

Electronic Floquet Liquid Crystals

Iliya Esin,¹ Gaurav Kumar Gupta,¹ Erez Berg,² Mark S. Rudner,³ and Netanel H. Lindner¹

¹*Physics Department, Technion, 3200003 Haifa, Israel*

²*Department of Condensed Matter Physics, Weizmann Institute of Science, Rehovot, 76100, Israel*

³*Center for Quantum Devices and Niels Bohr Institute, Niels Bohr Institute, University of Copenhagen, 2100 Copenhagen, Denmark*

“Floquet engineering” – designing band structures “on-demand” through the application of coherent time-periodic drives – has recently emerged as a powerful tool for creating new topological and anomalous phases of matter. In this manuscript, we show that the same principle can be applied to create non-equilibrium correlated states with spontaneously broken symmetry in a lightly doped semiconductor. The periodic drive provides means for obtaining large electronic densities of states necessary for the broken symmetry phase. The phase transition occurs in the steady-state of the system achieved due to interplay between the coherent external drive, electron-electron interactions, and dissipative processes arising from the coupling to phonons and the electromagnetic environment. We obtain the phase diagram of the system using numerical calculations that match predictions obtained from a phenomenological treatment and discuss the conditions on the system and the external drive under which spontaneous symmetry breaking occurs. Our results imply that Floquet engineering of the density of states provides a new route for generating and controlling correlated states of electrons with external fields.

INTRODUCTION

Strongly-correlated phases of electronic systems emerge from the competition between the potential energy savings and kinetic energy costs of developing correlations that allow electrons to avoid each other. In materials with band structures that feature large densities of states (DOSs), the kinetic energy costs that oppose the formation of correlations are small. Such materials therefore provide a rich platform for realizing exotic phases of matter where interparticle interactions crucially alter the ground state properties of the system.

In two-dimensional systems, a prominent route to achieving high DOS bands is through the application of strong out-of-plane magnetic fields, which gives rise to flat Landau levels. At certain rational filling fractions, the resulting macroscopic degeneracy is lifted by the formation of strongly-correlated fractional quantum Hall states [1, 2]. Recently, a rich phase diagram of correlated states arising from flat band formation has also been uncovered for twisted bilayer graphene, when the twist angle between layers is tuned close to the “magic angle” [3–8].

Two-dimensional systems in which the minimum of the single-particle dispersion occurs along a ring in momentum space (rather than at a single point, as for a standard parabolic dispersion), provide an alternative route for achieving large densities of states and novel correlated phases [9–21]. This occurs, for example, in two-dimensional materials with strong Rashba-type spin-orbit coupling [22, 23]. The ring-minimum in such systems leads to a large degeneracy and a divergent DOS at energies approaching the bottom of the band. At low densities, inter-particle interactions may lead to a plethora of possible symmetry-broken phases. In particu-

lar, for short-ranged interactions, novel electronic liquid-crystalline ground states were predicted in Ref. 16. These phases exhibit spontaneously broken rotational symmetry, with extremely anisotropic Fermi surfaces and related susceptibilities.

Here we present a “Floquet engineering” approach for inducing analogous liquid crystalline phases in electronic systems using time-periodic driving. Floquet engineering [24–28] has recently emerged as a powerful technique for creating topological bands [29–41] and for inducing novel non-equilibrium phases [42–55]. Along with extensive theoretical progress, Floquet engineering has been experimentally realized in solid-state, as well as atomic, molecular and optical (AMO) systems [56–65].

The non-equilibrium phase transition that we describe results from an interplay between coherent driving, electron-electron interactions, and dissipative dynamics due to the system’s coupling to its environment [66–80]. The coherent drive is used to produce a Floquet band structure that features a ring-like minimum analogous to that of the Rashba system described above. In turn, the interactions and dissipative dynamics determine the steady state of the system and the symmetry breaking that it exhibits.

A ring-like dispersion minimum is natural to obtain in a direct band gap system subjected to a coherent drive, where the drive frequency Ω is larger than the system’s band gap (see Fig. 1a). The structure of the modified (Floquet) bands is most easily visualized in a rotating frame. Starting from the original bands as depicted in Fig. 1a, we transform to a rotating frame in which the energies of all states in the valence band are rigidly shifted upwards by $\hbar\Omega$ [32]. In the rotating frame, the (shifted) valence and conduction bands cross along a continuous “resonance ring” of points in momentum space where the original conduction and valence bands were separated by

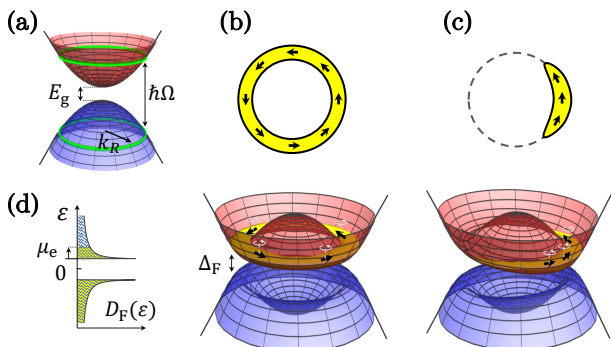


FIG. 1. Single-particle band structure near the Γ -point. (a) The band structure of the non-driven semiconductor. The resonance rings of the external drive are indicated by the green curves. (b,c) Floquet quasienergy bands arising from the semiconductor’s band structure and the resonant drive around $\varepsilon = 0$. The yellow area represents the occupation of the upper Floquet band in the “ideal” distribution scenario, analogous to the zero-temperature Gibbs state for the quasi-energy spectrum. Black arrows represent the pseudospin direction of the Floquet states near the resonance ring. The texture of the pseudospins arises from the pseudospin-momentum locking induced by the semiconductor. In addition, each pseudospin rotates in the x - y plane with the frequency of the periodic drive as is indicated on the figure by the light-gray thin arrows attached to each pseudospin. In the symmetric phase, (b), due to rotational symmetry the Floquet states near the resonance ring are uniformly occupied, as is indicated below panel (b). Panel (c) demonstrates the single-particle Floquet bands in the broken symmetry phase. In this case, the resonance ring is tilted towards a spontaneously chosen direction. The occupation of the bands is then biased toward this direction, signalling a ferromagnetic alignment of the pseudospins. (d) The density of Floquet states as a function of the quasi-energy around $\varepsilon = 0$ in the paramagnetic phase. The density of states features square-root Van Hove singularities in each Floquet band, i.e., $D_F(\delta\varepsilon) \sim \delta\varepsilon^{-1/2}$ in the upper Floquet band, where $\delta\varepsilon \equiv \varepsilon - \Delta_F/2$. A similar relation holds for the lower Floquet band.

$\hbar\Omega$ (see green curves in Fig. 1a). After transforming to the rotating frame, the driving field obtains a static (co-rotating) part, and a component that oscillates with integer multiples of the drive frequency Ω . Within the rotating wave approximation we keep only the static part of the drive in the rotating frame, and discard the oscillating components. As we show in detail below, under appropriate conditions on the material’s band structure and the form of the drive, the co-rotating part of the drive opens a “Floquet gap” all the way around the resonance ring. The minima and maxima of the resulting upper and lower Floquet bands correspondingly occur along a ring in momentum space (see Fig. 1b), yielding a DOS for the Floquet bands, $D_F(\varepsilon)$, with square-root divergences near the two band extrema (Fig. 1d). Along these ring-extrema, the Floquet-Bloch states may be characterized

by a pseudo-spin with a non-trivial winding, see Fig 1b, in close analogy to the spin winding that occurs around the ring minimum of a Rashba-type band structure.

Our goal is to find the conditions under which the divergence in the DOS promotes spontaneous symmetry breaking in the electronic steady-state of the system. Throughout this paper we study a system lightly doped above half filling. To preview the considerations involved, consider first an ideal situation where the steady-state is a zero-temperature Gibbs state of electrons in the band structure obtained in the rotating wave approximation [81]. In the absence of electron-electron interactions this zero temperature state corresponds to a full lower Floquet band and an annulus-shaped Fermi sea at the bottom of the upper band, as indicated in Fig 1b. At low doping density, the DOS at the Fermi energy is strongly enhanced due to the divergence at the band bottom. Sufficiently strong electron-electron interactions make it energetically favorable for electrons to change the topology of the Fermi sea from an annulus to a single pocket centered around a spontaneously chosen point on the resonance ring. The symmetry broken state is ferromagnetic as the pseudospins of the electrons are predominantly aligned along one direction, see Fig. 1c. This leads to a reduction in the potential energy (as the electronic wavefunction overlaps are suppressed for parallel pseudospins due to Pauli exclusion). As a consequence the mean-field band structure in the symmetry broken phase acquires a tilt along the spontaneously chosen momentum direction. Interestingly, due to the periodic time-dependence of the Floquet states, the emergent pseudospin magnetization vector rotates in time at the frequency of the drive (in the lab frame).

The discussion above, based on the rotating wave approximation and a zero-temperature Gibbs-type steady state, captures the essence of the symmetry breaking transition. However, the non-equilibrium nature of the setup implies that the steady-state cannot be described by a simple Gibbs state. Even when the electronic system is coupled to a zero-temperature heat bath, unavoidable scattering processes create electron-hole excitations in the Floquet bands. These excitations may suppress the tendency towards ordering. In this work, we introduce a self-consistent treatment of coupled kinetic and Floquet-Hartree-Fock equations that capture the interplay between the steady state of the system and its renormalized Floquet band structure, with the possibility of spontaneously broken symmetry. Using this treatment, we will obtain the non-equilibrium phase diagram for different doping densities, interaction strengths, and properties of the external heat baths.

MODEL SYSTEM AND PROBLEM SETUP

To study the phase transition in the steady-state of a periodically driven direct bandgap semiconductor, we introduce an effective model that describes the single-particle electronic states near the semiconductor's Γ -point. We consider a two-band, two-dimensional (2D) system, with topologically trivial bands. (This model, which lacks time reversal symmetry, may be taken to represent half of the degrees of freedom of a time-reversal symmetric semiconductor [32, 82].) We assign a common effective mass m_* for the electrons in the conduction band and holes in the valence band, and denote the gap separating these bands by E_g , see Fig. 1a. The Hamiltonian describing the electronic system and the time-periodic drive, near the Γ -point, reads

$$\hat{H}(t) = \sum_{\mathbf{k}} \hat{\mathbf{c}}_{\mathbf{k}}^\dagger [H_0(\mathbf{k}) + H_d(t)] \hat{\mathbf{c}}_{\mathbf{k}} + \sum_{\mathbf{q}} \mathcal{V}_{\mathbf{q}} \hat{\rho}_{\mathbf{q}} \hat{\rho}_{-\mathbf{q}}. \quad (1)$$

Here $H_0(\mathbf{k}) = E_0 + (\hbar^2 |\mathbf{k}|^2 / 2m_* + E_g/2) \sigma^z + \lambda_0 \mathbf{k} \cdot \boldsymbol{\sigma}$, where $\mathbf{k} = (k_x, k_y)$ is the two-dimensional momentum, $\hat{\mathbf{c}}_{\mathbf{k}}^\dagger = (\hat{c}_{\mathbf{k}\uparrow}^\dagger, \hat{c}_{\mathbf{k}\downarrow}^\dagger)$ is the two-component spinor for the pseudospin degree of freedom, $\mathcal{V}_{\mathbf{q}}$ describes an effective short-ranged electron-electron interaction, $\hat{\rho}_{\mathbf{q}} = \sum_{\mathbf{k}} \hat{\mathbf{c}}_{\mathbf{k}+\mathbf{q}}^\dagger \hat{\mathbf{c}}_{\mathbf{k}}$, and E_0 is an energy offset. We denote the pseudospin-orbit coupling by λ_0 and use $\boldsymbol{\sigma} = (\sigma^x, \sigma^y)$, where σ^α , $\alpha = x, y, z$, is a Pauli matrix in the pseudospin space. The bandstructure of the system in the absence of the drive is given by the spectrum of H_0 . We denote the energies of the valence and conduction band by $E_v(\mathbf{k})$ and $E_c(\mathbf{k})$, respectively.

We consider a uniform driving field that couples to the electrons through σ^z , $H_d(t) = V \cos(\Omega t) \sigma^z$ [83], with an above-gap frequency $\hbar\Omega = E_g + \delta E$, where δE is much smaller than semiconductor's full bandwidth. The Floquet state solutions of $\hat{H}(t)$ for $\mathcal{V}_{\mathbf{k}} = 0$ satisfy $[i\hbar \frac{\partial}{\partial t} - H_0(\mathbf{k}) - H_d(t)] |\psi_{\mathbf{k}\nu}(t)\rangle = 0$, with $|\psi_{\mathbf{k}\nu}(t)\rangle = e^{-i\varepsilon_{\mathbf{k}\nu} t / \hbar} |\phi_{\mathbf{k}\nu}(t)\rangle$. Here $|\phi_{\mathbf{k}\nu}(t)\rangle = |\phi_{\mathbf{k}\nu}(t + \mathcal{T})\rangle$ is periodic with period $\mathcal{T} = 2\pi/\Omega$ and ε is the quasienergy (which is periodic in $\hbar\Omega$). Throughout, we use the convention $-\hbar\Omega/2 \leq \varepsilon < \hbar\Omega/2$. For convenience we take $E_0 = \hbar\Omega/2$ such that $\varepsilon = 0$ at the center of the Floquet gap (see Fig. 1d).

The drive resonantly couples valence and conduction band states along a ring in momentum space for which $\hbar\Omega = E_c(\mathbf{k}) - E_v(\mathbf{k})$. We denote the radius of this ring by k_R . At the resonance ring, a gap of magnitude $\Delta_F = 2\lambda_0 k_R V / \hbar\Omega$ opens in the Floquet quasienergy spectrum. This gap separates the ‘‘upper Floquet’’ ($\nu = +$) and ‘‘lower Floquet’’ ($\nu = -$) bands, corresponding respectively to $\varepsilon > 0$ and $\varepsilon < 0$. Here, we will focus on the parameter regime $\Delta_F \ll \delta E$, where the ring minimum is well developed. Each of the bands has a ring of degenerate states associated with square-root van Hove singularities in the density of Floquet states: near the bottom

of the upper Floquet band, the density of states takes the form $D_F(\delta\varepsilon) \approx \frac{m_*}{2\pi\hbar^2} \sqrt{\frac{\Delta_F}{\delta\varepsilon}}$, where $\delta\varepsilon = \varepsilon - \Delta_F/2$, see Fig. 1. A similar expression holds for quasienergies near the top of the lower Floquet band. Below we show how these van Hove singularities promote spontaneous symmetry breaking in the driven system.

ORDER PARAMETER AND FLOQUET SELF-CONSISTENT MEAN FIELD APPROACH

In this work we will look for spontaneous symmetry breaking that emerges in the steady state of the driven system. The steady state arises from an interplay between the time-periodic drive, electron-electron interactions, and the coupling of the electrons to the electromagnetic and phononic modes of their environment. In this interplay, the electron-electron interactions play a dual role, as they lead to formation of order parameters as well as to incoherent scattering which may suppress the tendency towards order.

In order to capture the coherent part of the electron-electron interaction, which leads to order parameter formation, we use a mean-field approximation [84] in which we assume that the steady state is Gaussian (i.e., obeys Wick's theorem). We assume translation invariance is maintained, and consider a mean-field decoupling of the Hamiltonian Eq. (1) with ferromagnetic nematic order parameter

$$\mathbf{h}_{\mathbf{k}}(t) = - \sum_{\mathbf{k}'} \mathcal{V}_{\mathbf{k}-\mathbf{k}'} \langle \hat{\mathbf{c}}_{\mathbf{k}'}^\dagger \boldsymbol{\sigma} \hat{\mathbf{c}}_{\mathbf{k}'} \rangle_{\text{MF}}. \quad (2)$$

The expectation value in Eq. (2) is taken with respect to the time-periodic steady-state of the system. The corresponding mean-field Hamiltonian is given by $\hat{H}_{\text{MF}}(t) = \sum_{\mathbf{k}} \hat{\mathbf{c}}_{\mathbf{k}}^\dagger H_{\text{MF}}(\mathbf{k}, t) \hat{\mathbf{c}}_{\mathbf{k}}$, where

$$H_{\text{MF}}(\mathbf{k}, t) = H_0(\mathbf{k}) + H_d(t) + \mathbf{h}_{\mathbf{k}}(t) \cdot \boldsymbol{\sigma}. \quad (3)$$

Note that if $\mathbf{h}_{\mathbf{k}}(t)$ has the same time-period as the drive, $\hat{H}_{\text{MF}}(t)$ is also time-periodic and therefore defines a new Floquet problem.

The time-periodic steady state used in Eqs. (2) and (3) is determined self-consistently by solving the kinetic equation for the populations of electrons in the Floquet bands of $\hat{H}_{\text{MF}}(t)$. These populations are defined as $f_{\mathbf{k}\nu}(t) \equiv \langle \hat{\phi}_{\mathbf{k}\nu}^\dagger(t) \hat{\phi}_{\mathbf{k}\nu}(t) \rangle$, where $\hat{\phi}_{\mathbf{k}\nu}^\dagger(t)$ is a creation operator corresponding to the Floquet state $|\phi_{\mathbf{k}\nu}(t)\rangle$. Note that the meaning of the index ν and the values of populations $f_{\mathbf{k}\nu}$ depend on the order parameter, $\mathbf{h}_{\mathbf{k}}(t)$, as it determines the Floquet bandstructure of $\hat{H}_{\text{MF}}(t)$. The kinetic equation includes scattering rates due to electron-phonon interactions, $I_{\mathbf{k}\nu}^s$, radiative recombination, $I_{\mathbf{k}\nu}^\ell$, and electron-electron collisions, $I_{\mathbf{k}\nu}^{\text{ee}}$, and is given by

$$\dot{f}_{\mathbf{k}\nu} = I_{\mathbf{k}\nu}^s(\{f\}) + I_{\mathbf{k}\nu}^\ell(\{f\}) + I_{\mathbf{k}\nu}^{\text{ee}}(\{f\}), \quad (4)$$

where the steady state is determined by $\dot{f}_{\mathbf{k}\nu} = 0$. The notation $\{f\}$ refers to the full set of populations over all momenta and band indices.

In writing the kinetic equation in terms of the populations $f_{\mathbf{k}\nu}$ we have assumed that the Gaussian steady state is approximately described by a single particle density matrix which is diagonal in the Floquet basis. This condition is satisfied when the scattering rates in the steady state are small, $\hbar/(\tau_{\text{scat}}\Delta_F) \ll 1$ [70]. Here $1/\tau_{\text{scat}}$ is the total scattering rate of the electrons.

The scattering rates $I_{\mathbf{k}\nu}^s$ and $I_{\mathbf{k}\nu}^\ell$ describe scattering processes in which a boson (phonon, s, or photon, ℓ) is emitted or absorbed by the electronic system. The corresponding rates are determined by the dispersions of these bosons, and the form of the electron-boson coupling.

We denote by $\hat{b}_{p\mathbf{q}}^\dagger$ the operator creating an acoustic phonon (for $p = s$) or a photon (for $p = \ell$) with the three-dimensional (3D) momentum $\mathbf{q} = (\mathbf{q}_\parallel, q_z)$ and frequency $\omega_{\mathbf{q}} = v_p|\mathbf{q}|$. Here \mathbf{q}_\parallel is the component of \mathbf{q} within the plane of the 2D electronic system and $v_s(v_\ell)$ is the speed of sound (light). Note that the phonons propagate in the 3D substrate of the 2D electronic system.

The electron-boson coupling is described by the Hamiltonian [85]

$$\hat{\mathcal{H}}_{\text{HB}} = \sum_{\mathbf{k}, p, \mathbf{q}} \hat{\mathbf{c}}_{\mathbf{k}}^\dagger \mathcal{M}_p(\mathbf{q}_\parallel, \omega_{\mathbf{q}}) \hat{\mathbf{c}}_{\mathbf{k}+\mathbf{q}_\parallel} (\hat{b}_{p, \mathbf{q}}^\dagger + \hat{b}_{p, -\mathbf{q}}) + \text{h.c.}, \quad (5)$$

where $\mathcal{M}_p(\mathbf{q}_\parallel, \omega_{\mathbf{q}})$ is the coupling matrix in pseudospin space. We consider a diagonal electron-phonon coupling matrix in the $\{\uparrow, \downarrow\}$ basis, which captures the conservation of the pseudospin in small-momentum-transfer electron-phonon interactions. In contrast, photon emission requires changing the electronic angular momentum. We account for this by taking an electron-photon coupling matrix that is strictly off-diagonal in the $\{\uparrow, \downarrow\}$ basis, as these two basis states have opposite parity. Throughout the manuscript, we will assume that the phonons and photons are in thermodynamic equilibrium at zero-temperature.

The rates $I_{\mathbf{k}\nu}^s$ and $I_{\mathbf{k}\nu}^\ell$ in Eq. (4) can be computed through Floquet-Fermi's golden rule [86] using the electron-boson coupling in Eq. (5). Similarly, $I_{\mathbf{k}\nu}^{\text{ee}}$ is computed using Floquet-Fermi's golden rule and the electron-electron interactions appearing in Eq. (1). Explicit expressions for these rates appear in the supplementary material (SM).

FERROMAGNETIC-NEMATIC STEADY STATES

Before presenting the full steady-state solution to Eqs. (2), (3), and (4), we introduce a phenomenological model which we will use to characterize the phase diagram of the system. The model includes the key processes required for obtaining the steady-state distribution for

the electrons. Our goal is to identify the conditions on the electronic system and its environment under which spontaneous symmetry breaking may occur. A key quantity for describing the steady state is the density of electrons in the upper Floquet band, defined as $n_e = \int \frac{d^2\mathbf{k}}{(2\pi)^2} f_{\mathbf{k}+}$. Likewise, the density of holes in the lower band, n_h , is computed by integration over $1 - f_{\mathbf{k}-}$. In what follows, we discuss generation and annihilation rates of electron-hole pairs (in the Floquet basis) resulting from collision processes [see Eq. (4)]. We refer to these as heating and cooling processes, respectively. Of particular importance are Floquet-Umklapp processes, in which the energies of the electrons and bosonic modes in the initial and final states differ by $\hbar\Omega$. At zero bath temperature, these processes provide the only mechanism for heating.

We will be interested in the situation in which the system is doped slightly above half filling. In the absence of Floquet-Umklapp processes and at zero bath temperature, the steady-state is a zero-temperature Gibbs distribution of electrons in the (mean-field) Floquet bands [81]. Specifically, in this situation, the steady state features a completely filled lower Floquet band, and a low density Fermi sea of electrons in the upper Floquet band. In the presence of Floquet-Umklapp processes, this ideal distribution is perturbed by the creation of (inter-Floquet-band) electron-hole pairs. We will focus on the regime where the densities of electrons and holes in the upper and lower Floquet bands are low: $n_e, n_h \ll \mathcal{A}_R$, where $\mathcal{A}_R \equiv \pi k_R^2$ is the area in reciprocal space enclosed by the resonance ring.

The pair creation rate in almost empty upper and almost full lower Floquet bands is approximately independent of the densities of electrons and holes in the respective bands. We denote the total pair creation rate due to collisions with both phonons and photons by $\dot{n}_e|_{\text{ph}} = \Gamma_{\text{ph}}$. Similarly, the pair creation rate due to electron-electron collisions is denoted by $\dot{n}_e|_{\text{ee}} = \Gamma_{\text{ee}}$. The parameter Γ_{ee} depends on $\mathcal{V}_{\mathbf{q}}^2$ at \mathbf{q} corresponding to the inverse interparticle distance in the nearly filled band. The processes contributing to $\dot{n}_e|_{\text{ee}}$ are of the Floquet-Umklapp type, and are suppressed by $(V/\hbar\Omega)^2$. In addition, electron-electron scattering gives rise to quasienergy conserving processes, causing thermalization of the populations within each band without changing the electron and hole population densities. These processes therefore do not contribute to $\dot{n}_e|_{\text{ee}}$. Moreover, as in equilibrium, these elastic scattering processes all together preserve the form of the distribution when the electrons are distributed according to the Fermi-function over the quasienergy spectrum.

Once excited, the electrons (holes) rapidly relax to the bottom (top) of the Floquet band through multiple low-energy phonon emissions. The electron-hole pairs then annihilate through inter-Floquet-band scattering processes mediated by phonons [87]. The rate of the

pair annihilation processes, $\dot{n}_e|_{\text{cool}}$, is proportional to the product of the densities of electrons and holes. Therefore, we estimate $\dot{n}_e|_{\text{cool}} = -\Lambda_{\text{inter}}n_en_h$, where Λ_{inter} is independent of the populations. Note that for this essential cooling process to occur, the Debye frequency of the phonons needs to be larger than the Floquet gap Δ_F .

Summing up the cooling and heating rates we obtain a rate equation for the density of electrons in the upper Floquet band,

$$\dot{n}_e = \Gamma_{\text{ph}} + \Gamma_{\text{ee}} - \Lambda_{\text{inter}}n_en_h. \quad (6)$$

In the steady-state ($\dot{n}_e = 0$), Eq. (6) leads to $n_en_h = \kappa$, where we define the ‘‘heating parameter’’ $\kappa \equiv \kappa_{\text{ph}} + \kappa_{\text{ee}}$, with $\kappa_{\text{ph}} \equiv \Gamma_{\text{ph}}/\Lambda_{\text{inter}}$, $\kappa_{\text{ee}} \equiv \Gamma_{\text{ee}}/\Lambda_{\text{inter}}$. Furthermore, the difference between electron and hole excitation densities is fixed by the electron doping, Δn , measured relative to half-filling, $n_e - n_h = \Delta n$. Using this relation, together with the steady-state solution to Eq. (6) we obtain

$$n_{e/h} = \sqrt{(\Delta n/2)^2 + \kappa} \pm \Delta n/2, \quad (7)$$

where the plus (minus) sign on the right hand side corresponds to the density of electrons (holes). Note that in the absence of drive-induced heating processes ($\kappa = 0$), the ideal steady-state with no holes in the lower band and density Δn in the upper band is obtained. In what follows, we focus on the electron-doped regime, $\Delta n \geq 0$ (similar considerations apply in the hole-doped regime).

Having established the steady-state densities of electrons and holes (concentrated near the Floquet band extrema at the resonance ring), Eq. (7), we are well-positioned to address the conditions for spontaneous breaking of rotational symmetry in the system. In the following, we assume contact interactions described by a constant in \mathbf{q} interaction strength, $\mathcal{V}_{\mathbf{q}} = U/\varpi$, and \mathbf{k} -independent magnetization $\mathbf{h}(t) = \mathbf{h}_{\mathbf{k}}(t)$ [see Eq. (2)], where ϖ is the area of the system. In the steady state, $\mathbf{h}(t)$ is time periodic with the same time-period as the drive. Therefore, we expand $\mathbf{h}(t)$ in terms of its Fourier harmonics,

$$\mathbf{h}(t) = \text{Re} [\mathbf{h}_0 + \mathbf{h}_1 e^{i\Omega t} + \dots]. \quad (8)$$

Here \mathbf{h}_0 and \mathbf{h}_1 are vectors of complex magnitudes, representing the constant and the first harmonic components of the mean-field, respectively, and ‘‘...’’ represents higher harmonics. The values of the coefficients $\{\mathbf{h}_i\}$ are determined self-consistently via Eqs. (2), (3), and (4).

Crucially, a nonvanishing magnitude of the ‘‘in-plane’’ (x - y) component of the magnetization $\mathbf{h}(t)$, which we denote by $\mathbf{h}^{(xy)}(t)$, does not respect the rotational symmetry of the microscopic Hamiltonian $\hat{\mathcal{H}}(t)$, see Eq. (1). Therefore, $|\mathbf{h}^{(xy)}(t)|$ serves as the order parameter for the ferromagnetic-nematic phase that we study. In contrast, a non-vanishing z component of $\mathbf{h}(t)$ respects the symmetry. Generically, we expect a non-vanishing z component of $\mathbf{h}(t)$ in both the symmetry broken and unbroken

phases. In particular, we expect a large static z component of \mathbf{h}_0 (with magnitude on the order of U) even in the absence of the drive. This static field simply renormalizes the parameters of H_0 in Eq. (1), and therefore we do not treat it self-consistently in our analysis.

For simplicity, in the analytical treatment below we take $\mathbf{h}_n = 0$ for $n \geq 2$ since these harmonics are suppressed by powers of $V/(\hbar\Omega)$ for $V/(\hbar\Omega) \ll 1$. Furthermore, we note that when the in-plane (x - y) components of \mathbf{h}_0 are small, $|\mathbf{h}_0^{(xy)}| \ll E_g$, their effect on the Floquet band structure via Eq. (3) is negligible. To facilitate the analysis we thus also take $\mathbf{h}_0 = 0$, thereby focusing our attention on the behavior of \mathbf{h}_1 , which describes the component of the magnetization that oscillates at the same frequency as the drive. In the next section we will present numerical results in which all harmonics are allowed to freely develop.

In order to understand the expected form of \mathbf{h}_1 , it is helpful to examine the Floquet states near the resonance ring. These states are created by the operators

$$\hat{\phi}_{\mathbf{k}\pm}^\dagger(t) = (e^{-i\Omega t} \hat{c}_{\mathbf{k}\uparrow}^\dagger \mp e^{i\theta_{\mathbf{k}}} \hat{c}_{\mathbf{k}\downarrow}^\dagger) / \sqrt{2} + \mathcal{O}(V/\hbar\Omega), \quad (9)$$

where $|\mathbf{k}| = k_R$ and $\theta_{\mathbf{k}} \equiv \arctan(k_y/k_x)$. The pseudospins of these states form a rotating-in-time ‘‘vortex’’ in the x - y plane, see Fig. 1b. In the low doping limit ($\Delta n \rightarrow 0$) and in the regime where cooling dominates over heating processes ($\kappa \ll \Delta n^2$), the upper Floquet band has a significant population only near the band’s bottom. Above a critical interaction strength, we expect the self-consistent solution to converge to a ferromagnetic nematic steady-state where the electrons localize around a single spontaneously chosen momentum on the ring (see Fig. 1c). Subsequently, due to the time-dependent pseudospin-momentum locking in Eq. (9), the pseudospins of the electrons will be synchronized. This implies that the ‘‘in-plane’’ (x - y) components of $\mathbf{h}(t)$ should take the form of a rotating (circularly polarized) field, with its dominant harmonic given by $\mathbf{h}_1^{(xy)} \approx h_1(\hat{x} - i\hat{y})/\sqrt{2}$. In our analysis we use $|\mathbf{h}_1^{(xy)}|$ as the diagnostic for spontaneous symmetry breaking.

We note that in both the symmetry broken and unbroken phases, the system exhibits an oscillating z -component of the magnetization $\mathbf{h}(t)$. The z -component of the harmonic \mathbf{h}_1 renormalizes the amplitude and phase of the drive [see text below Eq. (1)]. As we will show below, throughout the parameter regime of interest this renormalization remains weak. Therefore, in estimating the critical interaction strength below, we neglect this component and keep only $\mathbf{h}_1^{(xy)}$.

We now seek the minimal interaction strength, U_c , required to achieve spontaneous symmetry breaking for finite values of κ and Δn . To make progress, we approximate the distribution of electrons in the upper Floquet band by a Fermi-Dirac distribution with an effective chemical potential, μ_e , measured from the bottom of the

upper band, and temperature (measured in energy units), T_e . Analogously, we parametrize the hole distribution in the lower Floquet band by an effective chemical potential μ_h , measured from the top of the lower band, and temperature T_h . Such a fit well-approximates the distributions in the limit of low density (see Ref. 79 and numerical results in SM). Note that the electron and hole populations are generically described by finite effective temperatures, even when the baths are at zero temperature.

In Eq. (7) above, we found the total densities of electrons and holes in the upper and lower Floquet bands, n_e and n_h , respectively. However, a given pair of values for n_e and n_h can be obtained for a continuous family of choices of $\mu_{e/h}$ and $T_{e/h}$. Below we first derive a general result for the critical interaction strength U_c , parametrized by the chemical potentials and temperatures that are realized. Later, we will discuss how to determine the values of $\mu_{e/h}$ and $T_{e/h}$ in the steady-state.

To find U_c , assuming the transition is continuous, we solve Eq. (2) by expanding the expectation value on its RHS to linear order in the amplitude of the in-plane (x - y) component of the magnetization, $|\mathbf{h}_1^{(xy)}|$, which we take to be circularly polarized. Note that the RHS of Eq. (2) depends on $\mathbf{h}(t)$ through the steady-state distribution, $f_{\mathbf{k}\nu}$, defined in the basis of the eigenstates of H_{MF} [which also depend on $\mathbf{h}(t)$], see Eq. (3). Given that the effective temperature and chemical potential weakly depend on $\mathbf{h}_1^{(xy)}$, the dominant dependence of $f_{\mathbf{k}\nu}$ on $\mathbf{h}_1^{(xy)}$ arises from the eigenstates and eigenvalues of H_{MF} .

Expanding the RHS of Eq. (2) to linear order in h_1 yields three terms: (i) a contribution corresponding to a full lower Floquet band, and the contributions of (ii) the electrons and (iii) the holes in the upper and lower Floquet bands, respectively. We use the assumed Fermi-Dirac distribution functions for electrons and holes to evaluate each of the terms analytically (for the full derivation see SM), yielding an expression for the critical interaction strength:

$$\tilde{U}_c^{-1} = \tilde{U}_{\text{fb}}^{-1} + \tilde{U}_{\text{ex}}^{-1} \left(\frac{\tilde{\Theta}(\mu_e/T_e)}{\tilde{n}_e} + \frac{\tilde{\Theta}(\mu_h/T_h)}{\tilde{n}_h} \right). \quad (10)$$

Here $\tilde{U}_c = \mathcal{A}_R U_c / \delta E$, $\tilde{n}_e = n_e / \mathcal{A}_R$, and $\tilde{n}_h = n_h / \mathcal{A}_R$ are the normalized interaction strength and population densities, respectively. (Recall that \mathcal{A}_R is the area in reciprocal space enclosed by the resonance ring and $\delta E = \hbar\Omega - E_g$.) The dimensionless function $\tilde{\Theta}$ will be defined below. The contribution to the inverse of \tilde{U}_c of type (i) above is given by $\tilde{U}_{\text{fb}}^{-1}$. For a hypothetical state with a full lower Floquet band and an empty upper Floquet band, the critical interaction strength would be equal to \tilde{U}_{fb} . The contributions to \tilde{U}_c^{-1} of types (ii) and (iii) are captured by the terms proportional to $\tilde{U}_{\text{ex}}^{-1}$ in Eq. (10). At finite doping, and/or with a finite density of electron-hole excitations, these terms reduce the critical interaction strength. In the derivation of Eq. (10) we obtain ex-

PLICIT expressions for these coefficients, $\tilde{U}_{\text{ex}} = 4\pi^4 \delta E / \Delta_F$ and $\tilde{U}_{\text{fb}} = 2\pi^2 [\log \left(\frac{8E_{\text{BW}} \delta E}{\Delta_F} \right) - 1]^{-1}$, where E_{BW} is a high-energy cutoff representing the bandwidth of the semiconductor, see SM.

The enhancement of the density of states at the ring extrema of the Floquet bandstructure affects \tilde{U}_c through the terms of type (ii) and (iii) in Eq. (10). The unitless function $\tilde{\Theta}(x)$ that appears in this term has the form of a ‘‘smeared’’ step function that drops to zero when its argument is negative, and saturates to 1 in the opposite limit, with a smooth cross-over whose width is $\mathcal{O}(1)$. Therefore, the contribution of type (ii) is governed by a competition between two effects: on the one hand, for this term to be significant, a small density of electrons is required. On the other hand, to achieve $\tilde{\Theta}(\mu_e/T_e) \approx 1$ the distribution of the electrons in the upper Floquet band is required to have a sharp Fermi surface (which is realized for $\mu_e/T_e \gg 1$). When these conditions are met, the critical interaction strength is suppressed due to the divergence of the DOS at the ring minimum. Similar considerations hold for the contribution of type (iii) arising from holes in the lower Floquet band.

Equation (10) is a non-equilibrium analogue of the Stoner criterion [88, 89], which gives the critical interaction strength for spontaneous symmetry breaking in the steady-state of the system. The criterion crucially depends on the effective chemical potentials and temperatures of electrons and holes in the steady state, which are controlled by the interactions both within the system and between the system and its environment. As discussed above, when the electrons in the upper band form a low-density population with a sharp Fermi surface (such that $\tilde{\Theta} \approx 1$), the critical interaction strength U_c may be reduced. Such a suppression of U_c is particularly important for ensuring the possibility that a low-temperature symmetry-broken steady-state can arise in the non-equilibrium system, as the heating rate due to electron-electron scattering scales as U^2 [see Eq. (6)]. In the next section, we will analyze the phase diagram of the system using both numerical simulations and further analysis based on the rate equation approach.

PHASE DIAGRAM AND NUMERICAL SIMULATIONS

In this section, we introduce a lattice model whose effective description for momenta near the Γ -point is given by Eq. (1). Our motivation is to demonstrate symmetry breaking from a full self-consistent solution of the coupled kinetic and Floquet mean-field equations in Eqs. (2)–(4). In addition, we seek to validate the suppression of U_c due to the enhanced density of states near the resonance ring [exhibited by the term proportional to $\tilde{U}_{\text{ex}}^{-1}$ in Eq. (10)]. To this end, we extend the

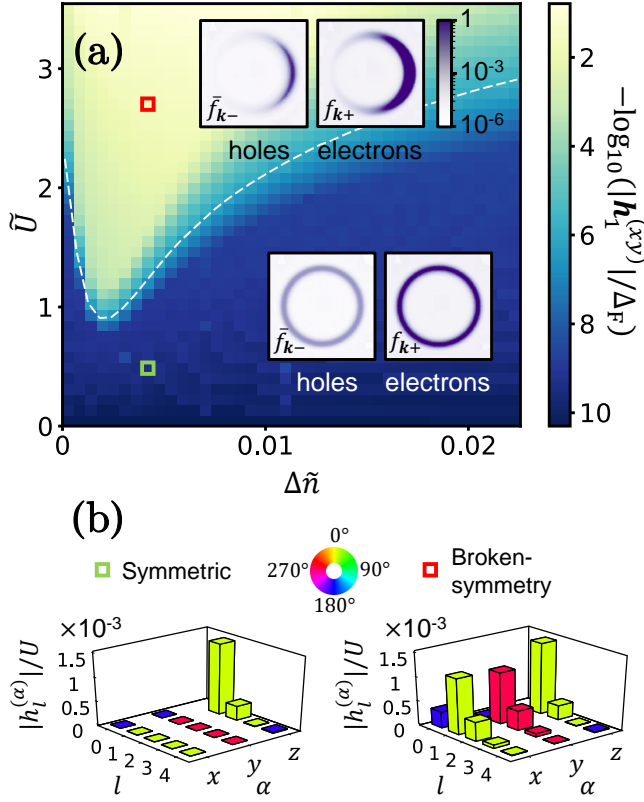


FIG. 2. (a) Spontaneous magnetization strength, $|\mathbf{h}_1^{(xy)}|$, obtained from the self-consistent mean-field calculation, as a function of a normalized electron doping, $\Delta\tilde{n} \equiv \Delta n/\mathcal{A}_R$ and normalized interaction strength, $\tilde{U} \equiv \mathcal{A}_R U/\delta E$. The dashed white line represents the phase boundary, corresponding to the critical interaction strength \tilde{U}_c , extracted using the same method as in Fig. 3 below. The insets show the electron and hole steady-state distributions (respectively $f_{\mathbf{k}+}$ and $\bar{f}_{\mathbf{k}-} \equiv 1 - f_{\mathbf{k}-}$) in the momentum domain near the resonance ring, for $\Delta\tilde{n} = 0.004$, $\tilde{U} = 0.44$, indicated by a green square, in the symmetric phase, and $\Delta\tilde{n} = 0.004$, $\tilde{U} = 2.66$, indicated by a red square, in the symmetry-broken phase. (b) Harmonics of the self-consistent magnetization $\mathbf{h}(t) = \text{Re} \left[\sum_{l,\alpha} \hat{\mathbf{e}}_\alpha h_l^{(\alpha)} e^{i\Omega t} \right]$, where $\hat{\mathbf{e}}_\alpha = \hat{\mathbf{x}}, \hat{\mathbf{y}}, \hat{\mathbf{z}}$. We plot $|h_l^{(\alpha)}|/U$ corresponding to the first five harmonics ($l = 0, 1, 2, 3, 4$) at the two points in the phase diagram indicated by the red and green squares in panel (a). The heights and the colors of the bars respectively indicate the amplitudes and phases of the harmonics. The color scale for the phase is shown at the top of the panel. Note that we omit $|h_0^{(z)}|$, which is responsible for the bandgap renormalization of the system in the absence of the drive, see main text.

Hamiltonian in Eq. (1) to the entire Brillouin zone of a square lattice with primitive lattice vectors $\mathbf{a}_1 = (a, 0)$ and $\mathbf{a}_2 = (0, a)$. We consider nearest and next nearest neighbor hopping, described by the modified Hamiltonian $H_0(\mathbf{k}) = \mathbf{d}(\mathbf{k}) \cdot \boldsymbol{\sigma}$, where $\mathbf{d} = (d_x, d_y, d_z)$, with $d_{x(y)}(\mathbf{k}) = A \sin(ak_{x(y)}) + A' [\sin(\mathbf{r}_1 \cdot \mathbf{k}) \pm \sin(\mathbf{r}_2 \cdot \mathbf{k})]$,

$d_z(\mathbf{k}) = E_g/2 - B[\cos(ak_x) + \cos(ak_y) - 2] - B'[\cos(\mathbf{r}_1 \cdot \mathbf{k}) + \cos(\mathbf{r}_2 \cdot \mathbf{k}) - 2]$, and Hubbard interaction $\mathcal{V}_\mathbf{q} = U/\varpi$. The coefficients A' and B' denote the next-nearest neighbor hopping along the vectors $\mathbf{r}_{1,2} = a(\hat{\mathbf{x}} \pm \hat{\mathbf{y}})$. In the numerical simulations we set $A' = A/4$ and $B' = B/4$ [90]. Note that the form of $H_0(\mathbf{k})$ used for the numerical simulation agrees with the Hamiltonian $H_0(\mathbf{k})$ in Eq. (1) for momenta near the Γ -point, with $A = 2\lambda_0/3a$, and $B = 2\hbar^2/3m_*a^2$. We consider the case $E_g, B > 0$ [91], and restrict $\hbar\Omega > E_g/2 + 4B$ to ensure that $2\hbar\Omega$ is larger than the total bandwidth, such that there are no second and higher order resonances in the numerical simulation.

Using the lattice model within the mean-field approximation, we numerically solved the rate and the mean-field equations for the steady state in a self-consistent manner according to the procedure described between Eqs. (2)-(4). To this end, we computed the occupation function $f_{\mathbf{k}\nu}$ and the scattering rates $I_{\mathbf{k}\nu}^s$, $I_{\mathbf{k}\nu}^\ell$, and $I_{\mathbf{k}\nu}^{ee}$ using a non-uniform grid of 8008 points in momentum space, with enhanced resolution in the vicinity of the resonance ring. We evaluated the scattering rates using Fermi's golden rule with the electron-phonon coupling matrix $\mathcal{M}_s(\mathbf{q}_\parallel, \omega) = g_s |\mathbf{q}_\parallel|/\sqrt{\omega}$, and electron-photon coupling matrices for two orthogonal photon polarizations, $\mathcal{M}_\ell^{(1)} = g_\ell \sigma^x$ and $\mathcal{M}_\ell^{(2)} = g_\ell \sigma^y$. The densities of states for spontaneous emission of acoustic phonons ($p = s$) and photons ($p = \ell$), traced over the out-of-plane momentum, are given by $\rho_p(\omega, \mathbf{q}_\parallel) = \rho_p^0 \omega / \sqrt{\omega^2 - |v_p \mathbf{q}_\parallel|^2}$ when $\omega > v_p |\mathbf{q}_\parallel|$ and $\rho_p = 0$ otherwise, where ω is the frequency of the emitted phonon or photon and \mathbf{q}_\parallel is the in-plane component of its momentum. The constants $g_{s(\ell)}$ and $\rho_{s(\ell)}^0$ are material-dependent parameters. In the simulations we tune $g_{s(\ell)}$ and $\rho_{s(\ell)}^0$ to explore their roles in determining the steady states, and to effectively tune the heating parameter κ for comparison with our analytical results. In the numerical results presented in the main text, we focus on the regime $\kappa_{ee} \ll \kappa_{ph}$, where Floquet-Umklapp electron-electron scattering processes do not significantly contribute to the heating rate. We obtain qualitatively similar results in the regime of $\kappa_{ee} \gtrsim \kappa_{ph}$, see SM.

In each iteration of the algorithm, we numerically compute the magnetization $\mathbf{h}(t)$ via Eq. (2). To improve the precision of the momentum integral, we first fit the electron and hole distributions to Fermi functions, then perform the integration using the fits interpolated to a finer grid. In the simulations, we allow for the magnetization to develop components up to the fifth harmonic of the driving frequency. As discussed below Eq. (2), we discard the constant in-time component in the z direction, which simply renormalizes the parameters of the underlying band structure.

In Fig. 2a we show the non-equilibrium phase diagram of the system in the plane of doping, Δn , and interaction strength, U . The bath parameters are fixed with values

that yield $\kappa_0 a^4 \approx 10^{-9}$, where the bare heating parameter, κ_0 , denotes the value of the heating parameter κ at $U = 0$ and half-filling (see SM for details). The color scale in Fig. 2a indicates the magnitude of spontaneous magnetization, $|\mathbf{h}_1^{(xy)}|$, for a lightly electron-doped system. The figure shows two distinct phases: a symmetric phase (blue), $|\mathbf{h}_1^{(xy)}| = 0$, and a broken-symmetry phase (yellow), $|\mathbf{h}_1^{(xy)}| > 0$.

We present characteristic particle distributions well-inside of each phase in the insets to Fig. 2a. In the paramagnetic (symmetry-preserving) phase, the electron and hole populations exhibit uniform occupation of states around the resonance ring. In the ferromagnetic nematic (broken symmetry) phase, the electron and hole populations are concentrated on one side of the resonance ring. The magnitudes of the harmonics of $\mathbf{h}(t)$ for the same representative states in the two phases are shown in Fig. 2b. Here it is evident that in the broken symmetry phase the first harmonic \mathbf{h}_1 gives the dominant contribution, yet the DC component and second harmonic are substantial. Although present, as discussed below Eq. (8), these harmonics do not significantly affect the Floquet mean-field band structure.

The boundary between the phases occurs at a critical interaction strength U_c . The dependence of U_c on the doping Δn can be explained using Eq. (10). However, to use Eq. (10) we first need to know how $\mu_{e(h)}/T_{e(h)}$ and $n_{e(h)}$ depend on Δn and other parameters of the model. The electron and hole densities $n_{e(h)}$ found from the phenomenological rate equation treatment are given in Eq. (7). We now seek two additional equations to fix the ratios μ_e/T_e and μ_h/T_h for these electron and hole populations, respectively. (Recall that the same values of n_e and n_h can be obtained from a continuous family of values of μ_e/T_e and μ_h/T_h .) Note that $\mu_{e(h)}/T_{e(h)}$ and $n_{e(h)}$ depend on U through their dependence on κ . Therefore, the RHS of Eq. (10) implicitly depends on U_c . For simplicity, as in the numerical simulations that lead to Fig. 2, here we focus on the case of $\kappa_{ee} \ll \kappa_{ph}$, where the heating parameter κ can be treated as a U independent parameter (see text below Eq. (6) for definitions).

Connecting back to U_c given by Eq. (10), recall that $\tilde{\Theta}(\mu_e/T_e) = \mathcal{O}(1)$ when $\mu_e/T_e > 1$, leading to a suppression of U_c . In this situation, the population of electrons in the upper band exhibits a sharp Fermi surface. We refer to such a state as a degenerate electronic Floquet metal (EFM). Alternatively, if $\mu_e/T_e < 0$, the effective chemical potential lies in the Floquet gap and the electronic distribution corresponds to a non-degenerate Fermi gas. We refer to such a state as an electronic Floquet insulator (EFI). In this state, $\tilde{\Theta}(\mu_e/T_e)$ is small.

We now discuss the factors that determine the value of μ_e/T_e and which phase (EFM or EFI) is achieved in the steady state. The EFM phase is established when the intraband cooling of excited electrons is more efficient than

the relaxation of electrons from the upper to the lower Floquet band. In this case, electrons excited from the lower to the upper Floquet band via Floquet-Umklapp processes quickly relax to the bottom of the upper Floquet band, where a Fermi sea is formed. The flow of electrons into the Fermi sea in the upper Floquet band is balanced by phonon-assisted annihilation of electrons in the Fermi sea with holes in the lower Floquet band. The balance between these interband and intraband rates can be analyzed by extending the rate equation treatment, expressed in Eq. (6), to include an energy-resolved treatment of the electron and hole populations, see Ref. 79 and SM.

Deep in the EFM phase, and for $U \lesssim U_c$, the extended rate equation treatment yields $\mu_e/T_e \approx x_e^{1/4}$, where $x_e \equiv \zeta n_e^6 / (v_s^3 \kappa)$, and we estimate $\zeta \approx C \hbar^5 / (\Delta_F m_*^4 k_R^3)$, where C is a constant of $\mathcal{O}(10^{-3})$ (see SM for the full details). Since the EFM phase corresponds to large μ_e/T_e and therefore large x_e , this phase is favored at large electron density (large doping), small sound velocity v_s , and low values of the heating parameter κ . In particular, lower sound velocities facilitate intraband cooling, as this leads to an enhancement of the density of states for low frequency phonons.

The EFI phase is obtained in the opposite limit, where interband relaxation is more efficient than intraband cooling. In this case, the extended rate equation treatment yields $e^{\mu_e/T_e} \approx x_e^{1/5}$ (see SM). The extended rate equation treatment can also be used to characterize the hole population in the lower Floquet band. We find that for electron doping, $\Delta n > 0$, the holes form a non-degenerate Fermi gas for all parameter values within our model. Fast, quasienergy conserving electron-hole scattering processes tend to equalize the electron and hole temperatures, T_e and T_h .

Figure 3 shows a comparison of μ_e/T_e and U_c extracted from numerical simulations (data points), to the analytical estimates obtained from the extended rate equations discussed above. We obtain U_c using a numerical analogue of the procedure leading to Eq. (10). Specifically, we compute the expectation value on the RHS of Eq. (2), using the steady state obtained from Eq. (4) for a system whose electronic Hamiltonian corresponds to $\hat{\mathcal{H}}_{\text{MF}}(t)$ in Eq. (3). In this procedure for obtaining U_c , we use a prescribed form of $\mathbf{h}(t)$ with a single non vanishing harmonic $\mathbf{h}_1^{(xy)}$ of small magnitude in $\hat{\mathcal{H}}_{\text{MF}}(t)$, see Eq. (8). The dashed white line in Fig. 2a shows U_c extracted using the above procedure on top of the phase diagram obtained from the full self-consistent numerical simulations for the same parameters.

In Fig. 3a we show μ_e/T_e as a function of doping Δn for several values of phonon sound velocity v_s . We extract μ_e and T_e from the numerical simulations described in the previous paragraph by fitting the electron steady state distribution in the upper Floquet band to a Fermi func-

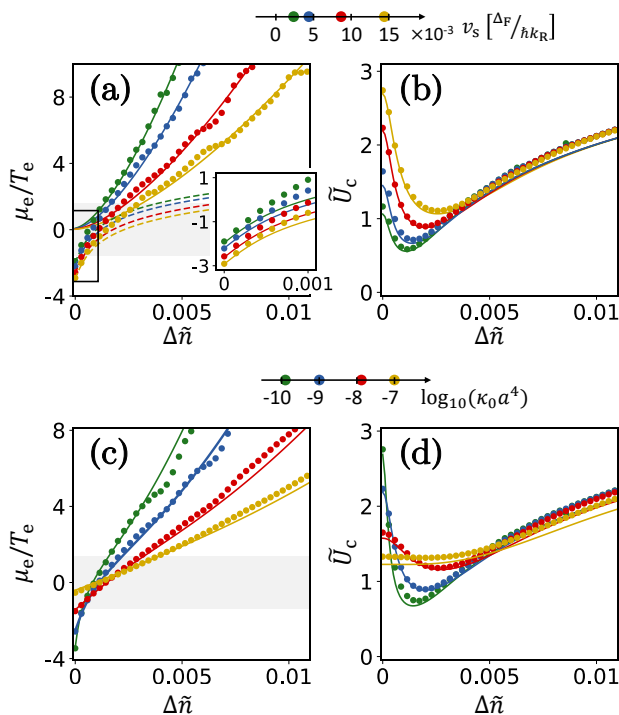


FIG. 3. (a) Numerically obtained ratio of effective chemical potential to temperature of the electronic population in the upper Floquet band, as a function of the normalized doping (data points). The data are extracted from the steady-state solution to Eq. (4) for $\kappa_0 a^4 \approx 10^{-9}$ and four values of speed of sound, v_s . Solid and dashed lines represent the results of the extended rate equation treatment for the EFM and the EFI phases, respectively. The full set of curves is generated using the same value of the single fit parameter ζ (see text for definition). The shaded area indicates the EFI-to-EFM crossover range where the $\tilde{\Theta}$ -function in Eq. (10) rises from 0 to 1. Inset: Zoom-in on the low-doping regime (enclosed by a black frame in the main panel). Solid lines correspond to the analytical curves for the EFI phase. (b) Critical interaction strength U_c extracted for the same data set as in panel a (data points). Solid lines represent U_c calculated from Eq. (10), where for the values of μ_e/T_e we used a function which interpolates between the analytical results deep in the EFM and EFI phases. We use the same value of ζ as in panel a, and two additional fitting parameters \tilde{U}_{ex} and \tilde{U}_{fb} . (c) and (d) Results for μ_e/T_e and U_c , extracted in the same manner as in panels a and b (data points), for $v_s = 0.0086 \Delta_F / \hbar k_R$, and four values of κ_0 . Solid lines in the two panels show the interpolated values of μ_e/T_e and the resulting U_c . All fitting parameters are the same as in panels a and b.

tion with respect to the quasienergies of the mean-field Hamiltonian [Eq. (3)]. The fit lines correspond to the analytical forms for μ_e/T_e obtained from the extended rate equation treatment. The solid and dashed lines correspond to the forms for μ_e/T_e in the EFM and EFI regimes, respectively. The only freedom in these fits is the parameter ζ in the definition of x_e , which was given the same value across all of the curves shown. The ex-

tracted value of ζ is of the same order of magnitude as the analytical estimate given above.

In Fig. 3c we again show μ_e/T_e as a function of Δn , this time highlighting the dependence on the value of the bare heating parameter κ_0 . In this plot, the fit lines are given by a function that interpolates between the analytical results for the asymptotic behavior in the EFM and EFI regimes: $\mathcal{F}_j[\lambda(\mu_e/T_e)] = x_e^\eta$, where \mathcal{F}_j is the complete Fermi-Dirac integral, $\eta = 0.174$, $j = -0.3$, and $\lambda = 0.871$. These parameter values are fixed by demanding that μ_e/T_e displays the correct dependence on x_e deep in the EFI ($e^{\mu_e/T_e} \sim x_e^{1/5}$) and EFM ($\mu_e/T_e \sim x_e^{1/4}$) phases. The value of ζ used in x_e is the same as used in Fig. 3a.

In Figs. 3b and d we show U_c as a function of Δn for different values of v_s and κ_0 . The data points are obtained from the numerical procedure discussed above. To obtain the fit lines, we use the interpolated values of (μ_e/T_e) in Eq. (10). We additionally use \tilde{U}_{ex} and \tilde{U}_{fb} as fitting parameters. The same values of these parameters were used in all curves shown. The values used for the fits are close to those obtained from the formulas given below Eq. (10). For the contribution of the holes, we used the same interpolating function, with x_h replacing x_e . Here x_h is defined in the same manner as x_e , but with n_h replacing n_e (with the same value of the parameter ζ). Note that holes are in the analogue of the EFI phase for any $\Delta n > 0$, and hence the value of $\tilde{\Theta}(\mu_h/T_h)$ is small throughout the regime studied.

As is evident in the phase diagram in Fig. 2a, U_c obtains a minimal value at an optimal value of the doping, which we denote Δn_* . Using the extended rate equation treatment, we estimate $\Delta n_* = C_*(v_s^3 \kappa / \zeta)^{1/6}$, where C_* is a constant of $\mathcal{O}(1)$, see SM. The corresponding minimal interaction strength is given by $\tilde{U}_c^{\text{min}} \approx \tilde{U}_{\text{ex}} \Delta n_* / \mathcal{A}_R$ for $\kappa \ll k_R^4$. For $\Delta n > \Delta n_*$, electrons in the upper band are in the EFM phase, and exhibit a sharp Fermi surface (note the corresponding values of μ_e/T_e in Fig. 3a). As explained below Eq. (10), the existence of a Fermi surface tends to reduce the critical interaction strength. However, as the doping increases, the phase transition requires stronger interactions as the density of states at the Fermi surface decreases. Below the optimal doping, $\Delta n < \Delta n_*$, the electrons in the upper Floquet band are in the EFI regime, which has no Fermi surface. Thus, the suppression of U_c is lost for $\Delta n < \Delta n_*$.

DISCUSSION

In this work, we demonstrated a mechanism for realizing electronic liquids crystals in two-dimensional electronic systems through time-periodic driving. The phase that we find exhibits ferromagnetic-nematic order associated with spontaneous breaking of U(1) symmetry in both pseudospin and orbital degrees of freedom. Above the critical interaction strength, the Fermi sea becomes

highly anisotropic and occupies a limited sector of the ring minimum of the Floquet bands, see Figs. 1 and 2. Due to pseudospin-momentum locking, the Fermi sea in the symmetry broken phase exhibits a finite magnetization which rotates with the frequency of the drive [cf. Eq. (8)].

Our analysis has been carried out on a model system with a two-component pseudospin degree of freedom, whose bandstructure is described by $H_0(\mathbf{k})$, see Eq. (1). For $E_g > 0$, the model $H_0(\mathbf{k})$ lacks time reversal symmetry. The model can also be taken to describe half of the degrees of freedom of a time-reversal invariant system. Our analysis can be straightforwardly extended to include the relevant time-reversal partner degrees of freedom. In this situation, there are many more possibilities for how the system may order. As one example, in the SM we describe a mean-field treatment which shows an instability towards an order in which the magnetizations of the two time-reversal partners are aligned, which yields a breaking of the time-reversal symmetry. We leave a more elaborate study of this interplay for the future investigation.

For simplicity, throughout the paper we considered a driving whose form is described below Eq. (1). It is interesting to consider driving with circularly polarized light, which, like the drive we studied, preserves the U(1) symmetry of the system and uniformly opens a gap all the way around the resonance ring. Depending on the handedness of the drive, the pseudospin may wind twice or zero times around the resonance ring [32]. In the case of double winding, each direction of the pseudospin in the x - y plane corresponds to two momentum points on the resonance ring. Therefore, in this case, an analogous ferromagnetic-nematic phase would exhibit two electron pockets occupying opposite sectors of the ring minimum.

To put our results in an experimentally relevant context, we estimate the value of the heating parameter κ , employing the definition of κ appearing below Eq. (6). We base our estimate on typical scattering rates measured in semiconductors [92]. We start with the phonon assisted interband scattering rate, which we estimate by $\Lambda_{\text{inter}} \approx (\tau_s \mathcal{A}_{\text{BZ}})^{-1}$, where τ_s is a typical hot-electron scattering lifetime due to phonons, ~ 0.1 ps, and \mathcal{A}_{BZ} is the reciprocal-space area of the Brillouin zone. In addition, electron-phonon scattering also contributes to heating through Floquet-Umklapp scattering processes. We estimate the phonon-mediated excitation rate by $\Gamma_s \approx (V/\hbar\Omega)^2 \mathcal{A}_{\text{R}}/\tau_s$. The area inside the resonance ring \mathcal{A}_{R} appears due to the form of electron-acoustic phonon coupling and the band inversion of the Floquet bands. Radiative recombination predominantly occurs between states with inverted band indices, i.e., inside the resonance ring. We estimate this rate by $\Gamma_\ell \approx \mathcal{A}_{\text{R}}/\tau_\ell$, where τ_ℓ is a typical time for the radiative recombination evaluated as ~ 1 ns. Assuming $V/\hbar\Omega \approx 10^{-2}$ and $\mathcal{A}_{\text{R}}/\mathcal{A}_{\text{BZ}} \approx 10^{-3}$, we estimate $\kappa_{\text{ph}} = (\Gamma_s + \Gamma_\ell)/\Lambda_{\text{inter}} \approx 10^{-7} \mathcal{A}_{\text{BZ}}^2$.

Next, we estimate the electron-hole pair generation (heating) rate Γ_{ee} due to photon-assisted electron-electron scattering. To lowest order in $(V/\hbar\Omega)^2$, these processes predominantly excite a pair of electrons from the lower to the upper Floquet band, accompanied by the absorption of one photon from the driving field. Due to the pseudospin structure of the Floquet states the dominant scattering processes involve one electron that is scattered from the interior of the resonance ring to the exterior, and vice versa for the other electron. Therefore, we expect the scattering rate to be proportional to the squared area of the resonance ring. After averaging over initial and final momenta, we estimate $\Gamma_{\text{ee}}(U) = \frac{\mathcal{A}_{\text{R}}^2 m_* U^2}{2\pi^4 \hbar^3} \left(\frac{V}{\hbar\Omega}\right)^2$. The critical interaction strength is not significantly changed when $\kappa_{\text{ee}}(U_{\text{fb}}) \ll \kappa_{\text{ph}}$, where $\kappa_{\text{ee}}(U) = \Gamma_{\text{ee}}(U)/\Lambda_{\text{inter}}$ (see SM for supporting numerical simulations). When the above condition applies, and for $U \lesssim U_{\text{fb}}$, the effective temperatures of the electron and hole distributions are dominated by the electron-phonon and electron-photon interactions. The estimate for Γ_{ee} , when \mathcal{A}_{R} is small, shows that for realistic parameter choices, the above conditions can be indeed satisfied. We note that short-range interactions corresponding to this regime can be obtained using screening gates placed near the 2D electronic system.

The phenomenon we discussed can be realized in 2D Dirac systems such as transition metal dichalcogenides and semiconductor quantum wells. To ensure that Floquet-Umklapp processes are suppressed, it is beneficial to use large bandgap materials. In gapless Dirac system such as graphene, driving may induce similar ring-like Floquet-band extrema [37]. We leave the exploration of particle dynamics and symmetry breaking in such systems to future studies. The use of periodic driving to create ring extrema in Floquet bands may be utilized to study exotic phases of fermions and bosons in cold atom systems [31, 93, 94]. In particular, it would be interesting to investigate the possibility to use buffer gases in cold atom systems to serve as the heat baths needed for stabilizing the broken-symmetry phases discussed in this work.

ACKNOWLEDGMENTS

We would like to thank Ehud Altman, Vladimir Kalnizky, Gil Refael, and Ari Turner for illuminating discussions and David Cohen and Yan Katz for technical support. N. L. acknowledges support from the European Research Council (ERC) under the European Union Horizon 2020 Research and Innovation Programme (Grant Agreement No. 639172), and from the Israeli Center of Research Excellence (I-CORE) ‘‘Circle of Light’’. M. R. gratefully acknowledges the support of the European Research Council (ERC) under the European Union Horizon 2020 Research and Innovation Pro-

gramme (Grant Agreement No. 678862) and the Villum Foundation. M. R. and E. B. acknowledge support from CRC 183 of the Deutsche Forschungsgemeinschaft. G. K. G. acknowledges support from Israel Council for Higher Education.

-
- [1] D. C. Tsui, H. L. Stormer, and A. C. Gossard, *Phys. Rev. Lett.* **48**, 1559 (1982).
- [2] R. B. Laughlin, *Phys. Rev. Lett.* **50**, 1395 (1983).
- [3] R. Bistritzer and A. H. MacDonald, *Proc. Natl. Acad. Sci. USA* **108**, 12233 (2011).
- [4] Y. Cao, V. Fatemi, S. Fang, K. Watanabe, T. Taniguchi, E. Kaxiras, and P. Jarillo-Herrero, *Nature* **556**, 43 (2018).
- [5] Y. Cao, V. Fatemi, A. Demir, S. Fang, S. L. Tomarken, J. Y. Luo, J. D. Sanchez-Yamagishi, K. Watanabe, T. Taniguchi, E. Kaxiras, R. C. Ashoori, and P. Jarillo-Herrero, *Nature* **556**, 80 (2018).
- [6] M. Yankowitz, S. Chen, H. Polshyn, Y. Zhang, K. Watanabe, T. Taniguchi, D. Graf, A. F. Young, and C. R. Dean, *Science* **363**, 1059 (2019).
- [7] A. L. Sharpe, E. J. Fox, A. W. Barnard, J. Finney, K. Watanabe, T. Taniguchi, M. A. Kastner, and D. Goldhaber-Gordon, *Science* **365**, 605 (2019).
- [8] U. Zondiner, A. Rozen, D. Rodan-Legrain, Y. Cao, R. Queiroz, T. Taniguchi, K. Watanabe, Y. Oreg, F. von Oppen, A. Stern, E. Berg, P. Jarillo-Herrero, and S. Ilani, *Nature* **582**, 203 (2020).
- [9] K. Yang and S. Sachdev, *Phys. Rev. Lett.* **96**, 187001 (2006).
- [10] C. Wang, C. Gao, C. M. Jian, and H. Zhai, *Phys. Rev. Lett.* **105**, 160403 (2010).
- [11] C.-J. Wu, I. Mondragon-Shem, and X.-F. Zhou, *Chinese Phys. Lett.* **28**, 097102 (2011).
- [12] S. Gopalakrishnan, A. Lamacraft, and P. M. Goldbart, *Phys. Rev. A* **84**, 061604 (2011).
- [13] C. M. Jian and H. Zhai, *Phys. Rev. B* **84**, 060508 (2011).
- [14] R. Barnett, S. Powell, T. Graß, M. Lewenstein, and S. Das Sarma, *Phys. Rev. A* **85**, 023615 (2012).
- [15] T. A. Sedrakyan, A. Kamenev, and L. I. Glazman, *Phys. Rev. A* **86**, 063639 (2012).
- [16] E. Berg, M. S. Rudner, and S. A. Kivelson, *Phys. Rev. B* **85**, 035116 (2012).
- [17] X. Zhou, Y. Li, Z. Cai, and C. Wu, *J. Phys. B* **46**, 134001 (2013).
- [18] J. Ruhman and E. Berg, *Phys. Rev. B* **90**, 235119 (2014).
- [19] P. G. Silvestrov and O. Entin-Wohlman, *Phys. Rev. B* **89**, 155103 (2014).
- [20] T. A. Sedrakyan, L. I. Glazman, and A. Kamenev, *Phys. Rev. B* **89**, 201112 (2014).
- [21] T. A. Sedrakyan, L. I. Glazman, and A. Kamenev, *Phys. Rev. Lett.* **114**, 037203 (2015).
- [22] E. I. Rashba and V. I. Sheka, *Fiz. Tverd. Tela Collect. Pap.* **2**, 62 (1959).
- [23] Y. A. Bychkov and E. I. Rashba, *Pis'ma Zh. Eksp. Teor. Fiz.* **39**, 66 (1984).
- [24] M. Bukov, L. D'Alessio, and A. Polkovnikov, *Adv. Phys.* **64**, 139 (2015).
- [25] A. Eckardt, *Rev. Mod. Phys.* **89**, 011004 (2017).
- [26] T. Oka and S. Kitamura, *Annu. Rev. Condens. Matter Phys.* **10**, 387 (2019).
- [27] N. R. Cooper, J. Dalibard, and I. B. Spielman, *Rev. Mod. Phys.* **91**, 015005 (2019).
- [28] M. S. Rudner and N. H. Lindner, *Nat. Rev. Phys.* **2**, 229 (2020).
- [29] T. Oka and H. Aoki, *Phys. Rev. B* **79**, 081406 (2009).
- [30] J.-i. Inoue and A. Tanaka, *Phys. Rev. Lett.* **105**, 017401 (2010).
- [31] T. Kitagawa, E. Berg, M. Rudner, and E. Demler, *Phys. Rev. B* **82**, 235114 (2010).
- [32] N. H. Lindner, G. Refael, and V. Galitski, *Nat. Phys.* **7**, 490 (2011).
- [33] T. Kitagawa, T. Oka, A. Brataas, L. Fu, and E. Demler, *Phys. Rev. B* **84**, 235108 (2011).
- [34] N. H. Lindner, D. L. Bergman, G. Refael, and V. Galitski, *Phys. Rev. B* **87**, 235131 (2013).
- [35] A. Gómez-León and G. Platero, *Phys. Rev. Lett.* **110**, 200403 (2013).
- [36] J. Cayssol, B. Dóra, F. Simon, and R. Moessner, *Phys. Status Solidi RRL* **7**, 101 (2013).
- [37] G. Usaj, P. M. Perez-Piskunow, L. E. F. Foa Torres, and C. A. Balseiro, *Phys. Rev. B* **90**, 115423 (2014).
- [38] J. Klinovaja, P. Stano, and D. Loss, *Phys. Rev. Lett.* **116**, 176401 (2016).
- [39] R. Roy and F. Harper, *Phys. Rev. B* **96**, 155118 (2017).
- [40] A. Lubatsch and R. Frank, *Symmetry* **11**, 1246 (2019).
- [41] F. Harper, R. Roy, M. S. Rudner, and S. Sondhi, *Annu. Rev. Condens. Matter Phys.* **11**, 345 (2020).
- [42] M. S. Rudner, N. H. Lindner, E. Berg, and M. Levin, *Phys. Rev. X* **3**, 031005 (2013).
- [43] A. G. Grushin, Á. Gómez-León, and T. Neupert, *Phys. Rev. Lett.* **112**, 156801 (2014).
- [44] K. Sacha, *Phys. Rev. A* **91**, 033617 (2015).
- [45] V. Khemani, A. Lazarides, R. Moessner, and S. L. Sondhi, *Phys. Rev. Lett.* **116**, 250401 (2016).
- [46] D. V. Else, B. Bauer, and C. Nayak, *Phys. Rev. Lett.* **117**, 090402 (2016).
- [47] A. C. Potter, T. Morimoto, and A. Vishwanath, *Phys. Rev. X* **6**, 041001 (2016).
- [48] P. Titum, E. Berg, M. S. Rudner, G. Refael, and N. H. Lindner, *Phys. Rev. X* **6**, 021013 (2016).
- [49] C. W. von Keyserlingk and S. L. Sondhi, *Phys. Rev. B* **93**, 245145 (2016).
- [50] C. W. von Keyserlingk and S. L. Sondhi, *Phys. Rev. B* **93**, 245146 (2016).
- [51] H. C. Po, L. Fidkowski, T. Morimoto, A. C. Potter, and A. Vishwanath, *Phys. Rev. X* **6**, 041070 (2016).
- [52] D. V. Else and C. Nayak, *Phys. Rev. B* **93**, 201103 (2016).
- [53] S. Choi, J. Choi, R. Landig, G. Kucsko, H. Zhou, J. Isoya, F. Jelezko, S. Onoda, H. Sumiya, V. Khemani, C. von Keyserlingk, N. Y. Yao, E. Demler, and M. D. Lukin, *Nature* **543**, 221 (2017).
- [54] J. Zhang, P. W. Hess, A. Kyprianidis, P. Becker, A. Lee, J. Smith, G. Pagano, I.-D. Potirniche, A. C. Potter, A. Vishwanath, N. Y. Yao, and C. Monroe, *Nature* **543**, 217 (2017).
- [55] M. S. Rudner and J. C. Song, *Nat. Phys.* **15**, 1017 (2019).
- [56] Y. H. Wang, H. Steinberg, P. Jarillo-Herrero, and N. Gedik, *Science* **342**, 453 (2013).
- [57] M. C. Rechtsman, J. M. Zeuner, Y. Plotnik, Y. Lumer, D. Podolsky, F. Dreisow, S. Nolte, M. Segev, and A. Szameit, *Nature* **496**, 196 (2013).
- [58] G. Jotzu, M. Messer, R. Desbuquois, M. Lebrat,

- T. Uehlinger, D. Greif, and T. Esslinger, *Nature* **515**, 237 (2014).
- [59] M. Aidelsburger, M. Lohse, C. Schweizer, M. Atala, J. T. Barreiro, S. Nascimbène, N. R. Cooper, I. Bloch, and N. Goldman, *Nat. Phys.* **11**, 162 (2015).
- [60] M. Lohse, C. Schweizer, O. Zilberberg, M. Aidelsburger, and I. Bloch, *Nat. Phys.* **12**, 350 (2016).
- [61] F. Mahmood, C.-K. Chan, Z. Alpichshev, D. Gardner, Y. Lee, P. A. Lee, and N. Gedik, *Nat. Phys.* **12**, 306 (2016).
- [62] S. Nakajima, T. Tomita, S. Taie, T. Ichinose, H. Ozawa, L. Wang, M. Troyer, and Y. Takahashi, *Nat. Phys.* **12**, 296 (2016).
- [63] L. J. Maczewsky, J. M. Zeuner, S. Nolte, and A. Szameit, *Nat. Commun.* **8**, 13756 (2017).
- [64] N. Fläschner, D. Vogel, M. Tarnowski, B. S. Rem, D. S. Lühmann, M. Heyl, J. C. Budich, L. Mathey, K. Sengstock, and C. Weitenberg, *Nat. Phys.* **14**, 265 (2018).
- [65] J. W. McIver, B. Schulte, F. U. Stein, T. Matsuyama, G. Jotzu, G. Meier, and A. Cavalleri, *Nat. Phys.* **16**, 38 (2020).
- [66] T. Iadecola, D. Campbell, C. Chamon, C.-Y. Hou, R. Jackiw, S.-Y. Pi, and S. V. Kusminskiy, *Phys. Rev. Lett.* **110**, 176603 (2013).
- [67] H. Dehghani, T. Oka, and A. Mitra, *Phys. Rev. B* **90**, 195429 (2014).
- [68] T. Iadecola and C. Chamon, *Phys. Rev. B* **91**, 184301 (2015).
- [69] T. Iadecola, T. Neupert, and C. Chamon, *Phys. Rev. B* **91**, 235133 (2015).
- [70] K. I. Seetharam, C.-E. Bardyn, N. H. Lindner, M. S. Rudner, and G. Refael, *Phys. Rev. X* **5**, 041050 (2015).
- [71] D. E. Liu, *Phys. Rev. B* **91**, 144301 (2015).
- [72] H. Dehghani, T. Oka, and A. Mitra, *Phys. Rev. B* **91**, 155422 (2015).
- [73] M. Genske and A. Rosch, *Phys. Rev. A* **92**, 062108 (2015).
- [74] T. Shirai, T. Mori, and S. Miyashita, *Phys. Rev. E* **91**, 030101(R) (2015).
- [75] H. Dehghani and A. Mitra, *Phys. Rev. B* **93**, 205437 (2016).
- [76] T. Shirai, J. Thingna, T. Mori, S. Denisov, P. Hänggi, and S. Miyashita, *New J. Phys.* **18**, 053008 (2016).
- [77] K. Iwahori and N. Kawakami, *Phys. Rev. B* **94**, 184304 (2016).
- [78] I. Esin, M. S. Rudner, G. Refael, and N. H. Lindner, *Phys. Rev. B* **97**, 245401 (2018).
- [79] I. Esin, M. S. Rudner, and N. H. Lindner, (2019), [arXiv:1904.07856](https://arxiv.org/abs/1904.07856).
- [80] K. I. Seetharam, C.-E. Bardyn, N. H. Lindner, M. S. Rudner, and G. Refael, *Phys. Rev. B* **99**, 014307 (2019).
- [81] V. M. Galitskii, S. P. Goreslavskii, and V. F. Elesin, *Zh. Eksp. Teor. Fiz.* **57**, 207 (1969).
- [82] B. A. Bernevig, T. L. Hughes, and S.-C. Zhang, *Science* **314**, 1757 (2006).
- [83] More realistic time-dependent electromagnetic fields can be incorporated in this model, see [32].
- [84] We assume here only the ferromagnetic phase, which we can easily treat within the Hartree-Fock analysis. We leave the analysis of the nematic paramagnetic phase, which can potentially emerge in our system [16, 18], for future studies.
- [85] G. D. Mahan, *Many-Particle Physics* (Springer, New York, 2000).
- [86] M. S. Rudner and N. H. Lindner, (2020), [arXiv:2003.08252](https://arxiv.org/abs/2003.08252).
- [87] The electron-hole pair annihilation processes predominantly occur near the resonance ring, where the electrons and holes are concentrated. Note that for these momenta the Floquet states are equal superpositions of the conduction and valence bands [see Eq. (9)], and these states are efficiently coupled by acoustic phonons.
- [88] E. C. Stoner, *Proc. R. Soc. A* **165**, 372 (1938).
- [89] E. C. Stoner, *Proc. R. Soc. A* **169**, 339 (1939).
- [90] Such a fine-tuning of the next-nearest neighbor hopping parameters helps to reduce lattice modulations of the resonance ring. The latter lift the degeneracy at the resonance ring, thus removing the divergence of the DOS essential for satisfying the Stoner criterion.
- [91] Such a choice provides non-inverted bands of the semiconductor.
- [92] S. K. Sundaram and E. Mazur, *Nat. Mater.* **1**, 217 (2002).
- [93] T. A. Sedrakyan, V. M. Galitski, and A. Kamenev, *Phys. Rev. Lett.* **115**, 195301 (2015).
- [94] K. Wintersperger, C. Braun, F. N. Ünal, A. Eckardt, M. Di Liberto, N. Goldman, I. Bloch, and M. Aidelsburger, (2020), [arXiv:2002.09840](https://arxiv.org/abs/2002.09840).

Electronic Floquet Liquid Crystals - Supplemental Material

This supplemental material provides detailed analytical derivations discussed in the paper and explains key aspects of the numerical simulations. Throughout the notes we work in natural units in which $\hbar = k_B = 1$.

I. EFFECTIVE TWO-BAND FLOQUET HAMILTONIAN

Here we derive an effective time-independent Hamiltonian in the rotating wave approximation (RWA), $H_{\text{RWA}}(\mathbf{k})$ for the periodically driven system described by Eq. (1) in the main text, without the interaction part. Our goal is to find the effective dispersion and eigenstates near the resonance ring. The time-dependent Hamiltonian is given by $H(\mathbf{k}, t) = H_0(\mathbf{k}) + H_d(t)$, where $H_0(\mathbf{k}) = E_0 + \mathbf{d}(\mathbf{k}) \cdot \boldsymbol{\sigma}$, with

$$\mathbf{d}(\mathbf{k}) = \left(\lambda_0 k_x, \lambda_0 k_y, \frac{|\mathbf{k}|^2}{2m_*} + \frac{E_g}{2} \right), \quad (\text{S1})$$

and $H_d(t) = \mathbf{v} \cdot \boldsymbol{\sigma} \cos(\Omega t)$, where $\mathbf{v} = (0, 0, V)$. In the RWA, we shift the lower (upper) bands by $\pm\Omega/2$ and then neglect rapidly oscillating terms. The operator that shifts the energies reads

$$\mathcal{U}_R(\mathbf{k}, t) = e^{\frac{i\Omega t}{2} \hat{\mathbf{d}}(\mathbf{k}) \cdot \boldsymbol{\sigma}}, \quad (\text{S2})$$

where $\hat{\mathbf{d}}(\mathbf{k})$ is a unit vector in the direction $\mathbf{d}(\mathbf{k})$. The transformed Hamiltonian, $H_R(\mathbf{k}, t)$, then reads

$$H_R(\mathbf{k}, t) = \mathcal{U}_R(\mathbf{k}, t) H(\mathbf{k}, t) \mathcal{U}_R^\dagger(\mathbf{k}, t) - i \mathcal{U}_R \frac{\partial \mathcal{U}_R^\dagger}{\partial t}. \quad (\text{S3})$$

Note that \mathcal{U}_R commutes with H_0 , but does not commute with the time-derivative and the driving field. Using the explicit form of $H(\mathbf{k}, t)$, we arrive at

$$H_R = E_0 + (|\mathbf{d}| - \Omega/2) \hat{\mathbf{d}} \cdot \boldsymbol{\sigma} + \mathbf{v}'(t) \cdot \boldsymbol{\sigma} \cos(\Omega t), \quad (\text{S4})$$

where $\mathbf{v}'(t) = \mathbf{v} \cos(\Omega t) - \hat{\mathbf{d}} \times \mathbf{v} \sin(\Omega t) + \hat{\mathbf{d}}(\hat{\mathbf{d}} \cdot \mathbf{v})(1 - \cos(\Omega t))$, following from the Rodrigues' formula of rotation of \mathbf{v} around $\hat{\mathbf{d}}$. The last term in Eq. (S4) has constant in time parts and parts oscillating with the frequency Ω and 2Ω . Following RWA, we omit the time-oscillating terms, leading to

$$H_{\text{RWA}}(\mathbf{k}) = E_0 + \mathbf{d}_F(\mathbf{k}) \cdot \boldsymbol{\sigma}, \quad (\text{S5})$$

where $\mathbf{d}_F = (|\mathbf{d}| - \Omega/2) \hat{\mathbf{d}} + \frac{1}{2}[\mathbf{v} - \hat{\mathbf{d}}(\hat{\mathbf{d}} \cdot \mathbf{v})]$. The spectrum of H_{RWA} then reads, $\varepsilon_{\mathbf{k}\pm} = E_0 \pm \varepsilon_{\mathbf{k}}$, where

$$\varepsilon_{\mathbf{k}} = \sqrt{(|\mathbf{d}| - \Omega/2)^2 + |\mathbf{v} - \hat{\mathbf{d}}(\hat{\mathbf{d}} \cdot \mathbf{v})|^2/4}. \quad (\text{S6})$$

For simplicity of notations, throughout we set $E_0 = 0$. To leading order in V/Ω and $\lambda_0^2 m/E_g$, the minimum of

the upper band is positioned at the resonance ring, given by $|\mathbf{d}(\mathbf{k})| = \Omega/2$. The radius of the resonance ring is given by $k_R = \sqrt{m_* \delta E}$ and the quasienergy gap at $|\mathbf{k}| = k_R$ reads $\Delta_F = 2V\lambda_0 k_R/\Omega$. We thus approximate the quasienergy as

$$\varepsilon_{\mathbf{k}} \approx \sqrt{\left(\frac{k^2}{2m_*} - \frac{\delta E}{2}\right)^2 + \left(\frac{\Delta_F k}{2k_R}\right)^2}, \quad (\text{S7})$$

where $k \equiv |\mathbf{k}|$.

The eigenstates of H_{RWA} read

$$|\phi'_{\mathbf{k}\pm}\rangle = \frac{1}{\sqrt{2}} \left(\sqrt{1 \pm \hat{\mathbf{z}} \cdot \hat{\mathbf{d}}_F} |\uparrow\rangle \mp e^{i\theta_{\mathbf{k}}} \sqrt{1 \mp \hat{\mathbf{z}} \cdot \hat{\mathbf{d}}_F} |\downarrow\rangle \right). \quad (\text{S8})$$

where $\theta_{\mathbf{k}} = \tan^{-1}(k_y/k_x)$ and $\hat{\mathbf{d}}_F$ is a unit vector in the direction of \mathbf{d}_F , defined in Eq. (S5).

At the resonance ring, $\hat{\mathbf{d}}_F$ approximately lies in the $x-y$ plane such that $\hat{\mathbf{z}} \cdot \hat{\mathbf{d}}_F \approx 0$, therefore

$$|\phi'_{\mathbf{k}\pm}\rangle \Big|_{|\mathbf{k}|=k_R} = \frac{1}{\sqrt{2}} (|\uparrow\rangle \mp e^{i\theta_{\mathbf{k}}} |\downarrow\rangle). \quad (\text{S9})$$

To find the time-dependent eigenstates of $H(\mathbf{k}, t)$ within the RWA in the lab frame, we apply the inverse transformation, \mathcal{U}_R^\dagger on the states, $|\phi'_{\mathbf{k}\pm}\rangle$. Approximating, $\mathcal{U}_R^\dagger \approx e^{-\frac{i\Omega t}{2} \sigma^z}$, we arrive at

$$|\phi_{\mathbf{k}\pm}(t)\rangle \Big|_{|\mathbf{k}|=k_R} = \frac{1}{\sqrt{2}} (e^{-i\Omega t} |\uparrow\rangle \mp e^{i\theta_{\mathbf{k}}} |\downarrow\rangle). \quad (\text{S10})$$

II. DERIVATION OF U_c

In this section we solve the mean-field equation [Eq. (2) in the main text] in the limit $\mathbf{h}(t) \rightarrow 0$. The solution in this limit provides the minimal interaction strength required for non-zero magnetization, U_c [Eq. (10) in the main text]. In our analysis we assume contact interactions, $\mathcal{V}_{\mathbf{k}} = U/\varpi$, and take only the first harmonic of the circularly polarized magnetization field,

$$\mathbf{h}(t) = h_1 e^{i\Omega t} (\hat{\mathbf{x}} - i\hat{\mathbf{y}})/2 + c.c., \quad (\text{S11})$$

as discussed in the main text [see Eq. (8)], where h_1 is real and positive. In the rotating frame of reference such a term reads $\mathcal{U}_R(\mathbf{h}(t) \cdot \boldsymbol{\sigma}) \mathcal{U}_R^\dagger = h_1 \sigma^x$.

We first rewrite Eq. (2) in the main text in terms of the single particle states and the distribution function, $f_{\mathbf{k}\nu}$,

$$\mathbf{h}(t) = -U \sum_{\nu=\pm} \int \frac{d^2 \mathbf{k}}{(2\pi)^2} \langle \phi_{\mathbf{k}\nu}(t) | \boldsymbol{\sigma} | \phi_{\mathbf{k}\nu}(t) \rangle f_{\mathbf{k}\nu}. \quad (\text{S12})$$

We approximate $|\phi_{\mathbf{k}\nu}(t)\rangle$ by eigenstates of the rotating-wave approximated mean-field Hamiltonian [Eq. (3)

in the main text] in the lab frame, given by $H_{\text{MF,RWA}}(\mathbf{k}, t) = \mathcal{U}_{\text{R}}^\dagger H'_{\text{MF,RWA}}(\mathbf{k}) \mathcal{U}_{\text{R}}$, where

$$H'_{\text{MF,RWA}}(\mathbf{k}) = H_{\text{RWA}}(\mathbf{k}) + h_1 \sigma^x; \quad (\text{S13})$$

$H_{\text{RWA}}(\mathbf{k})$ is given in Eq. (S5).

Next, we transform Eq. (S12) given in a vector form, into a scalar equation for a single mode amplitude, h_1 , defined in Eq. (S11). To this end, we transform the Floquet states into a rotating frame of reference, leading to

$$h(t) = -U \sum_{\nu=\pm} \int \frac{d^2\mathbf{k}}{(2\pi)^2} \langle \phi'_{\mathbf{k}\nu} | \mathcal{U}_{\text{R}} \sigma \mathcal{U}_{\text{R}}^\dagger | \phi'_{\mathbf{k}\nu} \rangle f_{\mathbf{k}\nu}. \quad (\text{S14})$$

Here $|\phi'_{\mathbf{k}\nu}\rangle \equiv \mathcal{U}_{\text{R}}(\mathbf{k}, t) |\phi_{\mathbf{k}\nu}(t)\rangle$ are the eigenstates of $H'_{\text{MF,RWA}}(\mathbf{k})$, given in Eq. (S13). Using the Rodrigues' formula, we find, $\mathcal{U}_{\text{R}}(\mathbf{k}, t) \sigma \mathcal{U}_{\text{R}}^\dagger(\mathbf{k}, t) = \sigma \cos(\Omega t) + \hat{\mathbf{d}} \times \sigma \sin(\Omega t) + \hat{\mathbf{d}}(\hat{\mathbf{d}} \cdot \sigma)(1 - \cos(\Omega t))$. We extract only the components proportional to $e^{i\Omega t}$, and multiply both sides of Eq. (S14) by $(\hat{x} + i\hat{y})/\sqrt{2}$. Approximating $\hat{\mathbf{d}} \approx \hat{\mathbf{z}}$, we find

$$\frac{h_1}{\sqrt{2}} = -U \sum_{\nu=\pm} \int \frac{d^2\mathbf{k}}{(2\pi)^2} \langle \phi'_{\mathbf{k}\nu} | \frac{\sigma^x + i\sigma^y}{\sqrt{2}} | \phi'_{\mathbf{k}\nu} \rangle f_{\mathbf{k}\nu}, \quad (\text{S15})$$

where $f_{\mathbf{k}\nu}$ is the particle distribution function. As $H'_{\text{MF,RWA}}(\mathbf{k})$ is symmetric to reflections of the y -axis, the expectation value of σ^y vanishes, leading to

$$h_1 = -U \sum_{\nu=\pm} \int \frac{d^2\mathbf{k}}{(2\pi)^2} \langle \phi'_{\mathbf{k}\nu} | \sigma^x | \phi'_{\mathbf{k}\nu} \rangle f_{\mathbf{k}\nu}. \quad (\text{S16})$$

To evaluate the integral in Eq. (S16), in what follows we assume a low-excitation steady-state corresponding to almost-full lower Floquet band and low density of electron and hole excitations in the bottom of the upper and top of the lower Floquet bands, respectively. We then split the integral into two contributions, $h_1 = h_1^{\text{fb}} + h_1^{\text{ex}}$. Here, h_1^{fb} is the contribution of the full lower Floquet band,

$$h_1^{\text{fb}} = -U \int \frac{d^2\mathbf{k}}{(2\pi)^2} \langle \phi'_{\mathbf{k}-} | \sigma^x | \phi'_{\mathbf{k}-} \rangle, \quad (\text{S17})$$

and h_1^{ex} is the contribution of the electron and hole excitations,

$$h_1^{\text{ex}} = -U \sum_{\nu} \int \frac{d^2\mathbf{k}}{(2\pi)^2} \langle \phi'_{\mathbf{k}\nu} | \sigma^x | \phi'_{\mathbf{k}\nu} \rangle \delta f_{\mathbf{k}\nu}, \quad (\text{S18})$$

where $\delta f_{\mathbf{k}+} \equiv f_{\mathbf{k}+}$ corresponds to electrons and $\delta f_{\mathbf{k}-} \equiv 1 - f_{\mathbf{k}-}$ to holes.

We begin with h_1^{ex} . Recall that the Floquet states and quasienergies result from the solution of the mean-field Hamiltonian [Eq. (S13)], and therefore depend (implicitly) on h_1 . As we are interested in the regime near the critical value ($U \sim U_c$), where h_1 is small, we expand the states $\{|\phi'_{\mathbf{k}\nu}\rangle\}$ in the integrand in Eq. (S18) in powers of

h_1 around $h_1 = 0$. The zeroth-order term in h_1 is proportional to $\langle \phi'_{\mathbf{k}\nu} | \sigma^x | \phi'_{\mathbf{k}\nu} \rangle \delta f_{\mathbf{k}\nu}|_{h_1=0}$. This contribution vanishes, as it consists of the momentum integral over an odd-parity function (arising from the symmetry to reflections of the x -axis, exhibited by $H'_{\text{MF,RWA}}$ at $h_1 = 0$). The contribution to linear order in h_1 includes two terms: the first one is proportional to $h_1 \left[\frac{\partial \langle \phi'_{\mathbf{k}\nu} | \sigma^x | \phi'_{\mathbf{k}\nu} \rangle}{\partial h_1} \delta f_{\mathbf{k}\nu} \right]_{h_1=0}$ and the second to $h_1 \left[\frac{\partial \delta f_{\mathbf{k}\nu}}{\partial h_1} \langle \phi'_{\mathbf{k}\nu} | \sigma^x | \phi'_{\mathbf{k}\nu} \rangle \right]_{h_1=0}$. In the limit of low filling, the momentum integral over the first term is proportional to the density of particles in the upper band, while the momentum integral over the second term is proportional to the inverse of the density (see below). Therefore, in the low-density limit, considered throughout, we neglect the first term (arising from the dependence of the eigenstates on h_1) with respect to the second one (which captures the change of the distribution function due to h_1).

In order to compute $\frac{\partial \delta f_{\mathbf{k}\nu}}{\partial h_1}|_{h_1=0}$, we approximate the distribution function by the Fermi function

$$\delta f_{\mathbf{k}\pm} \approx [1 + e^{(\varepsilon_{\mathbf{k}} - \Delta_{\text{F}}/2 - \mu_{\text{e/h}})/T_{\text{e/h}}}]^{-1}. \quad (\text{S19})$$

Here we used the particle-hole symmetry of the system, where $\varepsilon_{\mathbf{k}}$ is the dispersion relation of the upper Floquet band [cf. Eq. (S7) for $h_1 = 0$ case]. Note that the effective temperature, $T_{\text{e/h}}$, and the effective chemical potential, $\mu_{\text{e/h}}$, must be even functions of h_1 , as the setting $h_1 \rightarrow -h_1$ inverts the position of the band minimum in the momentum space, but does not change the overall energetics of the system. Therefore, the linear-order dependence of $\delta f_{\mathbf{k}\nu}$ on h_1 results predominantly from the dependence of $\varepsilon_{\mathbf{k}}$ on h_1 . We find this dependence using first-order perturbation theory, $\varepsilon_{\mathbf{k}} = \varepsilon_{0,\mathbf{k}} + h_1 \langle \phi'_{0,\mathbf{k}+} | \sigma^x | \phi'_{0,\mathbf{k}+} \rangle + \mathcal{O}(h_1^2)$, where $|\phi'_{0,\mathbf{k}\nu}\rangle \equiv |\phi'_{\mathbf{k}\nu}\rangle|_{h_1=0}$, and $\varepsilon_{0,\mathbf{k}} \equiv \varepsilon_{\mathbf{k}}|_{h_1=0}$. Finally, using the chain rule, we arrive at $\frac{\partial \delta f_{\mathbf{k}\nu}}{\partial h_1}|_{h_1=0} = \frac{\partial \delta f_{\mathbf{k}\nu}^0}{\partial \varepsilon_{0,\mathbf{k}}} \langle \phi'_{0,\mathbf{k}+} | \sigma^x | \phi'_{0,\mathbf{k}+} \rangle$, where $\delta f_{\mathbf{k}\nu}^0 \equiv \delta f_{\mathbf{k}\nu}|_{h_1=0}$ [see Eq. (S19)]. To make the notations more transparent, throughout we distinguish between rotation-symmetric functions (dependent only on the momentum amplitude) with index k , and functions of momentum amplitude and angle with index \mathbf{k} .

We substitute the result of the expansion in small h_1 back into Eq. (S18), yielding

$$h_1^{\text{ex}} = -h_1 U \sum_{\nu} \int \frac{d^2\mathbf{k}}{(2\pi)^2} \frac{\partial \delta f_{\mathbf{k}\nu}^0}{\partial \varepsilon_{0,\mathbf{k}}} |\langle \phi'_{0,\mathbf{k}+} | \sigma^x | \phi'_{0,\mathbf{k}+} \rangle|^2. \quad (\text{S20})$$

To evaluate the integral in Eq. (S20), we use polar coordinates $\mathbf{k} = k(\cos \theta, \sin \theta)$, yielding

$$h_1^{\text{ex}} = -h_1 U \sum_{\nu} \int \frac{k dk}{2\pi} \frac{\partial \delta f_{\mathbf{k}\nu}^0}{\partial \varepsilon_{0,\mathbf{k}}} \overline{\sigma_k^2}, \quad (\text{S21})$$

where $\overline{\sigma_k^2} \equiv \int \frac{d\theta}{2\pi} |\langle \phi'_{0,\mathbf{k}+} | \sigma^x | \phi'_{0,\mathbf{k}+} \rangle|^2$. To further simplify the expression, we approximate $\overline{\sigma_k^2}$ by its value at the resonance ring, $\overline{\sigma_{k_{\text{R}}}^2}$. Corrections to this approximation lead

to higher order terms in the density of excitations, and hence are small in the low-density limit. We transform the integral over the magnitude of the momentum k , in Eq. (S21) to an integral over energy ε , by introducing the density of states $D_F(\varepsilon) \equiv \int \frac{d^2\mathbf{k}}{(2\pi)^2} \delta(\varepsilon - \varepsilon_{0,\mathbf{k}} + \Delta_F/2)$. These transformations lead to

$$h_1^{\text{ex}} \approx -h_1 U \overline{\sigma_{k_R}^2} \sum_{\nu=\pm} \int_0^\infty d\varepsilon D_F(\varepsilon) \partial_\varepsilon \delta f_{\varepsilon\nu}^0, \quad (\text{S22})$$

where $\delta f_{\varepsilon\pm}^0 = [1 + e^{(\varepsilon - \mu_{e/h})/T_{e/h}}]^{-1}$, cf. Eq. (S19). We estimate the density of states near the band bottom by

$$D_F(\varepsilon) \approx D_0 \sqrt{\Delta_F/\varepsilon}, \quad (\text{S23})$$

where D_0 is a constant depending on the parameters of the Floquet bands. In terms of the bare parameters of the model, we evaluate $D_0 = m_*/2\pi$. We use the eigenstates given in Eq. (S9) to evaluate, $\overline{\sigma_{k_R}^2} = \frac{1}{2}$.

To perform the energy integral in Eq. (S22), we define a dimensionless integration variable. For $\nu = +$ term, we define $x = \varepsilon/T_e$. The integral then reads $\int_0^\infty d\varepsilon D_F(\varepsilon) \partial_\varepsilon \delta f_{\varepsilon+}^0 = D_F(T_e) \int_0^\infty \frac{dx}{\sqrt{x}} \partial_x \frac{1}{1+e^{x-(\mu_e/T_e)}} = \sqrt{\pi} D_F(T_e) \text{Li}_{-1/2}(-e^{\mu_e/T_e})$, where $\text{Li}_s(z)$ is the polylogarithm function¹. To bring this result into the form of Eq. (10), we replace the term proportional to the temperature by $\sqrt{T_e} = -n_e/[\sqrt{\pi} \Delta_F D_0 \text{Li}_{1/2}(e^{-\mu_e/T_e})]$. The last relation follows from the definition of the electron density $n_e = \int d\varepsilon D_F(\varepsilon) \delta f_{\varepsilon+}^0 = -\sqrt{\pi} T_e D_F(T_e) \text{Li}_{1/2}(e^{-\mu_e/T_e})$. We repeat the same calculation for the lower band ($\nu = -$), to arrive at

$$h_1^{\text{ex}} = h_1 U U_{\text{ex}}^{-1} \left(\frac{\tilde{\Theta}(\mu_e/T_e)}{n_e/\mathcal{A}_R} + \frac{\tilde{\Theta}(\mu_h/T_h)}{n_h/\mathcal{A}_R} \right). \quad (\text{S24})$$

Here $U_{\text{ex}}^{-1} = \frac{2\overline{\sigma_{k_R}^2} \Delta_F D_0^2/\mathcal{A}_R}{\pi \text{Li}_{-1/2}(-e^x) \text{Li}_{1/2}(-e^x)}$ and $\tilde{\Theta}(x) \equiv \frac{\pi}{2} \text{Li}_{-1/2}(-e^x) \text{Li}_{1/2}(-e^x)$, see Fig. S1.

Now, we turn to the evaluation of h_1^{fb} given in Eq. (S17). In contrast to the integral in Eq. (S18), which is limited to an area in k -space near the resonance ring, the integral in Eq. (S17) is defined over the entire Brillouin zone. The dependence on h_1 arises from the dependence of Floquet states $\{|\phi'_{\mathbf{k}\nu}\rangle\}$ on h_1 . Using first order perturbation theory, we find $|\phi'_{\mathbf{k}-}\rangle = |\phi'_{0,\mathbf{k}-}\rangle - h_1 \frac{\langle \phi'_{0,\mathbf{k}+} | \sigma^x | \phi'_{0,\mathbf{k}-} \rangle}{2\varepsilon_{\mathbf{k}}} |\phi'_{0,\mathbf{k}+}\rangle$. Employing this expansion of the Floquet states, we express the linear order term in h_1 of Eq. (S17) as

$$h_1^{\text{fb}} = h_1 U \int \frac{d^2\mathbf{k}}{(2\pi)^2} \frac{|\langle \phi'_{0,\mathbf{k}-} | \sigma^x | \phi'_{0,\mathbf{k}+} \rangle|^2}{\varepsilon_{\mathbf{k}}}. \quad (\text{S25})$$

This integral is independent of the steady-state distribution [by the definition, see Eq. (S17)]. We denote the value of this integral by $U_{\text{fb}}^{-1} = \int \frac{d^2\mathbf{k}}{(2\pi)^2} |\langle \phi'_{0,\mathbf{k}-} | \sigma^x | \phi'_{0,\mathbf{k}+} \rangle|^2 / \varepsilon_{\mathbf{k}}$.

To evaluate U_{fb} , we first note that the mean-field Hamiltonian, $H_{\text{MF}}(\mathbf{k}, t)$ (see Eq. (3) in the main text)

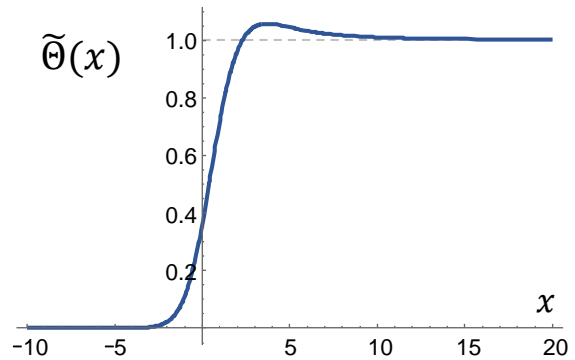


FIG. S1. A plot of the smeared step function $\tilde{\Theta}(x) \equiv \frac{\pi}{2} \text{Li}_{-1/2}(-e^x) \text{Li}_{1/2}(-e^x)$, appearing in Eq. (10) in the main text.

describes the system only near the Γ -point, while the integral in the definition of U_{fb} is over the entire Brillouin zone. To address this issue, we impose a cutoff in the integral at the momentum Λ , as a stand-in for the Brillouin zone edge. We evaluate the wavefunctions using Eq. (S8), where we approximate $\hat{\mathbf{z}} \cdot \hat{\mathbf{d}}_F \approx (k^2/2m_* - \delta E/2)/\varepsilon_{\mathbf{k}}$, with $\varepsilon_{\mathbf{k}}$ given by Eq. (S7). Substituting in Eq. (S25) we find

$$U_{\text{fb}}^{-1} = \frac{m_*}{2\pi} \left[\log \left(\frac{4E_{\text{BW}}}{\delta E - k_R^2/m_*} \right) - 1 \right], \quad (\text{S26})$$

where we denote $E_{\text{BW}} = \varepsilon_{\mathbf{k}}|_{k=\Lambda}$.

Summing Eqs. (S24) and (S25) we arrive at

$$h_1 = h_1 U \left[U_{\text{ex}}^{-1} \left(\frac{\tilde{\Theta}(\mu_e/T_e)}{n_e/\mathcal{A}_R} + \frac{\tilde{\Theta}(\mu_h/T_h)}{n_h/\mathcal{A}_R} \right) + U_{\text{fb}}^{-1} \right]. \quad (\text{S27})$$

Note that h_1 appears on the both sides of Eq. (S27). Dividing by h_1 and by U , we obtain the expression for U_c given in Eq. (10) in the main text.

The calculation outlined in this section helps to find the critical value of U by expanding the self-consistent equation [Eq. (2) in the main text] to the linear order in the order parameter. Expanding this equation to higher orders in h_1 reveals how the order parameter grows as a function of U .

III. THE EXTENDED RATE MODEL

In this section, we give a detailed description of the extended rate model. The results of the model are used to fit the numerical data of μ_e/T_e in Fig. 3 in the main text and to estimate the heating rates in the discussion section. We partially follow the analysis of Ref. 2. Throughout this section, we consider the ‘‘paramagnetic phase’’, with no spontaneous symmetry breaking, corresponding to $U \leq U_c$. In our analysis, we assume that the system

reached a steady state with a low-density of electrons (n_e) in the upper Floquet band (UFB) and holes (n_h) in the lower Floquet band (LFB), $n_e, n_h \ll \mathcal{A}_R$. We verified numerically that the distributions of each of the bands can be well approximated by Fermi functions with effective parameters, see Fig. S9.

Here we consider only an electron-doped case ($\Delta n > 0$); the analysis of the hole-doped system is similar due to particle-hole symmetry of the Hamiltonian. We distinguish between two cases: (i) The electrons form a degenerate Fermi gas ($\mu_e/T_e \gg 1$) featuring two concentric Fermi surfaces. We refer to this case as the electron Floquet metal (EFM) phase (see Fig. S2). In this phase we evaluate energy integrals using the Sommerfeld expansion³. (ii) Non-degenerate distribution of electrons ($\mu_e/T_e < 0$) referred to as the electron Floquet insulator (EFI) phase. In this phase, we approximate the distribution by the Maxwell's law

$$f_{\varepsilon+} = z_e e^{-\varepsilon/T_e}, \quad (\text{S28})$$

where $z_e = e^{-|\mu_e|/T_e}$ is the electron fugacity and ε is accounted from the UFB bottom. The two phases are separated by a crossover regime, $\mu_e \approx T_e$, where our analysis does not apply. Yet, as we show below, an analytic interpolation between the EFM and the EFI phases gives a good agreement with the numerical data (see Fig. 3 in the main text). We also show below that for the system considered in this paper, the holes always form a non-degenerate distribution in the electron-doped system. Therefore we approximate the distribution of holes by $\bar{f}_{\varepsilon-} \equiv 1 - f_{\varepsilon-}$, where

$$\bar{f}_{\varepsilon-} = z_h e^{\varepsilon/T_h}. \quad (\text{S29})$$

Here ε is accounted from the LFB top and $z_h = e^{-|\mu_h|/T_h}$ is the hole fugacity.

In what follows, we seek four equations for four variables, μ_e , μ_h , T_e , and T_h . Two of the equations [Eqs. (S34) and (S35)] determine the total densities of electrons and holes, n_e and n_h (identical to the derivation of Eq. (7) in the main text). The other two equations [Eqs. (S44) and (S45)], are rate equations for the densities of subpopulations (defined below) of the electron and hole distributions. The rate equations include the key processes leading to the steady-state distribution due to electron-phonon, electron-photon and electron-electron interactions, see Fig. S3. Our goal is to find the electron and hole densities and the densities of their subpopulations as functions of the rates in the steady state, and use them to find the chemical potentials and temperatures of the hole and electron distribution. The total densities are related to the parameters of the distribution through

$$n_e = \int \frac{d^2 \mathbf{k}}{(2\pi)^2} f_{\mathbf{k}+}, \quad n_h = \int \frac{d^2 \mathbf{k}}{(2\pi)^2} (1 - f_{\mathbf{k}-}). \quad (\text{S30})$$

We perform the momentum integral, when the electronic population is deep in the EFM phase, to estimate

$$n_e \approx 2\mu_e D_F(\mu_e), \quad (\text{S31})$$

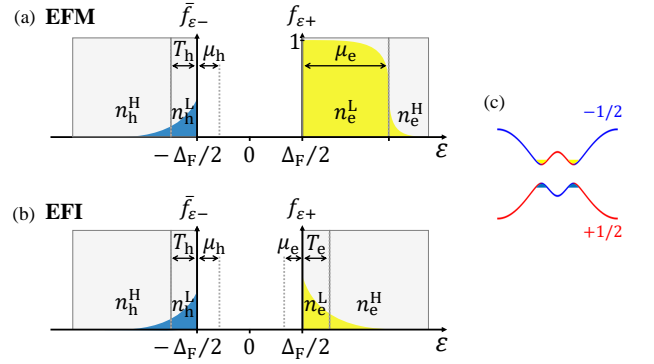


FIG. S2. Population at the bottom of the UFB and top of the LFB in the EFM and EFI phases. The yellow area indicates population of electrons and the blue area of holes. (a). Distribution in the EFM phase. The electrons exhibit a sharp Fermi-surface at the effective chemical potential μ_e . We denote densities of subpopulations occupying levels below and above the Fermi surface by n_e^L and n_e^H , respectively. (b). Distribution of electrons and holes in the EFI phase. The effective chemical potential of the electrons is in the Floquet gap, giving rise to a Maxwell distribution, given by Eq. (S28). In this case, the low and high-quasienergy populations occupy states below and above the effective temperature. The population of holes in an electron-doped system is always in the non-degenerate phase described by Eq. (S29). (c). Schematic drawing of the Floquet bands. The red/blue colored sectors indicates the character of the original valence/conduction bands. The color code helps to visually estimate the power n of the factor $(V/\Omega)^{2n}$ multiplying a scattering rate for the l th order Floquet Umklapp process. The power is given by $n = |l + m_i - m_f|$, where $m_i = 1/2$ when the state before the scattering is in the red sector and $m_i = -1/2$ when it is in the blue sector, similarly, m_f denotes the sector after the scattering.

where D_F is given in Eq. (S23). In the EFI phase, we perform the integral in Eq. (S30) using the Maxwell's distribution [see Eq. (S28)], leading to

$$n_e \approx z_e \sqrt{\pi} T_e D_F(T_e). \quad (\text{S32})$$

Likewise, we estimate the hole density [using Eqs. (S30) and (S29)] by

$$n_h \approx z_h \sqrt{\pi} T_h D_F(T_h). \quad (\text{S33})$$

Later in this section, we use the estimates of the densities in terms of the temperature and chemical potential to find the electron and hole temperatures as functions of the parameters of the electronic dispersion in the material, the periodic drive, and the heat-baths.

A. Equations determining the steady-state densities of the electrons and holes

Our first equation relates the total densities of electrons and holes with the doping,

$$n_e - n_h = \Delta n. \quad (\text{S34})$$

While the doping sets the difference between the densities of electrons and holes, it does not resolve the density of each of them. Indeed, even at zero doping, non-zero densities of electrons and holes can be created by the drive due to excitation processes. In fact, the populations of the bands are determined by the balance between the processes transferring electrons from the LFB to the UFB (which we will refer to as heating processes), and processes transferring particles from the UFB to LFB (which we will refer to as cooling processes). The heating processes arise from electron-photon, electron-phonon and electron-electron scattering. We capture the effect of each of these processes by a single parameter Γ_ℓ , Γ_s , and Γ_{ee} , cf. Fig. S3a-c, which we estimate in Secs. III D 1-III D 3.

The interband cooling processes are dominated by electron-hole recombination assisted by phonons. We expect the recombination rate to be proportional to the densities of electrons, n_e and holes, n_h (cf. Fig. S3d). Therefore, we estimate $\dot{n}_e|_{\text{cool}} = -\Lambda_{\text{inter}} n_e n_h$, see Sec. III E for the evaluation of Λ_{inter} . The interplay of these processes is captured by the rate equation for n_e ,

$$\dot{n}_e = \Gamma_\ell + \Gamma_s + \Gamma_{ee} - \Lambda_{\text{inter}} n_e n_h, \quad (\text{S35})$$

satisfying $\dot{n}_e = 0$ in the steady state. Note that from the conservation of particles, $\dot{n}_h = -\dot{n}_e$. In the steady state ($\dot{n}_e = 0$), Eq. (S35) yields

$$n_e n_h = \kappa, \quad (\text{S36})$$

where we defined,

$$\kappa \equiv \frac{\Gamma_\ell + \Gamma_s + \Gamma_{ee}}{\Lambda_{\text{inter}}}. \quad (\text{S37})$$

Combining Eqs. (S34) and (S36), we arrive at the total densities of electrons and holes in the UFB and LFB,

$$n_{e/h} = \sqrt{(\Delta n/2)^2 + \kappa} \pm \Delta n/2, \quad (\text{S38})$$

similar to Eq. (7) in the main text.

B. Equations determining the effective temperatures of the electron and hole distributions

Eq. (S38) yields the total density of electrons and holes, but provides no information on how the particles are distributed within each of the bands. In order to obtain the quasienergy-resolved structure of the distribution in the UFB, we split the electronic population to

two subpopulations². We define a subpopulation occupying low-quasienergy levels close to the bottom of the UFB as

$$n_e^L = \int_{\Delta_F/2}^{\Delta_F/2 + E_s} D_F(\varepsilon - \Delta_F/2) f_{\varepsilon+} d\varepsilon \quad (\text{S39})$$

where D_F is the density of states, given in Eq. (S23). We furthermore define a complementary subpopulation corresponding to electrons in quasienergy levels not included in Eq. (S39). The density of this subpopulation is given by $n_e^H = n_e - n_e^L$. In the EFM, we choose $E_s = \mu_e$ and in the EFI $E_s = T_e$, see Figs. S2a and b for an illustration. A different choice of E_s in the EFI phase, leads to renormalization of the coefficients in the phenomenological model (see below), but does not change the final result. The splitting into subpopulations makes it possible to study intraband processes in terms of rate equations for the densities of the subpopulations. It is also convenient to define the density of unoccupied states in the low-quasienergy subset of the UFB, denoted by \bar{n}_e^L . The definition of \bar{n}_e^L is similar to Eq. (S39), where we replace $f_{\varepsilon+}$ by $1 - f_{\varepsilon+}$. When the electrons are deep in the EFM phase, we evaluate their subpopulations [using Eq. (S39)] by

$$n_e^H \approx \bar{n}_e^L \approx \log(2) T_e D_F(\mu_e) \text{ and } n_e^L \approx n_e, \quad (\text{S40})$$

where n_e is given in Eq. (S31). In turn, when the electrons exhibit the EFI phase, we evaluate

$$n_e^L \approx \text{erf}(1) n_e, \quad n_e^H \approx \text{erfc}(1) n_e \text{ and } \bar{n}_e^L \approx 2 T_e D_F(T_e), \quad (\text{S41})$$

where $\text{erf}(1) \approx 0.843$, $\text{erfc}(1) = 1 - \text{erf}(1)$ and n_e is given in Eq. (S32).

Likewise, we split the distribution of holes in the LFB into two subpopulations. A subpopulation near the top of the LFB within a quasienergy window $\varepsilon \in [-\Delta_F/2 - T_h, -\Delta_F/2]$. The density of this subpopulation is given by

$$n_h^L = \int_{-\Delta_F/2 - T_h}^{-\Delta_F/2} D_F(-\varepsilon - \Delta_F/2) (1 - f_{\varepsilon-}) d\varepsilon, \quad (\text{S42})$$

and the complementary subpopulation, whose density is $n_h^H = n_h - n_h^L$. We also define the density of populated states near the top of the LFB, \bar{n}_h^L , defined by Eq. (S42) with $1 - f_{\varepsilon-}$ replaced by $f_{\varepsilon-}$. Explicitly performing the integral in Eq. (S42) on the distribution of holes [given in Eq. (S29)], we evaluate

$$n_h^L \approx \text{erf}(1) n_h, \quad n_h^H \approx \text{erfc}(1) n_h \text{ and } \bar{n}_h^L \approx 2 T_h D_F(T_h), \quad (\text{S43})$$

where n_h is given in Eq. (S33).

In what follows, we express \dot{n}_e^L and \dot{n}_h^L in terms of the incoming and outgoing rates, and find a balance between them in the steady state by requiring $\dot{n}_e^L = 0$ and $\dot{n}_h^L = 0$. We begin with the equation for \dot{n}_e^L . The subpopulations of the UFB are subjected to intraband relaxation processes transferring particles between high-

and low-quasienergy sectors within the band. Essentially, these are phonon-assisted electron-hole pair annihilation processes with the rate estimated by $\dot{n}_e^L|_{\text{relax}} = \Lambda_{\text{intra}}(T_e)n_e^H\bar{n}_e^L$ (see Fig. S3e). As we show in Sec. III F, the relaxation rate in the UFB depends on the temperature of the electrons. The incoming rate of electrons into the low-quasienergy sector is balanced by the phonon-assisted interband recombination rate, serving as a sink of electrons from this sector. The interband recombination rate is proportional to the density of electrons in the low-quasienergy sector in the UFB and density of holes in the LFB, with approximately the same coefficient Λ_{inter} , as the total interband relaxation appearing in Eq. (S35). We thus estimate the interband recombination rate by $\dot{n}_e^L|_{\text{inter}} = -\Lambda_{\text{inter}}n_e^L n_h$.

Our treatment also includes equilibration between electron and hole distributions by electron-electron scattering. Electron-electron scattering tends to equalize the temperatures of the populations in the UFB and LFB, without changing their total densities (see Fig. S3f). As the population of each of the bands is assumed to be in a local equilibrium, which is well-described by the Fermi-function, scattering of two electrons in the same band can not affect it. To account for the interband equilibration, it is convenient to define the average temperature of the UFB and LFB populations $T = (T_e + T_h)/2$ and their temperature difference, $\Delta T = T_e - T_h$.

First, assume that the electrons and holes have the same temperature ($\Delta T = 0$). In this case, the thermalization rate is zero, as the populations are already in equilibrium. Next, consider a small temperature difference of the populations, ΔT . If $\Delta T > 0$, the electron-electron scattering induces electron-hole pair annihilation in the UFB and electron-hole pair creation in the LFB, effectively cooling down the UFB and heating up the LFB. In contrast, when $\Delta T < 0$, electron-hole pairs are created in the UFB and annihilated in the LFB. When the thermalization is significant, we expect the temperatures of the two bands to be almost the same, i.e., $|\Delta T| \ll T$. Such pair creation and annihilation in the two bands occurs in a quasienergy window of width $\sim T$. Notice that in the numerical simulation (Figs. 2 and 3 in the main text), the equilibration between electron and hole distributions due to electron-electron scattering was not taken in account. We later justify this (see Sec. III H 2) by showing that this effect does not significantly affect the majority population.

Following from the above arguments, we expect the electron-electron scattering rate to be linear in ΔT to the leading order. We estimate the equilibration rate by $\dot{n}_e^L|_{\text{ee}} = \gamma_{\text{ee}}\Delta T n_e^H \bar{n}_e^L n_h^H \bar{n}_h^L$. This rate serves as a source of particles for the low-quasienergy sector in the UFB when $\Delta T > 0$, and a sink when $\Delta T < 0$. It is proportional to the densities in the UFB of occupied states (above E_s) and unoccupied states (below E_s) available for annihilation, and densities in the LFB of occupied states (above $-\Delta_F/2 - T_h$) and unoccupied states (below $-\Delta_F/2 - T_h$) available for a pair creation. A further justification for

this form will be discussed in Sec. III G, where we estimate the value of γ_{ee} in terms of the system's parameters. Combining all the terms above, we arrive at the full rate equation for n_e^L , which reads

$$\dot{n}_e^L = \Lambda_{\text{intra}}(T_e)n_e^H\bar{n}_e^L - \Lambda_{\text{inter}}n_e^L n_h + \gamma_{\text{ee}}\Delta T n_e^H\bar{n}_e^L n_h^H\bar{n}_h^L. \quad (\text{S44})$$

Our fourth equation describes thermalization and relaxation in the LFB, expressed through an equation for \dot{n}_h^L . The intraband and interband rates are estimated by $\dot{n}_h^L|_{\text{intra}} = \Lambda_{\text{intra}}(T_h)n_h^H\bar{n}_h^L$ and $\dot{n}_h^L|_{\text{inter}} = -\Lambda_{\text{inter}}n_h^L n_e$. Here we approximate Λ_{inter} and Λ_{intra} by the same coefficients as in Eq. (S44) evaluated at the hole temperature T_h , as follows from the particle-hole symmetry of the Hamiltonian. In analogy to the discussion above Eq. (S44), we estimate the electron-electron thermalization rate by $\dot{n}_h^L|_{\text{ee}} = -\gamma_{\text{ee}}\Delta T n_h^H\bar{n}_h^L n_e^H\bar{n}_e^L$. Combining all the incoming and outgoing rates we arrive at the full rate equation for n_h^L , which reads

$$\dot{n}_h^L = \Lambda_{\text{intra}}(T_h)n_h^H\bar{n}_h^L - \Lambda_{\text{inter}}n_h^L n_e - \gamma_{\text{ee}}\Delta T n_h^H\bar{n}_h^L n_e^H\bar{n}_e^L. \quad (\text{S45})$$

In order to solve Eqs. (S44) and (S45) for the chemical potentials and effective temperatures in the steady state [for total densities n_e and n_h fixed by Eq. (S38)], we first need to estimate how the densities and the coefficients appearing in these equations (such as Λ_{inter} , Λ_{intra} and γ_{ee}) depend on the parameters of the steady state. In the sections below, we perform these estimations. In Sec. III H, we extract the expressions for the chemical potentials and temperatures as a function of κ , Δn and the parameters of the system.

C. Evaluation of the rates and Floquet-Fermi's golden rule

Before we evaluate the scattering rates for the processes presented in Fig. S3, we first review the Fermi's golden rule for transitions between Floquet states^{4,5}. For brevity, we use a notation $\mathbf{k}\nu$ to indicate a state with momentum \mathbf{k} and Floquet band ν .

We first discuss the rate for scattering of an electron between states $\mathbf{k}\nu$ and $\mathbf{k}'\nu'$ due to a collision with a phonon ($p = s$) or photon ($p = \ell$) [resulting from the coupling Hamiltonian in Eq. (5) in the main text]. We assume the phonon bath is at zero temperature. The scattering rate is given by

$$(\dot{f}_{\mathbf{k}\nu})_{p,\mathbf{k}'\nu'} = 2\pi \sum_l \mathcal{P}_p^{(l)}(\mathbf{k}\nu, \mathbf{k}'\nu') \times [\rho_p(\mathbf{q}, \omega_l) F(\mathbf{k}'\nu', \mathbf{k}\nu) - \rho_p(\mathbf{q}, -\omega_l) F(\mathbf{k}\nu, \mathbf{k}'\nu')], \quad (\text{S46})$$

where $\mathcal{P}_p^{(l)}(\mathbf{k}\nu, \mathbf{k}'\nu') = |\sum_m \langle \phi_{\mathbf{k}'\nu'}^{m+l} | \mathcal{M}_p(\mathbf{q}, \omega_l) | \phi_{\mathbf{k}\nu}^m \rangle|^2$ and

$$F(\mathbf{k}\nu, \mathbf{k}'\nu') = f_{\mathbf{k}\nu} \bar{f}_{\mathbf{k}'\nu'}, \quad (\text{S47})$$

where $\bar{f} \equiv 1 - f$. The in-plane momentum and energy transfers are given by $\mathbf{q} = \mathbf{k}' - \mathbf{k}$ and $\omega_l = \varepsilon_{\mathbf{k}'\nu'} - \varepsilon_{\mathbf{k}\nu} + l\Omega$.

We consider the following electron-phonon coupling

$$\mathcal{M}_s(\mathbf{q}, \omega) = g_s |\mathbf{q}| / \sqrt{\omega} \mathbf{1}, \quad (\text{S48})$$

where $\mathbf{1}$ is the identity matrix, and consider electron-photon coupling of two polarizations,

$$\mathcal{M}_\ell^{(1)} = g_\ell \sigma^x, \quad \mathcal{M}_\ell^{(2)} = g_\ell \sigma^y. \quad (\text{S49})$$

We take the density of states of three-dimensional phonons as a function of the in-plane momentum \mathbf{q} (the in-plane momentum of the phonon is the momentum transfer of the electron), $\rho_s(\omega, \mathbf{q}) = \rho_s^0 \omega / \sqrt{\omega^2 - v_s^2 |\mathbf{q}|^2}$ when $\omega > v_s |\mathbf{q}|$ and zero otherwise. For the heat bath of phonons, we consider $\rho_\ell(\omega, \mathbf{q}) = \delta^{(2)}(\mathbf{q}) \rho_\ell^0$.

The scattering rate due to electron-electron interaction depends on occupations of four electronic states. Consider an event in which two electrons occupying states $\mathbf{k}\nu$ and $\mathbf{p}\mu$, scatter into $\mathbf{k}'\nu'$ and $\mathbf{p}'\mu'$. The net rate of such an event and its reversed process reads

$$(\dot{f}_{\mathbf{k}\nu})_{ee} = 2\pi \sum_l \mathcal{P}_{ee}^{(l)}(\mathbf{k}\nu, \mathbf{p}\mu; \mathbf{k}'\nu', \mathbf{p}'\mu') \times F_{ee}(\mathbf{k}\nu, \mathbf{p}\mu; \mathbf{k}'\nu', \mathbf{p}'\mu') \delta(\Delta\varepsilon_1 + \Delta\varepsilon_2 + l\Omega), \quad (\text{S50})$$

where $\mathcal{P}_{ee}^{(l)} = |\sum_{jmn} \langle \phi_{\mathbf{k}\nu}^{l-j+m} | \phi_{\mathbf{p}\mu}^{j+n} | \hat{\mathcal{H}}_{\text{int}} | \phi_{\mathbf{k}'\nu'}^m | \phi_{\mathbf{p}'\mu'}^n \rangle|^2$,

$$F_{ee} = f_{\mathbf{k}'\nu'} \bar{f}_{\mathbf{p}'\mu'} \bar{f}_{\mathbf{p}\mu} - f_{\mathbf{k}\nu} \bar{f}_{\mathbf{k}'\nu'} f_{\mathbf{p}\mu} \bar{f}_{\mathbf{p}'\mu'}, \quad (\text{S51})$$

and $\Delta\varepsilon_1 = \varepsilon_{\mathbf{k}'\nu'} - \varepsilon_{\mathbf{k}\nu}$, $\Delta\varepsilon_2 = \varepsilon_{\mathbf{p}'\mu'} - \varepsilon_{\mathbf{p}\mu}$. Throughout, we consider contact interactions, $\hat{\mathcal{H}}_{\text{int}} = \sum_{\mathbf{k}_1 \mathbf{k}_2 \mathbf{k}_3} (U/a^2) \hat{c}_{\mathbf{k}_1 + \mathbf{k}_3 \uparrow}^\dagger \hat{c}_{\mathbf{k}_1 \uparrow} \hat{c}_{\mathbf{k}_2 - \mathbf{k}_3 \downarrow}^\dagger \hat{c}_{\mathbf{k}_2 \downarrow}$, where $\hat{c}_{\mathbf{k}\uparrow(\downarrow)}$ creates an electron of momentum \mathbf{k} and pseudospin $\uparrow(\downarrow)$ [see discussion below Eq. (1) in the main text]. Using the above form of $\hat{\mathcal{H}}_{\text{int}}$, the expression for the squared matrix element can be written as

$$\mathcal{P}_{ee}^{(l)} = \frac{U^2}{4a^4} \left| \sum_{jmn} \langle \phi_{\mathbf{k}\nu}^{l-j+m} | \phi_{\mathbf{k}'\nu'}^m \rangle \langle \phi_{\mathbf{p}\mu}^{j+n} | \phi_{\mathbf{p}'\mu'}^n \rangle - \sum_{\alpha=x,y,z} \langle \phi_{\mathbf{k}\nu}^{l-j+m} | \sigma^\alpha | \phi_{\mathbf{k}'\nu'}^m \rangle \langle \phi_{\mathbf{p}\mu}^{j+n} | \sigma^\alpha | \phi_{\mathbf{p}'\mu'}^n \rangle \right|^2, \quad (\text{S52})$$

when $\mathbf{k} + \mathbf{p} = \mathbf{k}' + \mathbf{p}'$ and $\mathcal{P}_{ee}^{(l)} = 0$ otherwise. Here σ^α is a Pauli matrix in the pseudospin basis. Clearly, the RHS of Eq. (S52) vanishes when the two colliding electrons have parallel pseudospins, and is maximal when the pseudospins are antiparallel. This property directly follows from the contact interactions between the electrons and the Pauli principle. Once we established the Floquet-Fermi's golden rule formalism, we are in the position to evaluate the heating, cooling and thermalization rates.

D. Heating rates

We begin our discussion with heating processes, transferring electrons from the LFB to UFB. For zero-temperature heat baths, energy required for the excitations is provided by the Floquet-Umklapp mechanism,

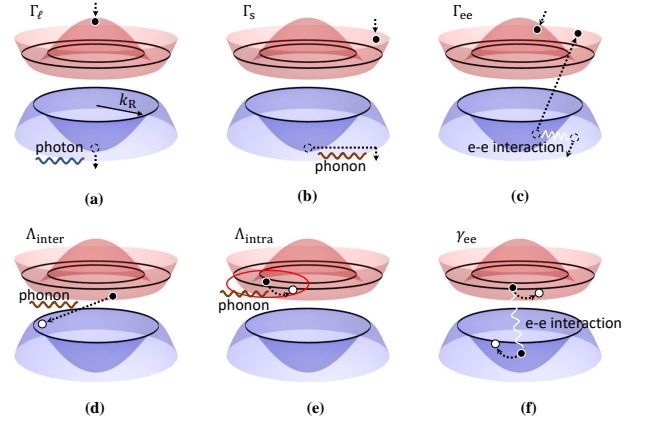


FIG. S3. Key processes contributing to the steady-state distribution in the nearly symmetric case, $U \lesssim U_c$. We consider here an EFM phase for the electrons in the UFB, associated with two concentric Fermi surfaces (represented by a double black ring), and a non-degenerate distribution of holes in the LFB, with a maximum of the distribution shown by a single black ring. The heating processes are summarized in panels (a), (b), and (c); Panels (d), (e), and (f) demonstrate cooling and thermalization processes. (a). Photon-mediated excitation processes, dominant inside the resonance ring, with approximately zero-momentum transfer. (b). Phonon-mediated excitations, predominantly transferring electrons between states inside and outside the resonance ring. (c). Floquet-Auger heating, corresponding to a transition of two electrons occupying the interior and exterior of the resonance ring, to states outside and inside the resonance ring, respectively (see Fig. S4). (d). Phonon-assisted interband recombination of electrons occupying the Fermi sea in the UFB and holes in the LFB. Assuming a large Floquet gap ($\Delta_F \gg 2k_R v_s$) the phonon density of states supports scattering between states in the UFB and LFB of any two points close to the resonance ring. (e). Phonon-assisted intraband relaxation. In the low-temperature limit, $T < 2k_R v_s$, the phonon density of states only allows for small-momentum transitions with a momentum transfer below $\sim T/v_s$. Therefore, the allowed states to scatter into are within a circle of radius $\sim T/v_s$ centered around the initial electron position (indicated by the red circle) (f). Intraband thermalization by electron-electron interactions. The main role of these processes is equilibration of temperatures of the electron and hole distributions. The total density of particles in each of the bands after the collision is preserved.

dominated by $l = 1$ terms in Eqs. (S46) and (S50). In the estimation of heating rates we will approximate $f_{\mathbf{k}-} \approx 1$ and $f_{\mathbf{k}+} \approx 0$, which is exact in the limit $\kappa \rightarrow 0$. As the majority of excitation processes occur away from the resonance ring, we simplify the analysis by taking the limit $V/\Omega \rightarrow 0$. In this limit, the Floquet wavefunctions are not analytic at $|\mathbf{k}| = k_R$, yet obtain a simple structure away from the resonance ring. The zeroth order in (V/Ω) reads

$$|\phi_{\mathbf{k}\pm}(t)\rangle = e^{\frac{i\Omega t}{2}} \begin{cases} |\Psi_{\mathbf{k}\mp}\rangle e^{\pm \frac{i\Omega t}{2}}, & |\mathbf{k}| < k_R \\ |\Psi_{\mathbf{k}\pm}\rangle e^{\mp \frac{i\Omega t}{2}}, & |\mathbf{k}| > k_R \end{cases}, \quad (\text{S53})$$

where $|\Psi_{\mathbf{k}\pm}\rangle$ are the eigenstates of $H_0(\mathbf{k})$ [see Eq. (S1)], given by

$$|\Psi_{\mathbf{k}\pm}\rangle = \frac{1}{\sqrt{2}} \left(\sqrt{1 \pm \hat{\mathbf{z}} \cdot \hat{\mathbf{d}}(\mathbf{k})} |\uparrow\rangle \mp e^{i\theta_{\mathbf{k}}} \sqrt{1 \mp \hat{\mathbf{z}} \cdot \hat{\mathbf{d}}(\mathbf{k})} |\downarrow\rangle \right). \quad (\text{S54})$$

To determine the power of V/Ω multiplying the scattering rates for the higher order terms, we use a method described in Fig. S2c. Note, that these approximate expressions of the wavefunctions can not be used to analyze the distributions near the Floquet gap. Therefore, we use a different approximation when we discuss relaxation and thermalization processes in Secs. III E-III G.

1. Photon-assisted excitation rate

We begin with the photon-assisted interband excitations. These are vertical Floquet-Umklapp processes [the initial and final momentum of the photons are identical, see the definition of the photon density of states below Eq. (S49)], predominantly transferring electrons inside the resonance ring. Processes outside the ring can be neglected in the limit $V/\Omega \rightarrow 0$, as they are suppressed by a factor of $\sim (V/\Omega)^4$ (see Fig. S2c for an explanation). In what follows, we estimate the dominant contribution, illustrated in Fig. S3a.

We define the rate of change (ROC) of the density in the UFB as $\dot{n}_{e|\text{photon}} = \Gamma_{\ell}$, where

$$\Gamma_{\ell} = \int \frac{a^2 d^2 \mathbf{k} d^2 \mathbf{k}'}{(2\pi)^4} (\dot{f}_{\mathbf{k}+})_{\ell, \mathbf{k}'-}. \quad (\text{S55})$$

We approximate $(\dot{f}_{\mathbf{k}+})_{\ell, \mathbf{k}'-}$ [given in Eq. (S46)] by $(\dot{f}_{\mathbf{k}+})_{\ell, \mathbf{k}'-} \approx 2\pi \mathcal{P}_{\ell}^{(1)}(\mathbf{k}+, \mathbf{k}-) \rho_{\ell}^0 \delta(\mathbf{k} - \mathbf{k}')$, when $|\mathbf{k}| < k_{\text{R}}$ and zero otherwise. The sum of squared matrix elements for two photon polarizations [Eq. (S49)] evaluated in the states $|\Psi_{\mathbf{k}\nu}\rangle$ [Eq. (S53)] inside the resonance ring ($|\mathbf{k}| < k_{\text{R}}$) is given by $\mathcal{P}_{\ell}^{(1)}(\mathbf{k}+, \mathbf{k}-) = \sum_{i=1,2} |\langle \Psi_{\mathbf{k}-} | \mathcal{M}_{\ell}^{(i)} | \Psi_{\mathbf{k}+} \rangle|^2 = g_{\ell}^2 (1 + \hat{\mathbf{z}} \cdot \hat{\mathbf{d}}(\mathbf{k}))$. We further approximate $\hat{\mathbf{z}} \cdot \hat{\mathbf{d}} \approx 1$ to leading order in $\lambda_0 k_{\text{R}}/E_{\text{g}}$, yielding $\mathcal{P}_{\ell}^{(1)} \approx 2g_{\ell}^2$ and perform the trivial momentum integral in Eq. (S55) to arrive at

$$\Gamma_{\ell} = g_{\ell}^2 \rho_{\ell}^0 \mathcal{A}_{\text{R}} a^2 / (4\pi^3). \quad (\text{S56})$$

Recall that $\mathcal{A}_{\text{R}} = \pi k_{\text{R}}^2$ is the area in the reciprocal space enclosed by the resonance ring.

2. Phonon-assisted excitation rate

Next, we estimate the phonon-assisted excitation rate (for an illustration see Fig. S3b). The ROC of the density in the UFB due to phonon-assisted excitation, $\dot{n}_{e|\text{phonon}} = \Gamma_{\text{s}}$, reads

$$\Gamma_{\text{s}} = \int \frac{a^2 d^2 \mathbf{k} d^2 \mathbf{k}'}{(2\pi)^4} (\dot{f}_{\mathbf{k}+})_{\text{s}, \mathbf{k}'-}, \quad (\text{S57})$$

where we use the approximate expression

$$(\dot{f}_{\mathbf{k}+})_{\text{s}, \mathbf{k}'-} \approx 2\pi \mathcal{P}_{\text{s}}^{(1)}(\mathbf{k}+, \mathbf{k}'-) \rho_{\text{s}}(\mathbf{k} - \mathbf{k}', \omega), \quad (\text{S58})$$

and $\omega = \varepsilon_{\mathbf{k}'-} - \varepsilon_{\mathbf{k}+} + \Omega$, see Eq. (S46). We evaluate the expectation value in $\mathcal{P}_{\text{s}}^{(1)}$ [defined below Eq. (S46)] using the electron-phonon coupling [Eq. (S48)] and the Floquet states given in Eq. (S53). The result splits to four different rates, depending whether the momenta \mathbf{k} and \mathbf{k}' are inside or outside the resonance ring.

First, consider transitions where both momenta \mathbf{k} and \mathbf{k}' are inside the resonance ring. The rate of such transitions is suppressed by $\sim (\lambda_0 k_{\text{R}}/E_{\text{g}})^2$ as the electron-phonon coupling [which we assume has a diagonal form in the pseudospin basis, see Eq. (S48)] connects almost orthogonal pseudospin states. Furthermore, transitions inside the resonance ring are unfavorable as the electron-phonon coupling favours short-wavelength phonons, while the wavelength corresponding to the momentum transfer inside the resonance ring is at least $\sim (2k_{\text{R}})^{-1}$. Therefore, in what follows we neglect transitions where both momenta are inside the resonance ring.

Next, we consider transitions for which \mathbf{k}' is inside and \mathbf{k} is outside the resonance ring (or otherwise, \mathbf{k}' outside and \mathbf{k} inside the resonance ring). These processes require an absorption of a drive-photon leading to suppression of their rate by a factor of $(V/\Omega)^2$ [see Fig. S2c for explanation]. Assuming a narrow-band semiconductor (analogous to the assumption in our numerical analysis, see Tab. S1) we approximate the energy transfer, appearing in the definition of $\mathcal{P}_{\text{s}}^{(1)}$ and ρ_{s} in Eq. (S58), by $\omega \sim \Omega$, leading to $\mathcal{P}_{\text{s}}^{(1)}(\mathbf{k}+, \mathbf{k}'-) \approx \frac{g_{\text{s}}^2 |\mathbf{k} - \mathbf{k}'|^2}{\Omega} \left(\frac{V}{\Omega}\right)^2$ [cf. Eq. (S48)] and $\rho_{\text{s}}(\mathbf{q}, \Omega) \approx \rho_{\text{s}}^0$. Explicitly integrating over $(\dot{f}_{\mathbf{k}+})_{\text{s}, \mathbf{k}'-}$ in Eq. (S57), we arrive at

$$\Gamma_{\text{s}} \approx \frac{g_{\text{s}}^2 \rho_{\text{s}}^0 a^2 \mathcal{A}_{\text{R}} \Lambda^4}{8\pi^2 \Omega} \left(\frac{V}{\Omega}\right)^2, \quad (\text{S59})$$

where $\Lambda \sim \pi/a$ is the large momentum cutoff for phonon transitions. Note that the processes considered here, involve collisions with large-energy phonons (of energy $\sim \Omega$). Such phonons might not be supported in materials in which the Debye frequency is smaller than Ω .

An alternative scenario, which describes many periodically driven semiconductor systems, is the case of a large electronic bandwidth compared to the drive frequency. In this case, the bandstructure supports transitions transferring electrons between momentum states inside and outside the resonance ring (similar to the scenario discussed above), assisted by low-energy phonons. In particular, the allowed energy of the phonon is within the range $\omega \in [\omega_0, \omega_{\text{D}}]$, where ω_{D} is the Debye energy of the semiconductor and ω_0 is the minimal energy allowed by the kinematic constraints. For simplicity, we assume the parabolic dispersion near the Γ -point (with an effective mass m_*) extends to energies $\gtrsim \Omega$. We also assume the limit $k_{\text{R}}/\sqrt{2m_*\Omega} \rightarrow 0$. In this limit, the momentum transfer $|\mathbf{q}| = |\mathbf{k} - \mathbf{k}'|$, approximately equals the momentum of the electron after the transition, $|\mathbf{k}|$. It follows

from the above, the minimal allowed phonon energy ω_0 is given by $\omega_0 = v_s|\mathbf{q}_0|$, where $|\mathbf{q}_0| = \sqrt{2m_*(\Omega - \omega_0)}$ is the maximal allowed momentum transfer in the process.

To evaluate $\mathcal{P}_s^{(1)}(\mathbf{k}+, \mathbf{k}'-)$ and the density of states, ρ_s [appearing in Eq. (S58)], we estimate the energy transfer by $\omega \approx \Omega - \varepsilon_{\mathbf{k}+}$. Recall that \mathbf{k} denotes momentum far from the resonance ring, where the dispersion is approximately parabolic, $\varepsilon_{\mathbf{k}+} \approx |\mathbf{k}|^2/(2m_*)$. Therefore, we approximate $\mathcal{P}_s^{(1)}(\mathbf{k}+, \mathbf{k}'-) \approx \frac{g_s^2|\mathbf{k}|^2}{\Omega - \varepsilon_{\mathbf{k}+}} \left(\frac{V}{\Omega}\right)^2$ and $\rho_s \approx \frac{\rho_s^0(\Omega - \varepsilon_{\mathbf{k}+})}{\sqrt{(\Omega - \varepsilon_{\mathbf{k}+})^2 - v_s^2|\mathbf{k}|^2}}$.

We are now ready to evaluate the integral in Eq. (S57). The \mathbf{k}' -integral is in the domain $|\mathbf{k}'| < k_R$. The integral over \mathbf{k} is performed in the range $|\mathbf{k}| \in [|\mathbf{q}_D|, |\mathbf{q}_0|]$, where \mathbf{q}_D is found from $\omega_D = \Omega - \varepsilon_{\mathbf{q}_D+}$ (leading to $|\mathbf{q}_D| = \sqrt{2m_*(\Omega - \omega_D)}$.) Transforming to polar coordinates where $k = |\mathbf{k}|$ and $k' = |\mathbf{k}'|$, we obtain $\Gamma_s = \frac{g_s^2\rho_s^0a^2}{\pi} \left(\frac{V}{\Omega}\right)^2 \int_0^{k_R} dk' k' \int_{|\mathbf{q}_D|}^{|\mathbf{q}_0|} dk k^3 / \sqrt{(\Omega - \varepsilon_{\mathbf{k}+})^2 - v_s^2k^2}$. Explicitly integrating over k and k' in the limit $\Omega \gg \omega_D \gg m_*v_s^2$, we arrive at

$$\Gamma_s \approx \frac{2c_D g_s^2 \rho_s^0 a^2 \mathcal{A}_R m_*^2 \Omega}{\pi^2} \left(\frac{V}{\Omega}\right)^2, \quad (\text{S60})$$

where $c_D = \log\left(\frac{\sqrt{2m_*v_s^2\Omega}}{\omega_D - \sqrt{\omega_D^2 - 2m_*v_s^2\Omega}}\right)$.

Finally, consider processes where both \mathbf{k} and \mathbf{k}' are outside the resonance ring. These processes are suppressed by $(V/\Omega)^4$ as they require absorption of two virtual photons [see Fig. S2c]. Furthermore, they will be suppressed by $\sim (2m_*\lambda_0/\Lambda)^2$ as such transitions connect almost orthogonal pseudospin states. We thus neglect the contribution of these processes to the phonon-assisted excitation rate.

3. Floquet-Auger excitation rate

Here, we estimate the rate of transfer of electrons from the LFB to the UFB due to electron-electron scattering. The main processes contributing to such transfer are electron-pair excitations from the LFB to UFB⁶. For the estimation of this rate, we assume a state with a full LFB and empty UFB (we therefore neglect processes which result in net transfer of electrons from the UFB to the LFB). The leading processes resulting in a transfer of two electrons from the LFB to the UFB involve a change of the total quasienergy by Ω via the Floquet-Umklapp mechanism (illustrated in Fig. S3c). The ROC of the density due to these processes is given by $\dot{n}_e|_{ee} = \Gamma_{ee}$, where

$$\Gamma_{ee} = 2 \int \frac{a^4 d^2\mathbf{k} d^2\mathbf{p} d^2\mathbf{q}}{(2\pi)^6} (\dot{j}_{\mathbf{k}+})_{ee}. \quad (\text{S61})$$

Here \mathbf{k} and \mathbf{p} are the momenta of the final states in the UFB and $\mathbf{k}' = \mathbf{k} + \mathbf{q}$, $\mathbf{p}' = \mathbf{p} - \mathbf{q}$ denote

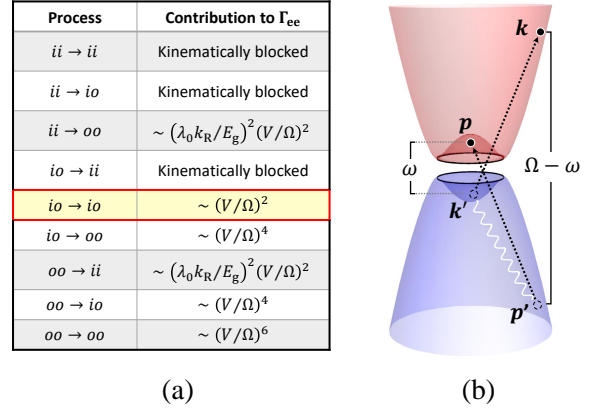


FIG. S4. Floquet-Auger excitation rate. (a). A summary of possible scattering processes and their estimated contribution to Γ_{ee} , divided to cases. The first column shows the possible types of processes; i and o indicate momenta inside and outside the resonance ring. The first two letters correspond to initial momenta of the two electrons (in the LFB) and the last two letters correspond to momenta after the collision (in the UFB). The second column shows the estimated weight of each process in terms of powers of (V/Ω) . We denote by “kinematically-blocked”, processes that can not satisfy the energy and momentum conservation conditions due to the bandstructure constraints. (b). Schematic illustration of the dominant collision, $io \rightarrow io$, highlighted in panel (a). The momenta \mathbf{k}' and \mathbf{p}' denote the states of two electrons in the LFB before the collision, and the momenta \mathbf{k} and \mathbf{p} denotes the states in the UFB after the collision. The energy differences, ω and $\Omega - \omega$ are defined as $\omega = \varepsilon_{\mathbf{p}+} - \varepsilon_{\mathbf{k}'-}$ and $\Omega - \omega = \varepsilon_{\mathbf{k}+} - \varepsilon_{\mathbf{p}'-}$.

the initial momenta in the LFB; the factor 2 accounts for a pair of electrons excited in each collision. We estimate $(\dot{j}_{\mathbf{k}+})_{ee}$, given in Eq. (S50), by $(\dot{j}_{\mathbf{k}+})_{ee} \approx 2\pi \mathcal{P}_{ee}^{(1)}(\mathbf{k}+, \mathbf{p}+, \mathbf{k}'-, \mathbf{p}'-) \delta(\Delta\varepsilon_1 + \Delta\varepsilon_2 + \Omega)$ [see definitions of $\Delta\varepsilon_{1,2}$ below Eq. (S50)], and evaluate $\mathcal{P}_{ee}^{(1)}$ using Eq. (S52) and the approximate Floquet wavefunctions given in Eq. (S53). As the approximate wavefunctions are non-analytic at $|\mathbf{k}| = k_R$, we divide the analysis of the scattering rate to 9 distinct cases. In each case, the momenta \mathbf{k} , \mathbf{k}' , \mathbf{p} and \mathbf{p}' are either inside or outside the resonance ring.

Fig. S4a shows a table of all possible cases and their estimated contribution to Γ_{ee} . We consider the limit $\delta E \ll \Omega$ which kinematically constraints some of the processes. For example, processes where the two initial and the two final momenta are inside the resonance ring (corresponding to $ii \rightarrow ii$ in Fig. S4a) are kinematically blocked, as there is no such process for which the total energy change (which is limited by $2\delta E$ by the Floquet bandstructure) can be equal Ω . Processes corresponding to $ii \rightarrow oo$ and $oo \rightarrow ii$ involve scattering of two electrons starting and ending in the same band in terms of the undriven band structure, cf. Eq. (S53). These processes

are Pauli-suppressed by a factor of $\sim (\lambda_0 k_{\text{R}}/E_{\text{g}})^2$ as the pseudospins of the electrons involved in the collision are almost parallel, see discussion following Eq. (S52).

The most significant contribution to the rate [proportional to $(V/\Omega)^2$] corresponds to transitions of two electrons initially occupying one state inside the resonance ring and one state outside of it, scattered into two states in the UFB where one is inside and one is outside the resonance ring (denoted by $io \rightarrow io$ in Fig. S4a). An illustration of such a process is shown in Fig. S4b. We choose the momenta \mathbf{k}' and \mathbf{p} inside the resonance ring and \mathbf{p}' and \mathbf{k} outside the resonance ring. To account for processes where $(\mathbf{k}', \mathbf{p})$ and $(\mathbf{p}', \mathbf{k})$ are exchanged, we multiply the rate by 2. We consider the process for which $\Delta\varepsilon_1 = \varepsilon_{\mathbf{k}'-} - \varepsilon_{\mathbf{k}+} < 0$, and $\Delta\varepsilon_2 = \varepsilon_{\mathbf{p}'-} - \varepsilon_{\mathbf{p}+} > 0$. The amplitude of such a process is suppressed by a factor of $(V/\Omega)^2$, see Fig. S2c. We also assume that the amplitude of the process where $\Delta\varepsilon_1 > 0$, and $\Delta\varepsilon_2 < 0$ constructively interfere with the previous case such that the matrix element for both processes is twice the matrix element of each one of them. Following from the above, we approximate $\mathcal{P}_{\text{ee}}^{(1)} \approx 2(2UV/a^2\Omega)^2$. Notice that there is an additional scenario included in $io \rightarrow io$ processes, corresponding to $|\mathbf{k}|, |\mathbf{k}'| < k_{\text{R}}$ and $|\mathbf{p}|, |\mathbf{p}'| > k_{\text{R}}$. This scenario gives much smaller contribution to the rate since it includes transitions between almost orthogonal pseudospin states. We thus neglect it in our analysis.

To evaluate the integral in Eq. (S61) we introduce a new variable, ω , which splits the energy-conservation δ -function as follows, $\delta(\Delta\varepsilon_1 + \Delta\varepsilon_2 + \Omega) = \int d\omega \delta(\Delta\varepsilon_3 + \omega) \delta(\Delta\varepsilon_4 + \Omega - \omega)$. Here, we defined $\Delta\varepsilon_3 \equiv \varepsilon_{\mathbf{k}'-} - \varepsilon_{\mathbf{p}+}$ and $\Delta\varepsilon_4 \equiv \varepsilon_{\mathbf{p}'-} - \varepsilon_{\mathbf{k}+}$, such that $\Delta\varepsilon_1 + \Delta\varepsilon_2 = \Delta\varepsilon_3 + \Delta\varepsilon_4$. Therefore, ω denotes the energy transfer inside the resonance ring and $\Omega - \omega$ the energy transfer outside the resonance ring (see Fig. S4b). It is also useful to define the momentum transfer inside the resonance ring, $\mathbf{q}' = \mathbf{p} - \mathbf{k}'$. By conservation of the total momentum, it equals the momentum transfer outside the resonance ring, $\mathbf{q}' = \mathbf{p}' - \mathbf{k}$. The bandstructure near the Γ -point restricts the values of ω and $|\mathbf{q}'|$ to $\omega < \delta E$ and $|\mathbf{q}'| < 2k_{\text{R}}$. Therefore, given the constraint $-\Delta\varepsilon_4 = \Omega - \omega$, we can approximate $\Delta\varepsilon_4 \approx 2\varepsilon_{\mathbf{p}'-} \approx -2\varepsilon_{\mathbf{k}+}$, since $\delta E \ll \Omega$.

We use the last approximation to replace $\Delta\varepsilon_4$ by $-2\varepsilon_{\mathbf{k}+}$ in the energy-conservation δ -function in Eq. (S61), and integrate over \mathbf{k} , yielding $\int d^2\mathbf{k} \delta(\Delta\varepsilon_4 + \Omega - \omega) \approx \pi m_*$. Remarkably, due to the nearly parabolic dispersion outside the resonance ring with a density of states which is constant as a function of energy, the result of the \mathbf{k} -integral is independent of $\Omega - \omega$. Next, we perform the ω -integral over $\delta(\Delta\varepsilon_3 + \omega)$, yielding 1. Finally, we perform the trivial \mathbf{p} and \mathbf{k}' -integrals over a constant function remained from the previous integrals, yielding a factor of \mathcal{A}_{R} for each of the variables. Collecting all the factors, we arrive at

$$\Gamma_{\text{ee}} \approx \frac{\mathcal{A}_{\text{R}}^2 U^2 m_*}{2\pi^4} \left(\frac{V}{\Omega}\right)^2. \quad (\text{S62})$$

E. Phonon-assisted interband recombination rate

Here, we discuss phonon-assisted interband relaxation processes. Interband relaxation serves as a sink mechanism for the excitations created by the heating processes (described in Sec. III D). Electrons transferred to the UFB by the heating processes first undergo fast intra-band relaxation followed by multiple-phonon emission, transferring electrons to the bottom of the UFB. Then, they recombine with the holes in the LFB, which were, in turn, transferred to the top of the UFB by similar processes. Here we focus on such interband electron-hole recombination processes predominantly mediated by phonons (see Fig. S3d). We approximate the states involved in the scattering by the RWA states at the resonance ring, see Eq. (S10).

We expect the ROC of the density due to interband-recombination to be proportional to the densities of the electrons and holes in the UFB and LFB respectively. We thus define $\dot{n}_{\text{e}}|_{\text{inter}} = -\Lambda_{\text{inter}} n_{\text{e}} n_{\text{h}}$, where

$$\Lambda_{\text{inter}} = -\frac{1}{n_{\text{e}} n_{\text{h}}} \int \frac{a^2 d^2\mathbf{k} d^2\mathbf{k}'}{(2\pi)^4} (\dot{f}_{\mathbf{k}+})_{\text{s}, \mathbf{k}'-}. \quad (\text{S63})$$

Here $(\dot{f}_{\mathbf{k}+})_{\text{s}, \mathbf{k}'-}$ is given by Eq. (S46) where we take only the $l = 0$ term and estimate the energy transfer by $\sim \Delta_{\text{F}}$, leading to

$$(\dot{f}_{\mathbf{k}+})_{\text{s}, \mathbf{k}'-} \approx -2\pi \mathcal{P}_{\text{s}}^{(0)}(\mathbf{k}+, \mathbf{k}'-) \rho_{\text{s}}(\mathbf{q}, \Delta_{\text{F}}) F(\mathbf{k}+, \mathbf{k}'-). \quad (\text{S64})$$

The function $F(\mathbf{k}+, \mathbf{k}'-)$ is non zero only when $|\mathbf{k}|, |\mathbf{k}'| \approx k_{\text{R}}$. Therefore, we estimate $|\mathbf{q}| = |\mathbf{k}' - \mathbf{k}| \approx 2k_{\text{R}} |\sin(\Delta\theta/2)|$, where $\Delta\theta = \theta - \theta'$, and θ, θ' are the angles of the vectors \mathbf{k} and \mathbf{k}' with respect to the \hat{x} axis. We evaluate $\mathcal{P}_{\text{s}}^{(0)}$ by the matrix elements of the electron-phonon coupling [Eq. (S48)] estimated at $\omega = \Delta_{\text{F}}$ with Floquet states given in Eq. (S10), leading to $\mathcal{P}_{\text{s}}^{(0)} \approx (4g_{\text{s}}^2 k_{\text{R}}^2 / \Delta_{\text{F}}) \sin^4(\Delta\theta/2)$. In the analysis we consider the limit, $\Delta_{\text{F}} \gg 2v_{\text{s}} k_{\text{R}}$, which allows us to treat the density of states of the phonons as constant, $\rho_{\text{s}}(\mathbf{q}, \Delta_{\text{F}}) \approx \rho_{\text{s}}^0$.

Now, we turn to the evaluation of the integral in Eq. (S63). The approximate form of $(\dot{f}_{\mathbf{k}+})_{\text{s}, \mathbf{k}'-}$, discussed in Eq. (S64) and further approximations below it, lead to a separation of the integrand into a product of radial and angular terms of \mathbf{k} and \mathbf{k}' . We thus transform $d^2\mathbf{k} \rightarrow d\theta k dk$ and $d^2\mathbf{k}' \rightarrow d\theta' k' dk'$. We first integrate over the radial components, which only appear in $F(\mathbf{k}+, \mathbf{k}'-)$, leading to $\frac{1}{(2\pi)^2} \int k dk k' dk' F(\mathbf{k}+, \mathbf{k}'-) = n_{\text{e}} n_{\text{h}}$. Then we integrate over the rest of the components, which have only angular dependencies, proportional to $\sin^4(\Delta\theta/2)$. We thus arrive at the following expression,

$$\Lambda_{\text{inter}} \approx \frac{3\pi g_{\text{s}}^2 \rho_{\text{s}}^0 a^2 k_{\text{R}}^2}{\Delta_{\text{F}}}. \quad (\text{S65})$$

F. Phonon-assisted intraband relaxation rate

Next, we estimate the phonon-assisted intraband relaxation rate. Phonon-assisted intraband relaxation is the dominant mechanism for reducing the effective temperature of the excitations created by heating processes (described in Sec. III D) within each of the bands. Namely, it transfers electrons in the UFB to the bottom of the band and holes in the LFB to the top of the band. To account for the relaxation rate, we divide the population of electrons into two subsets occupying high and low-quasienergy states of electron densities n_e^H and n_e^L , respectively [cf. Eqs. (S39) and (S42)]. For concreteness, in what follows we consider an EFM phase, associated with a sharp Fermi surface for the distribution of the electrons (the analysis in the EFI phase is similar). In this case, the separation between high- and low-quasienergy subsets for the distribution of the electrons is at the effective chemical potential measured relative to the UFB bottom, μ_e [see an extended discussion in Sec. III B and Fig. S2a for an illustration].

For the EFM phase, intraband relaxation in the UFB is essentially electron-hole pair annihilation across the effective chemical potential with the rate $\dot{n}_e^L|_{\text{intra}} = \Lambda_{\text{intra}} n_e^H \bar{n}_e^L$, where \bar{n}_e^L is the density of unoccupied states in the low-quasienergy subset. The rate Λ_{intra} is given by

$$\Lambda_{\text{intra}} = \frac{1}{n_e^H \bar{n}_e^L} \int \frac{a^2 d^2 \mathbf{k} d^2 \mathbf{k}'}{(2\pi)^4} (\dot{j}_{\mathbf{k}+})_{s, \mathbf{k}'+}, \quad (\text{S66})$$

where the range of \mathbf{k}' -integral is all the states in the high-energy sector, corresponding to $\varepsilon_{\mathbf{k}'+} > \Delta_F/2 + \mu_e$. Subsequently, the range of \mathbf{k} -integral is all the states in the low-quasienergy sector, $\Delta_F/2 < \varepsilon_{\mathbf{k}+} < \Delta_F/2 + \mu_e$. We estimate $(\dot{j}_{\mathbf{k}+})_{s, \mathbf{k}'+}$ [given in Eq. (S46)] by the $l = 0$ term, thus this is not a Floquet-Umklapp process. The typical energy transfer in these processes equals the effective temperature of the electrons $\sim T_e$. Therefore, we approximate

$$(\dot{j}_{\mathbf{k}+}) \approx 2\pi \mathcal{P}_s^{(0)}(\mathbf{k}+, \mathbf{k}'+) \rho_s(\mathbf{q}, T_e) F(\mathbf{k}+, \mathbf{k}'+). \quad (\text{S67})$$

Since both of the momenta involved are close to the band minimum at $|\mathbf{k}|, |\mathbf{k}'| = k_R$, the momentum transfer is given by $|\mathbf{q}| \approx 2k_R |\sin(\Delta\theta/2)|$, where $\Delta\theta$ is the angle between the vectors \mathbf{k} and \mathbf{k}' . For low temperatures $T_e \ll v_s k_R$, the density of states $\rho_s(\mathbf{q}, T_e)$, restricts the momentum transfers within a small circle in the momentum space, $|\mathbf{q}| < T_e/v_s$, illustrated by a red circle in Fig. S3e. To further simplify the expression in Eq. (S67), we use the paraxial approximation of small angles, $|\mathbf{q}| \approx k_R \Delta\theta$. We estimate $\mathcal{P}_s^{(0)}$ by the matrix elements of the electron-phonon coupling [Eq. (S48)] estimated at $\omega = T_e$, using the Floquet states given in Eq. (S10). The above approximations result in $\mathcal{P}_s^{(0)} \approx g_s^2 k_R^2 \Delta\theta^2 / T_e$, and $\rho_s(\mathbf{q}, T_e) \approx \rho_s^0 T_e / \sqrt{T_e^2 - (v_s k_R \Delta\theta)^2}$, where $|\Delta\theta| < \theta_s$; $\theta_s = T_e / (k_R v_s)$.

Now, we are ready to evaluate the integral in Eq. (S66); we will use polar coordinates. The integrand splits to a product of terms dependent on the radial and angular components of the momentum. The integral over the radial part yields $\frac{1}{(2\pi)^2} \int k dk k' dk' F(\mathbf{k}+, \mathbf{k}'+) = n_e^H \bar{n}_e^L$. In turn, the angular part yields $\int_{-\theta_s}^{\theta_s} d\Delta\theta \Delta\theta^2 / \sqrt{1 - (\Delta\theta/\theta_s)^2} = \pi \theta_s^3 / 2$. Combining the above results of the angular and radial integrals, we arrive at

$$\Lambda_{\text{intra}} \approx \frac{\pi g_s^2 \rho_s^0 a^2 T_e^2}{2k_R v_s^3}. \quad (\text{S68})$$

A similar analysis for the EFI phase yields the same estimate [Eq. (S68)]. Subsequently, an analysis for holes gives the same result upon a replacement $T_e \rightarrow T_h$ (due to the particle-hole symmetry of the Floquet bands).

G. Equilibration of the electron and hole distributions via electron-electron scattering

Here we estimate the rate of intraband thermalization processes induced by electron-electron scattering (depicted in Fig. S3f). We consider scattering processes in which one of the incoming electrons is in the UFB, and one in the LFB, and likewise for the outgoing electrons. Thus, no interband particle transfer is involved. These processes tend to equalize the temperatures of the electron and hole populations as a result of the collisions between them. We do not consider intraband scattering, where both electrons are in the UFB or LFB, as such processes do not contribute if the distribution within the band can be described by a Fermi function (i.e., in a phase-space-local equilibrium). For simplicity, we consider a situation where the electron and hole populations in the two bands have close temperatures, such that the difference between the temperatures, $\Delta T = T_e - T_h$, is much smaller than the mean temperature, $T = (T_e + T_h)/2$, $|\Delta T| \ll T$.

We define the thermalization rate by $\dot{n}_e^L|_{\text{ee}} = \gamma_{\text{ee}} \Delta T n_e^H \bar{n}_e^L n_h^H \bar{n}_h^L$, see the discussion above Eq. (S44), where

$$\gamma_{\text{ee}} = \frac{\int a^4 d^2 \mathbf{k} d^2 \mathbf{k}' d^2 \mathbf{p} d^2 \mathbf{p}' (\dot{j}_{\mathbf{k}+})_{\text{ee}} \delta^{(2)}(\mathbf{k} + \mathbf{p} - \mathbf{k}' - \mathbf{p}')}{(2\pi)^6 \Delta T n_e^H \bar{n}_e^L n_h^H \bar{n}_h^L}. \quad (\text{S69})$$

Here $(\dot{j}_{\mathbf{k}+})_{\text{ee}}$ is given by Eq. (S50), where we take only $l = 0$. We assume that \mathbf{k} and \mathbf{k}' describe states in the UFB and \mathbf{p} and \mathbf{p}' in the LFB, i.e., $(\nu, \nu', \mu, \mu') = (+, +, -, -)$, according to the notations in Eq. (S50). For concreteness, we consider an EFM phase for electrons in the UFB (the analysis for the EFI phase is similar). The holes in the LFB form a non-degenerate distribution. The range of \mathbf{k}' -integral is all the states in the high-energy sector of the UFB, corresponding to $\varepsilon_{\mathbf{k}'+} > \Delta_F/2 + \mu_e$. Subsequently, the range of \mathbf{k} -integral is all the states in the low-quasienergy sector of the UFB,

$\Delta_F/2 < \varepsilon_{\mathbf{k}+} < \Delta_F/2 + \mu_e$. The \mathbf{p} and \mathbf{p}' -integrals are in the range $-\Delta_F/2 - T < \varepsilon_{\mathbf{p}-} < -\Delta_F/2$ and $\varepsilon_{\mathbf{p}'-} < -\Delta_F/2 - T$, according to the definition of the low and high-quasienergy sectors in the LFB, see the text surrounding Eq. (S42) and Fig. S2.

In the limit $\Delta T/T \rightarrow 0$, we approximate $(\dot{f}_{\mathbf{k}+})_{ee}$ by the leading (linear) order in ΔT such that γ_{ee} is a constant in ΔT by the definition [Eq. (S69)]. To extract the first-order term in ΔT from $(\dot{f}_{\mathbf{k}+})_{ee}$, we describe the electron and hole distributions as Fermi functions and use this description in the expression for $F_{ee}(\mathbf{k}+, \mathbf{p}-; \mathbf{k}' + \mathbf{p}'-)$ [given in Eq. (S51)]. In particular, we use the property $1 - \frac{1}{e^x + 1} = e^x \left(\frac{1}{e^x + 1} \right)$ to switch between f and \bar{f} -terms in Eq. (S51), leading to

$$F_{ee} = (1 - e^{\Delta\varepsilon_1/T_e} e^{\Delta\varepsilon_2/T_h}) F(\mathbf{k}+, \mathbf{k}'+) F(\mathbf{p}-, \mathbf{p}'-), \quad (\text{S70})$$

where $F(\mathbf{k}\nu, \mathbf{k}'\nu')$ is defined in Eq. (S47). The term in the brackets in the RHS of Eq. (S70) is linear to the leading order in ΔT , i.e., $1 - e^{\Delta\varepsilon_1/T_e} e^{\Delta\varepsilon_2/T_h} = \Delta\varepsilon_1 \Delta T/T^2 + \mathcal{O}(\Delta T^2)$ (since by energy conservation $\Delta\varepsilon_1 + \Delta\varepsilon_2 = 0$). We thus take only the zeroth order in ΔT of the rest of the terms in the RHS, to arrive at

$$F_{ee}(\mathbf{k}+, \mathbf{p}-; \mathbf{k}' + \mathbf{p}'-) \approx \frac{\Delta\varepsilon_1 \Delta T}{T^2} F(\mathbf{k}+, \mathbf{k}'+) F(\mathbf{p}-, \mathbf{p}'-), \quad (\text{S71})$$

where all the Fermi functions in F are evaluated at $\Delta T = 0$.

Next, we evaluate $\mathcal{P}_{ee}^{(0)}$, employing Eq. (S52) and Floquet states given in Eq. (S10), which leads to

$$\begin{aligned} \mathcal{P}_{ee}^{(0)}(\mathbf{k}+, \mathbf{p}-; \mathbf{k}' + \mathbf{p}'-) &\approx \\ &\approx (U/a^2)^2 \cos^2[(\theta - \phi)/2] \cos^2[(\theta' - \phi')/2]. \end{aligned} \quad (\text{S72})$$

Here, we used polar coordinates, $\mathbf{k} = (k \sin(\theta), k \cos(\theta))$, $\mathbf{k}' = (k' \sin(\theta'), k' \cos(\theta'))$, $\mathbf{p} = (p \sin(\phi), p \cos(\phi))$, and $\mathbf{p}' = (p' \sin(\phi'), p' \cos(\phi'))$.

Once we estimated all the ingredients appearing in the definition of $(\dot{f}_{\mathbf{k}+})_{ee}$ [Eq. (S50)], we are in the position to evaluate the integral in Eq. (S69). To this end, we first replace each of the two-dimensional momenta integrals by the energy and angle integrals using polar representation. For example, $\int \frac{d^2\mathbf{k}}{(2\pi)^2} = \int d\varepsilon_k D_F(\varepsilon_k) \int \frac{d\theta}{2\pi}$, where $D_F(\varepsilon_k)$ is the density of states [given in Eq. (S23)].

We start with the angular part of the integral. We fix two of the angles, θ and θ' , and find the other two, ϕ and ϕ' by momentum conservation. If the scattering is exactly at the resonance ring, i.e., $k = k' = p = p' = k_R$, conservation of the total momentum implies either (i) $\phi = \theta'$ and $\phi' = \theta$, or (ii) $\phi = \pi + \theta$ and $\phi' = \pi + \theta'$, see Fig. S5a and b. In practice, the momentum amplitude fluctuates around k_R , due to the thermal and doping-induced width of the distributions, leading to fluctuations of the angles, $\phi = \phi_0 + \delta\phi$ and $\phi' = \phi'_0 + \delta\phi'$, where ϕ_0 and ϕ'_0 are the solutions for ϕ and ϕ' in terms of θ and θ' which we found in the cases (i) and (ii) above. To find how $\delta\phi$ and $\delta\phi'$ depend on the fluctuations in the amplitudes

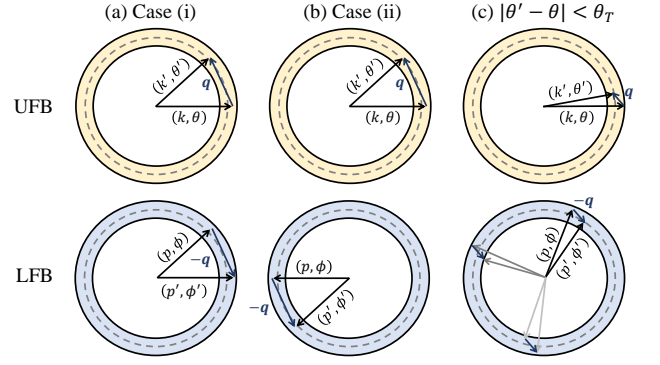


FIG. S5. Electron-electron scattering processes leading to equilibration of the electron and hole distributions. Yellow (top) and blue (bottom) rings indicate the area of states in the reciprocal space available for scattering near the resonance ring (gray dashed line), the width of the ring is approximately $\sim k_R \theta_T$. The black arrows in the upper circle represent the momentum of the electron in the UFB before and after the scattering event, with a momentum transfer \mathbf{q} indicated by blue arrow. Similarly, the black arrows in the figure at the bottom correspond to momentum of an electron in the LFB before and after the transition, with a momentum transfer $-\mathbf{q}$, due to total momentum conservation. (a). Possible scattering event for the case (i), for which $\phi \approx \theta'$ and $\phi' \approx \theta$. (b). Possible scattering event for the case (ii), for which $\phi \approx \pi + \theta$ and $\phi' \approx \pi + \theta'$. This case is Pauli suppressed as it scatters between almost orthogonal pseudospin states [cf. Eq. (S72)]. (c). Possible scattering events when $|\theta' - \theta| < \theta_T$. In this case, there are many possible configurations of the angle ϕ' , all satisfying momentum conservation.

(defined as $\delta k = k - k_R$ and similarly for other momenta), we expand the conservation of momentum in the \hat{x} and \hat{y} directions to the first order in the fluctuations. The linearized equations for the case (i) read

$$\delta\phi k_R \sin(\theta') = \delta k - \delta p' + (\delta p - \delta k') \cos(\theta') \quad (\text{S73a})$$

$$\delta\phi k_R \cos(\theta') = k_R \delta\phi' + (\delta k' - \delta p) \sin(\theta'), \quad (\text{S73b})$$

where we set $\theta = 0$, as the system is rotational symmetric. The momentum-conserving δ -function for the case (i) then reads

$$\delta_1^{(2)}(\mathbf{k} + \mathbf{p} - \mathbf{k}' - \mathbf{p}') = \frac{\delta(\phi - \theta' - \delta\phi_1) \delta(\phi' - \theta - \delta\phi'_1)}{k_R^2 |\sin(\theta')|}, \quad (\text{S74})$$

where $\delta\phi_1$ and $\delta\phi'_1$ obtained from the solution to Eq. (S73) for $\delta\phi$ and $\delta\phi'$ as functions of $\delta k, \delta k', \delta p, \delta p'$ and θ' . Next, we consider the case (ii). Here, the momentum conserving δ -functions reads

$$\begin{aligned} \delta_2^{(2)}(\mathbf{k} + \mathbf{p} - \mathbf{k}' - \mathbf{p}') &= \\ &= \frac{\delta(\phi - \pi - \theta - \delta\phi_2) \delta(\phi' - \pi - \theta' - \delta\phi'_2)}{k_R^2 |\sin(\theta')|}. \end{aligned} \quad (\text{S75})$$

In the case (ii), $\delta\phi_2$ and $\delta\phi'_2$ are obtained from equations similar to Eq. (S73) with an exchange $\delta p \leftrightarrow \delta p', \delta\phi \leftrightarrow$

$\delta\phi'$. The full momentum conserving δ -function is a sum of Eqs. (S74) and (S75).

The cases (i) and (ii) above, apply when $|\mathbf{k}' - \mathbf{k}| \gg \delta k, \delta k', \delta p, \delta p'$. We introduce a cutoff parameter, θ_T such that for $|\theta'| > \theta_T$, the momentum conservation is ensured by the sum of Eqs. (S74) and (S75). (Recall that $|\mathbf{k}' - \mathbf{k}| \approx k_R |\theta'|$ for $\theta = 0$ and small θ' .) This cutoff depends on the average values of $\delta k, \delta k', \delta p$ and $\delta p'$, therefore it is in general a function of T and μ_e . However as we shall show later, the result only weakly (logarithmically) depends on the cutoff, therefore its T and μ_e dependence is not significant. For $|\theta'| < \theta_T$, the momentum can be conserved for many values of ϕ' , see Fig. S5c. In this case, we fix ϕ' and $\theta = 0$ and find the corresponding angles ϕ and θ' from the momentum conservation. Defining $\phi = \phi' + \delta\phi$, where $\delta\phi$ is small (of the order of θ'), we arrive at the equations for $\delta\phi$ and θ' ,

$$\delta\phi k_R \sin(\phi') = \delta k - \delta k' + (\delta p - \delta p') \cos(\phi') \quad (\text{S76a})$$

$$\delta\phi k_R \cos(\phi') = k_R \theta' + (\delta p' - \delta p) \sin(\phi'). \quad (\text{S76b})$$

The momentum conserving δ -function then reads

$$\delta_3^{(2)}(\mathbf{k} + \mathbf{p} - \mathbf{k}' - \mathbf{p}') = \frac{\delta(\phi - \phi' - \delta\phi_3)\delta(\theta' - \theta'_3)}{k_R^2 |\sin(\phi')|}. \quad (\text{S77})$$

where $\delta\phi_3$ and θ'_3 are the solutions to Eqs. (S76). Eq. (S77) is valid above approximately same cutoff $|\phi'| > \theta_T$.

We are now ready to perform the angular integral in Eq. (S69). The only angle-dependent parts in this integral are the momentum-conserving δ -functions [Eqs. (S74), (S75) and (S77)] and $\mathcal{P}_{ee}^{(0)}$ given in Eq. (S72). We define an angular integral over each of the δ -functions, $I_{\text{ang}} = I_{\text{ang}}^{(1)} + I_{\text{ang}}^{(2)} + I_{\text{ang}}^{(3)}$, where $I_{\text{ang}}^{(1,2)} = \int_{|\theta'| > \theta_T} \frac{d\theta d\theta' d\phi d\phi'}{(2\pi)^4} \delta_{1,2}^{(2)} \mathcal{P}_{ee}^{(0)}$, and $I_{\text{ang}}^{(3)} = \int_{|\theta'| < \theta_T, |\phi'| > \theta_T} \frac{d\theta d\theta' d\phi d\phi'}{(2\pi)^4} \delta_3^{(2)} \mathcal{P}_{ee}^{(0)}$. The integral over θ can be trivially performed in each of $I_{\text{ang}}^{(i)}$, yielding 2π . Next, we perform the integrals over the δ -functions, leading to

$$I_{\text{ang}}^{(1)} = \frac{U^2}{a^4} \int \frac{d\theta'}{(2\pi)^3} \frac{\cos^2(\frac{\theta' + \delta\phi_1}{2}) \cos^2(\frac{\theta' - \delta\phi'_1}{2})}{k_R^2 |\sin(\theta')|} \quad (\text{S78})$$

$$I_{\text{ang}}^{(2)} = \frac{U^2}{a^4} \int \frac{d\theta'}{(2\pi)^3} \frac{\sin^2(\frac{\delta\phi_2}{2}) \sin^2(\frac{\delta\phi'_2}{2})}{k_R^2 |\sin(\theta')|} \quad (\text{S79})$$

$$I_{\text{ang}}^{(3)} = \frac{U^2}{a^4} \int \frac{d\phi'}{(2\pi)^3} \frac{\cos^2(\frac{\phi' + \delta\phi_3}{2}) \cos^2(\frac{\theta'_3 - \phi'}{2})}{k_R^2 |\sin(\phi')|} \quad (\text{S80})$$

The θ' -integral in Eqs. (S78) and (S79) and ϕ' -integral in Eq. (S80) are in the range $[\theta_T, 2\pi - \theta_T]$.

The last integral [Eq. (S80)] is nonzero when $|\theta'_3| < \theta_T$ [recall that θ'_3 is obtained from Eqs. (S76)]. We choose θ_T to be large enough for this condition to be satisfied for any allowed value of $\delta k, \delta k', \delta p, \delta p', \delta\phi$ and ϕ' . Choosing

too large value of θ_T will lead to an underestimate for the total rate, as some of the values of θ' will not be included in the calculation.

Turning back to Eqs. (S78)-(S80), we neglect small angles $\delta\phi_1$ and $\delta\phi'_1$ with respect to θ' in Eq. (S78), and $\delta\phi_3$ and θ'_3 with respect to ϕ' in Eq. (S80). We also neglect $I_{\text{ang}}^{(2)}$ as its value is proportional to the squares of small angles $\propto \delta\phi_2^2 \delta\phi'_2{}^2$. Therefore, we arrive at $I_{\text{ang}} \approx \frac{2U^2}{(2\pi)^3 a^4 k_R^2} \int d\theta' \frac{\cos^4(\theta'/2)}{|\sin(\theta')|}$, where $\theta' \in [\theta_T, 2\pi - \theta_T]$. This results, in the limit of small θ_T , in $I_{\text{ang}} \approx U^2 \frac{2 \log(2/\theta_T) - 1}{(2\pi)^3 a^4 k_R^2}$.

We note that in the calculation of the angular integral we omitted parameter regimes in which the angular integral can not be separated from the amplitude integral, by introducing the cutoff θ_T . As the angular phase space corresponding to this regime is small, its omission only weakly affects the final result.

Now, we turn to the integration over the energy-dependent terms arising from F_{ee} [Eq. (S71)] and $\delta(\Delta\varepsilon_1 + \Delta\varepsilon_2)$. Recall, that we consider an EFM phase for the electrons in the UFB, and describe the distribution of holes by Eq. (S29). We define I_{en} as the energy integral over the energy-dependent terms, given by

$$I_{\text{en}} = \int_0^{\mu_e} d\varepsilon_k \int_{\mu_e}^{\infty} d\varepsilon_{k'} \int_{-T}^0 d\varepsilon_p \int_{-\infty}^{-T} d\varepsilon_{p'} \\ D_{\text{F}}(\varepsilon_k) D_{\text{F}}(\varepsilon_{k'}) D_{\text{F}}(-\varepsilon_p) D_{\text{F}}(-\varepsilon_{p'}) \frac{\Delta T (\varepsilon_{k'} - \varepsilon_k)}{T^2} \\ \delta(\varepsilon_{k'} - \varepsilon_k + \varepsilon_{p'} - \varepsilon_p) \bar{f}_{\varepsilon_{k'}} + \bar{f}_{\varepsilon_k} + \bar{f}_{\varepsilon_{p'}} - \bar{f}_{\varepsilon_{p'-}}, \quad (\text{S81})$$

where ε_k and $\varepsilon_{k'}$ are accounted from the bottom of the UFB and ε_p and $\varepsilon_{p'}$ are accounted from the top of the LFB (and are negative). Assuming the electrons in the UFB are deep in the EFM regime, $\mu_e/T \gg 1$, we approximate $D_{\text{F}}(\varepsilon_k)$ and $D_{\text{F}}(\varepsilon_{k'})$ by $D_{\text{F}}(\mu_e)$ and take the lower limit of the ε_k -integral to $-\infty$. We set $\bar{f}_{\varepsilon_{p'-}} \approx z_h e^{\varepsilon_{p'}/T}$ and $\bar{f}_{\varepsilon_{p'}} \approx 1$, assuming $z_h \ll 1$, while $\bar{f}_{\varepsilon_k} = \frac{1}{e^{-(\varepsilon_k - \mu_e)/T} + 1}$ and $\bar{f}_{\varepsilon_{k'}} = \frac{1}{e^{(\varepsilon_{k'} - \mu_e)/T} + 1}$. To evaluate the integral, we shift ε_k and $\varepsilon_{k'}$ by μ_e and rescale all the energies by T , $\varepsilon_k = \mu_e - Tx$, $\varepsilon_{k'} = \mu_e + Ty$, $\varepsilon_p = -Tz$, and $\varepsilon_{p'} = -Tw$, leading to

$$I_{\text{en}} = C_1 C_2 \frac{\Delta T}{T^2} n_e^{\text{H}} \bar{n}_e^{\text{L}} n_h^{\text{H}} \bar{n}_h^{\text{L}}, \quad (\text{S82})$$

where

$$C_1 = \int_0^{\infty} dx \int_0^{\infty} dy \int_0^1 dz \int_1^{\infty} dw \frac{y+x}{\sqrt{zw}} \times \\ \times \delta(y+x+z-w) \frac{1}{e^x + 1} \frac{1}{e^y + 1} e^{-z} \approx 0.94, \quad (\text{S83})$$

and $C_2 = [2\sqrt{\pi} \text{erfc}(1) \log^2(2)]^{-1} \approx 3.73$. In this calculation we used explicit expressions of the densities of electron and hole subpopulations given in Eqs. (S40) and (S43).

Combining the angular and energy integrals, we arrive at $\gamma_{ee} = \frac{(2\pi)^3 a^4 I_{\text{ang}} I_{\text{en}}}{\Delta T n_e^H \bar{n}_e^L n_h^H \bar{n}_h^L}$ leading to

$$\gamma_{ee} \approx \frac{C_\gamma U^2}{k_R^2 T^2}, \quad (\text{S84})$$

where $C_\gamma = [2 \log(2/\theta_T) - 1] C_1 C_2$. The same calculation for the electrons in the EFI phase and for the holes, leads to a similar expression for γ_{ee} , up to a numerical factor $\mathcal{O}(1)$.

H. Solution of the extended rate equations

Now, we are ready to solve Eqs. (S44) and (S45). Our goal is to find the dependence of the effective temperatures and chemical potentials of the electrons and holes on the speed of sound, v_s , the doping, Δn and the ‘‘balance parameter’’, κ [defined in Eq. (S37)].

1. Electron and hole temperatures for $\gamma_{ee} = 0$

First, we assume $\gamma_{ee} = 0$, which corresponds to the model used for the full numerical simulation of the kinetic equation. Later, we show that if we include a finite γ_{ee} in the model, the distribution of the electrons, whose density is significantly larger than the density of the holes, will be almost unaffected. As a result, we expect the predicted phase boundary in Fig. 3 in the main text, to remain almost unchanged in the presence of electron-electron scattering processes which equilibrate the electron and hole populations. For $\gamma_{ee} = 0$, each temperature, T_e or T_h , is obtained from its respective equation, Eq. (S44) or Eq. (S45).

In what follows, we obtain T_e from the solution to Eq. (S44), which for $\gamma_{ee} = 0$ reads

$$\Lambda_{\text{intra}}(T_e) n_e^H \bar{n}_e^L = \Lambda_{\text{inter}} n_e^L n_h. \quad (\text{S85})$$

First, we assume an EHM phase. Our strategy in the analysis, is to replace the densities of subpopulations of electrons by their expressions, given in Eq. (S40). Then instead of μ_e , we substitute its expression in terms of n_e

$$\mu_e \approx n_e^2 / (4D_0^2 \Delta_F), \quad (\text{S86})$$

obtained by inverting Eq. (S31), where $D_0 = m_*/2\pi$ [see definition below Eq. (S23)]. We substitute $n_h = \kappa/n_e$ [cf. Eq. (S36)] and explicit expressions of Λ_{inter} and Λ_{intra} [Eq. (S65) and (S68)] in Eq. (S85) to extract,

$$T_e = \left(\frac{6k_R^3 v_s^3 \kappa n_e^2}{4 \log^2(2) \Delta_F^3 D_0^4} \right)^{1/4}. \quad (\text{S87})$$

Note that in Eq. (S87), T_e is expressed as a function of n_e . Recall, however, that n_e is an explicit function of Δn and κ , as follows from Eq. (S38). Therefore, Eq. (S87)

expresses T_e as a function of κ and Δn . The power $1/4$ in Eq. (S87) arises from the LHS term in Eq. (S85). This term is proportional to T_e^4 , as follows from the definitions of Λ_{intra} [see Eq. (S68)], n_e^H , and \bar{n}_e^L [see Eq. (S40)]. Finally, we divide the expression for μ_e given in Eq. (S86) by T_e given in Eq. (S87) to arrive at

$$\frac{\mu_e}{T_e} = \left(\frac{C_{\text{EFM}} n_e^6}{\Delta_F D_0^4 k_R^3 v_s^3 \kappa} \right)^{1/4}, \quad (\text{S88})$$

where $C_{\text{EFM}} = \log^2(2)/384 \approx 0.00125$. In Eq. (S88), n_e can be expressed as a function of Δn and κ , using Eq. (S38).

Next, we solve Eq. (S85) in the EFI phase. Here, we replace the electron subpopulation densities by expressions given in Eq. (S41) and substitute $n_h = \kappa/n_e$ [cf. Eq. (S36)]. We then extract an expression for T_e from the resulting equation, leading to

$$T_e = \left(\frac{3\text{erf}(1)}{\text{erfc}(1)} \frac{k_R^3 v_s^3 \kappa}{\Delta_F^{3/2} D_0 n_e} \right)^{2/5}. \quad (\text{S89})$$

Next, we find z_e , using

$$z_e = n_e / (\sqrt{\pi} T_e D_F(T_e)) \quad (\text{S90})$$

obtained from Eq. (S32). We substitute Eq. (S89) in Eq. (S90) to obtain

$$z_e \approx \left(\frac{C_{\text{EFI}} n_e^6}{\Delta_F D_0^4 k_R^3 v_s^3 \kappa} \right)^{1/5}, \quad (\text{S91})$$

where $C_{\text{EFI}} = \text{erfc}(1)/(3\pi^{5/2} \text{erf}(1)) \approx 0.0036$. Recall that μ_e/T_e can be extracted from z_e using the relation $\mu_e/T_e = \log(z_e)$.

We note that the phenomenological analysis outlined in this chapter is aimed to only capture the right scaling of T_e and μ_e as functions of the parameters of the system (i.e., κ , Δn , v_s , etc.), and not the values of the numerical coefficients C_{EFM} and C_{EFI} . We use these coefficients as fitting parameters in Fig. 3 in the main text. The best fit is obtained when $C_{\text{EFM}} = C_{\text{EFI}} \equiv C$.

Next, we consider the distribution of holes in the LFB. The analysis of Eq. (S45) in the regime $\gamma_{ee} = 0$ is similar to the analysis of Eq. (S85) in the EFI phase, above. The density of holes and their subpopulations are given by Eqs. (S33) and (S43). In this case, T_h and z_h are given by

$$T_h = \left(\frac{3\text{erf}(1)}{\text{erfc}(1)} \frac{k_R^3 v_s^3 \kappa}{\Delta_F^{3/2} D_0 n_h} \right)^{2/5}, \quad z_h \approx \left(\frac{C_{\text{EFI}} n_h^6}{\Delta_F D_0^4 k_R^3 v_s^3 \kappa} \right)^{1/5}. \quad (\text{S92})$$

Finally, we verify that Eq. (S92) is consistent with an assumption of the non-degenerate hole distribution, when the system is doped with electrons. To this end, we show that $z_h \rightarrow 0$ when we take $\kappa \rightarrow 0$ for fixed $\Delta n > 0$. In this limit, $n_h \approx \kappa/\Delta n$, see Eq. (S38). Substituting the latter

relation in Eq. (S92), we find $z_h \sim \kappa$. Therefore, the nondegenerate-hole-gas assumption is consistent; indeed $z_h \rightarrow 0$ as $\kappa \rightarrow 0$. Interestingly, note that this assumption is not consistent with Eq. (S92) when the system is substantially doped with holes, i.e., when $\Delta n \ll -\kappa$. In this case, $n_h \approx |\Delta n|$, leading to $z_h \sim \kappa^{-1/5}$, i.e., $z_h \rightarrow \infty$ as $\kappa \rightarrow 0$. In fact, when the system is substantially hole doped, the holes form a degenerate distribution analogous to the EFM phase for electrons in an electron-doped system.

2. Electron and hole temperatures in the presence of electron-electron scattering

In subsection III H 1 we considered the case $\gamma_{ee} = 0$, for which electron-electron interactions do not equilibrate the electron and hole distributions. Now, we consider the regime where the electron-electron scattering is significant, i.e., when γ_{ee} is finite. In this regime, both Eqs. (S44) and (S45) depend on T_e and T_h and need to be solved jointly. Fig. S6 shows T_e and T_h obtained from a numerical solution of Eqs. (S44) and (S45) in the EFM and EFI regimes. Here, we treat γ_{ee} as a constant varied from $\gamma_{ee} = 0$ to large values of γ_{ee} , where interband thermalization is significant. When $\gamma_{ee} = 0$, the electron and hole temperatures are found in Sec. III H 1. Here, we denote by $T_{e,0}$ the temperature of the distribution of the electrons given in Eq. (S87) if the electrons exhibit an EFM phase and Eq. (S89) if they exhibit an EFI phase. Likewise, we denote by $T_{h,0}$ the temperature of the distribution of holes for $\gamma_{ee} = 0$, given in Eq. (S92).

As γ_{ee} is increased, the difference between the temperatures of the two distribution is reduced until, in the limit $\gamma_{ee} \rightarrow \infty$, they reach a common temperature, T_∞ . Predictably, the minority population is more affected by this equilibration, while the temperature of the majority population is only slightly changed. For large values of γ_{ee} , as T_h tends towards T_∞ , the difference between $T_h(\gamma_{ee})$ and $T_{h,0}$ is proportional to $\sim 1/\gamma_{ee}$. In what follows, we solve analytically Eqs. (S44) and (S45) in the limit $\gamma_{ee} \rightarrow \infty$, to obtain an analytical expression for T_∞ in the EFM and EFI regimes. In this limit, the electron and hole temperatures are almost the same, $|\Delta T| \ll T$ [see discussion above Eq. (S44)]. Assuming this is the case, we can take only zeroth order in ΔT in all the terms in Eqs. (S44) and (S45), except of the terms proportional to γ_{ee} . Note that the term proportional to γ_{ee} is the same in both of these equations (up to a sign), thus cancels out upon addition of the two equations. The sum of Eqs. (S44) and (S45) then reads,

$$\Lambda_{\text{intra}}(T_\infty)(n_e^H \bar{n}_e^L + n_h^H \bar{n}_h^L) = \Lambda_{\text{inter}}(n_e^L n_h + n_h^L n_e). \quad (\text{S93})$$

Importantly, all the terms in Eq. (S93) depend only on the mean temperature, T_∞ , defined as $T_\infty = \lim_{\gamma_{ee} \rightarrow \infty} T$, where in this limit, $\Delta T = 0$. In what follows, we use Eq. (S93) to determine T_∞ . Similarly, ΔT can be found from the difference between Eqs. (S44) and (S45).

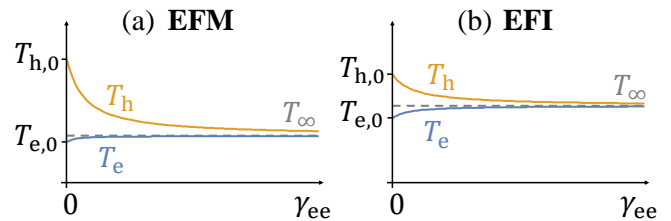


FIG. S6. Equilibration of the electron and hole distribution due to electron-electron scattering. The temperatures of electrons in the UFB (T_e) and holes in the LFB (T_h) are obtained from the solution to Eqs. (S44) and (S45), as a function of γ_{ee} for typical system's parameters in (a) the EFM phase and (b) EFI phase. The temperatures $T_{e,0}$ and $T_{h,0}$ obtained at $\gamma_{ee} = 0$ are given in Eqs. (S87), (S89) and (S92). The temperature for $\gamma_{ee} \rightarrow \infty$, T_∞ , [given in Eqs. (S95) and (S96)] is indicated by the dashed line.

First, consider an EFM regime for the electrons. To simplify Eq. (S93), we neglect the term proportional to $n_h^H \bar{n}_h^L$ relative to $n_e^H \bar{n}_e^L$ in the limit $\kappa \rightarrow 0$. We also approximate $n_e^L \approx n_e$ and use $n_h^L = \text{erf}(1)n_h$ [cf. Eqs. (S40) and (S43)]. As a result, Eq. (S93) simplifies to

$$\Lambda_{\text{intra}}(T_\infty)n_e^H \bar{n}_e^L = C' \Lambda_{\text{inter}} n_e n_h, \quad (\text{S94})$$

where $C' = 1 + \text{erf}(1) \approx 1.84$. Note that Eq. (S94) is reminiscent of Eq. (S85) up to a constant, C' . Subsequently, the mean temperature obtained from the solution to Eq. (S94) is related to the solution to Eq. (S85) by

$$T_\infty = (C')^{1/4} T_{e,0}, \quad (\text{S95})$$

where $T_{e,0}$ is given in Eq. (S87).

Now, we turn to the analysis of the EFI regime. This regime always arises at low-electron doping, which also includes half-filling (where $n_e = n_h$). Therefore in this case, we can not neglect the hole density with respect to the electron one, in Eq. (S93), as we did in the analysis of the EFM regime, above. To extract T_∞ from Eq. (S93), we replace the densities of subpopulations by their expressions given in Eqs (S41) and (S43) in terms of n_e , n_h and T_∞ [substituting T_∞ instead of T_e and T_h]. An extraction of T_∞ from the resulting equation yields

$$T_\infty = \left(\frac{2n_e}{n_e + n_h} \right)^{5/2} T_{e,0}, \quad (\text{S96})$$

where $T_{e,0}$ is given in Eq. (S89). At half-filling $T_\infty = T_{e,0}$, and away from the half-filling, as $n_h/n_e \rightarrow 0$, $T_\infty \rightarrow 2^{2/5} T_{e,0}$.

To conclude, in this section we showed that for an electron doped system, and in the presence of strong electron-electron scattering, the temperature of the distribution of the electrons in the UFB is close to the temperature obtained by setting $\gamma_{ee} = 0$, given by Eqs. (S87) and (S89). In contrast, the temperature of the distribution of the

holes may substantially change due to electron-electron scattering relative to temperature obtained for $\gamma_{ee} = 0$. However the properties of the distribution of holes in the LFB only weakly effect the critical interaction strength, and therefore the phase diagram of the system [cf. Fig. 2a in the main text] (which is mainly set by the properties of the distribution of the electrons in the UFB). Therefore, we expect the phase diagram obtained for $\gamma_{ee} = 0$ to give a good description of the phase diagram of the system in the presence of a nonzero value of γ_{ee} .

I. Interpolation between the EFM and the EFI regimes

In Sec. III H 1, we obtained expressions for μ_e/T_e in the EFM and EFI regimes for $\gamma_{ee} = 0$, see Eqs. (S88) and (S91). Here we discuss an interpolation between the two equations which we used to fit the numerical data in Fig. 3 in the main text. We assume $C_{\text{EFM}} = C_{\text{EFI}} \equiv C$, which yields the best fit for the data in Fig. 3, and define

$$x_e \equiv \zeta n_e^6 / (v_s^3 \kappa), \quad (\text{S97})$$

where $\zeta = C / (\Delta_F D_0^4 k_R^3)$. Using Eq. (S97), we rewrite Eqs. (S88) and (S91) as $\mu_e/T_e \approx x_e^{1/4}$ in the EFM regime and $e^{\mu_e/T_e} \approx x_e^{1/5}$ in the EFI regime. The transition between the two regimes occurs in the crossover area, corresponding to $\mu_e/T_e = \mathcal{O}(1)$.

Now we introduce an analytic function which interpolates between the values of μ_e/T_e in the two regimes. This function needs to interpolate between power-law (in the EFM regime) and exponential (in the EFI regime) functions. Therefore, we expect it to be of the form of the complete Fermi-Dirac integral function,

$$\mathcal{F}_j(\lambda \mu_e/T_e) = x_e^\eta. \quad (\text{S98})$$

Here $\mathcal{F}_j(x) = \frac{1}{\Gamma(j+1)} \int_0^\infty \frac{t^j}{e^{t-x} + 1} dt$, is the complete Fermi-Dirac integral and $\Gamma(j+1) = j\Gamma(j)$; $\Gamma(1) = 1$ is the Euler gamma function. The function in the LHS of Eq. (S98) has the following asymptotic values⁷,

$$\lim_{\mu_e/T_e \rightarrow -\infty} \mathcal{F}_j(\lambda \mu_e/T_e) = e^{\lambda \mu_e/T_e} \quad (\text{S99a})$$

$$\lim_{\mu_e/T_e \rightarrow \infty} \mathcal{F}_j(\lambda \mu_e/T_e) = \frac{(\lambda \mu_e/T_e)^{j+1}}{\Gamma(j+2)}. \quad (\text{S99b})$$

To obtain the right constants in the two asymptotic limits to match the dependencies in the EFM and EFI regimes, we require $\eta/\lambda = 1/5$, $\eta/(j+1) = 1/4$, and $\lambda^{j+1} = \Gamma(j+2)$. These conditions have a unique solution $j \approx -0.304$, $\lambda \approx 0.871$ and $\eta \approx 0.174$.

In order to use the interpolation in Fig. 3c in the main text, we need to obtain an expression for μ_e/T_e as a function of Δn . To this end, we invert Eq. (S98), and employ the definition of x_e [Eq. (S97)] to obtain

$$\mu_e/T_e = (1/\lambda) \mathcal{F}_j^{-1} \{ [\zeta n_e^6 / (v_s^3 \kappa)]^\eta \}, \quad (\text{S100})$$

where $\mathcal{F}_j^{-1}[\mathcal{F}_j(x)] = x$. Finally, we replace n_e by a function of Δn and κ , given in Eq. (S38). We fit the data in Fig. 3c by Eq. (S100) with a single fitting parameter ζ . The same fitting parameter is used for the curves shown in the Fig. 3. In order to fit the data in Figs. 3b and 3d, we used the equation for \tilde{U}_c [Eq. (10) in the main text], where we substituted Eq. (S100) for μ_e/T_e appearing inside the $\tilde{\Theta}$ -function. Eq. (10) depends also on μ_h/T_h , which from the analysis similar to the one leading to Eq. (S100), yields

$$\mu_h/T_h = (1/\lambda) \mathcal{F}_j^{-1} \{ [\zeta n_h^6 / (v_s^3 \kappa)]^\eta \}. \quad (\text{S101})$$

The fit in Figs. 3b and 3d is performed with the same value of ζ as in Fig. 3c. We used \tilde{U}_{ex} and \tilde{U}_{fs} as additional fitting parameters.

J. Evaluation of the optimal doping, Δn_*

Finally, we evaluate the optimal doping Δn_* , at which \tilde{U}_c exhibits a deep [cf. Figs. 3b and d in the main text]. The optimal doping is defined by

$$\left. \frac{\partial \tilde{U}_c}{\partial \Delta n} \right|_{\Delta n = \Delta n_*} = 0, \quad (\text{S102})$$

where \tilde{U}_c is given in Eq. (10) in the main text, and we estimate μ_e/T_e and μ_h/T_h by Eqs. (S100) and (S101) and n_e and n_h by Eq. (S38). For simplicity, we neglect the term proportional to \tilde{U}_{fs} as it is constant in Δn , and neglect the term proportional to the density of holes, as its contribution is negligible in the electron-doped system. The approximate expression for \tilde{U}_c then reads

$$\tilde{U}_c \approx \tilde{n}_e / \tilde{\Theta}(\mu_e/T_e). \quad (\text{S103})$$

As κ is a weak function of Δn near the phase boundary (see Fig. S10), we neglect its derivative with respect to Δn . Therefore, instead of finding the minimum with respect to Δn , we can find the minimum with respect to n_e [which according to Eq. (S38) is only a function of κ and Δn] for fixed κ . Replacing the Δn -derivative in Eq. (S102) by n_e -derivative and using the approximate form of \tilde{U}_c given in Eq. (S103), we arrive at

$$\frac{\tilde{\Theta}'(\mu_e/T_e)}{\tilde{\Theta}(\mu_e/T_e)} = \frac{\lambda}{6\eta} \frac{\mathcal{F}_j'(\lambda \mu_e/T_e)}{\mathcal{F}_j(\lambda \mu_e/T_e)}, \quad (\text{S104})$$

where $\tilde{\Theta}'(x) = \frac{d}{dx} \tilde{\Theta}(x)$ and $\mathcal{F}_j'(x) = \frac{d}{dx} \mathcal{F}_j(x)$. Numerical solution of Eq. (S104) leads to $\mu_e/T_e \approx 1.13$ which, using Eq. (S98), corresponds to $x_e = c_*$, where $c_* \approx 2.03$. Finally, using Eq. (S97), we find the density at the optimal doping,

$$n_{e,*} = (c_* v_s^3 \kappa / \zeta)^{1/6}. \quad (\text{S105})$$

The optimal doping as a function of $n_{e,*}$ is given by $\Delta n_* = n_{e,*} - \kappa / n_{e,*}$ [as follows from Eq. (S38)]. In the limit $\kappa \rightarrow 0$, this simplifies to $\Delta n_* \approx n_{e,*}$.

IV. PHASE TRANSITION IN THE PRESENCE OF TWO TIME-REVERSAL PARTNERS

In the main text and throughout this supplement, we have discussed a model describing half of the degrees of freedom of a time-reversal symmetric semiconductor [see Eq. (2) in the main text]. In this section, we generalize this model to a model for a material which is time-reversal symmetric (absent the drive). The model includes two copies considered in Eq. (2), which are related by time reversal symmetry. This model is described by the Hamiltonian

$$\hat{\mathcal{H}}^{\text{TR}}(t) = \sum_{\mathbf{k}} \hat{\mathbf{c}}_{\mathbf{k}}^{\dagger} H_0^{\text{TR}}(\mathbf{k}, t) \hat{\mathbf{c}}_{\mathbf{k}} + \hat{\mathcal{H}}_{\text{intra}}^{\text{TR}} + \hat{\mathcal{H}}_{\text{inter}}^{\text{TR}}, \quad (\text{S106})$$

where $\hat{\mathbf{c}}_{\mathbf{k}}^{\dagger} = (\hat{c}_{\mathbf{k}\uparrow 1}^{\dagger}, \hat{c}_{\mathbf{k}\downarrow 1}^{\dagger}, \hat{c}_{\mathbf{k}\uparrow 2}^{\dagger}, \hat{c}_{\mathbf{k}\downarrow 2}^{\dagger})$, is a four-dimensional spinor; $\sigma = \{\uparrow, \downarrow\}$ denotes the pseudospin degree of freedom and $\tau = \{1, 2\}$ are two components related by time reversal. The non-interacting part of the Hamiltonian reads

$$H_0^{\text{TR}}(\mathbf{k}, t) = \begin{pmatrix} H_0(\mathbf{k}) + H_d(t) & 0 \\ 0 & H_0^*(-\mathbf{k}) + H_d(t) \end{pmatrix}, \quad (\text{S107})$$

where $H_0(\mathbf{k}) = E_0 + (|\mathbf{k}|^2/2m_* + E_g/2) + \lambda_0 \mathbf{k} \cdot \boldsymbol{\sigma}$ and $H_d(t) = V \cos(\Omega t) \boldsymbol{\sigma}^z$, in accordance with the definitions in Eq. (1) in the main text. We consider contact interaction of electrons of the same time-reversal components,

$$\hat{\mathcal{H}}_{\text{intra}}^{\text{TR}} = \int d^2\mathbf{r} \sum_{\tau=1,2} U \hat{n}_{\uparrow\tau}(\mathbf{r}) \hat{n}_{\downarrow\tau}(\mathbf{r}), \quad (\text{S108})$$

and contact interaction between the components

$$\hat{\mathcal{H}}_{\text{inter}}^{\text{TR}} = \int d^2\mathbf{r} U_{12} \hat{n}_1(\mathbf{r}) \hat{n}_2(\mathbf{r}), \quad (\text{S109})$$

where $\hat{n}_{\sigma\tau}(\mathbf{r}) = \int \frac{d^2\mathbf{q}}{(2\pi)^2} e^{i\mathbf{q}\cdot\mathbf{r}} \hat{c}_{\mathbf{k}+\mathbf{q}\sigma\tau}^{\dagger} \hat{c}_{\mathbf{k}\sigma\tau}$ and $\hat{n}_{\tau}(\mathbf{r}) = \hat{n}_{\uparrow\tau}(\mathbf{r}) + \hat{n}_{\downarrow\tau}(\mathbf{r}) - n_0/2$; n_0 is the density of electrons at half-filling.

We will study the system described by Eq. (S106) using the mean-field approximation. In particular, we consider two independent magnetizations and densities for each of the time-reversal partners ($\alpha = 1, 2$),

$$\mathbf{h}_{\alpha}(t) = -\frac{U}{\varpi} \sum_{\mathbf{k}} \langle \mathbf{c}_{\mathbf{k}}^{\dagger} (\boldsymbol{\sigma} \otimes \tau_{\alpha}) \mathbf{c}_{\mathbf{k}} \rangle \quad (\text{S110a})$$

$$n_{\alpha} = \frac{1}{\varpi} \int d^2\mathbf{r} \langle \hat{n}_{\alpha}(\mathbf{r}) \rangle, \quad (\text{S110b})$$

where ϖ is the volume of the system and $\tau_{1(2)} = \begin{pmatrix} 1(0) & 0 \\ 0 & 0(1) \end{pmatrix}$. Such a choice of an order parameter gives rise to the following mean-field Hamiltonian, $\hat{\mathcal{H}}_{\text{MF}}^{\text{TR}}(t) = \sum_{\mathbf{k}} \hat{\mathbf{c}}_{\mathbf{k}}^{\dagger} [H_0^{\text{TR}}(\mathbf{k}, t) + H_{\text{mag}}^{\text{TR}}(t)] \hat{\mathbf{c}}_{\mathbf{k}} + \varpi U_{12} n_1 n_2$, where

$$H_{\text{mag}}^{\text{TR}}(t) = \begin{pmatrix} \mathbf{h}_1(t) \cdot \boldsymbol{\sigma} & 0 \\ 0 & \mathbf{h}_2(t) \cdot \boldsymbol{\sigma} \end{pmatrix}. \quad (\text{S111})$$

For simplicity, we will treat the problem as that of an equilibrium system in the rotating frame using the rotating wave approximation (RWA) (see Sec. I) and minimize quasienergy with the mean-field band structure. This situation corresponds to $\kappa = 0$, i.e., a situation when the Floquet-Umklapp terms are neglected. Our goal is to find $\mathbf{h}_1(t)$, $\mathbf{h}_2(t)$, n_1 and n_2 such that the ground state of $H_{\text{MF}}^{\text{TR}}$ will minimize the full interacting Hamiltonian, given in Eq. (S106). We work in the limit of small doping, $\Delta n \equiv n_1 + n_2 \ll \mathcal{A}_{\text{R}}$.

Our choice of the order parameter [Eq. (S110)] leads to a mean-field Hamiltonian in which the two components related by time reversal are decoupled, for a state with fixed n_1 and n_2 . Therefore, each of these components can be analyzed independently. We consider circularly polarized magnetizations for both of them, $\mathbf{h}_{\tau}(t) = h_{\tau} e^{i\Omega t} (\hat{\mathbf{x}} - i\hat{\mathbf{y}})/2 + c.c.$ (see discussion following Eq. (8) in the main text). The phase of h_{τ} spontaneously breaks the rotational symmetry individually exhibited by each partner. In what follows we will present the analysis of the first component ($\tau = 1$); the analysis of its partner ($\tau = 2$) is identical. Our analysis partially follows the analysis presented in Ref. 8. We choose real and positive h_1 leading to the magnetization $h_1 \hat{\mathbf{x}}$ in the RWA, see Eq. (S13). The single-particle bandstructure in the mean-field and RWA is given by $\varepsilon_{\mathbf{k},\pm} = \pm \varepsilon_{\mathbf{k}}$ [see Eq. (S7)], where

$$\varepsilon_{\mathbf{k}} = \sqrt{\left(\frac{k^2}{2m_*} - \frac{\delta E}{2}\right)^2 + \left(\frac{\Delta_{\text{F}} k_x}{2k_{\text{R}}} + h_1\right)^2 + \left(\frac{\Delta_{\text{F}} k_y}{2k_{\text{R}}}\right)^2}. \quad (\text{S112})$$

The Fermi surface, corresponding to a fixed density n_1 , has a curved elliptic shape centered around the band-minimum point, $\mathbf{k}_0 \equiv -k_{\text{R}} \hat{\mathbf{x}}$, see Fig. S7a. We expand $\varepsilon_{\mathbf{k}}$ around \mathbf{k}_0 in polar coordinates, $k_x = k \cos(\theta)$, $k_y = k \sin(\theta)$, for small θ and $\delta k = k - k_{\text{R}}$. For simplicity, we assume $\Delta_{\text{F}} \ll \delta E$ and $h_1 \ll k_{\text{R}}^2/2m_*$ leading, up to the second order in δk and θ , to

$$\varepsilon_{\mathbf{k}} \approx \Delta_{\text{F}}/2 - h_1 + \frac{\delta E}{\Delta_{\text{F}}} \frac{\delta k^2}{m_*} + \frac{h_1}{2} \theta^2. \quad (\text{S113})$$

We define the kinetic energy density by $\mathcal{E}_{\text{kin}} = \int \frac{d^2\mathbf{k}}{(2\pi)^2} (\varepsilon_{\mathbf{k}} - h_1 \langle \sigma^x \rangle_{\mathbf{k}})$, where $\langle \sigma^x \rangle_{\mathbf{k}} = (\Delta_{\text{F}} k_x / 2k_{\text{R}} + h_1) / \varepsilon_{\mathbf{k}}$. In the definition of \mathcal{E}_{kin} we subtracted the term proportional to h_1 to avoid double counting of the magnetization energy, as it will be accounted in the interaction energy density \mathcal{E}_{int} , see below. The expansion of $\langle \sigma^x \rangle_{\mathbf{k}}$ up to the second order in δk and θ reads

$$\langle \sigma^x \rangle_{\mathbf{k}} \approx -1 + \frac{\Delta_{\text{F}} \delta k}{2k_{\text{R}}(\Delta_{\text{F}}/2 - h_1)} + \frac{\delta E \delta k^2}{m_* \Delta_{\text{F}} (\Delta_{\text{F}}/2 - h_1)} + \left(\frac{1}{2} + \frac{h_1}{\Delta_{\text{F}}/2 - h_1} \right) \theta^2. \quad (\text{S114})$$

The integral of \mathcal{E}_{kin} is over a curved elliptical area in k -space enclosed by the Fermi surface, characterized by the radial length k_e and the angular aperture θ_e , see

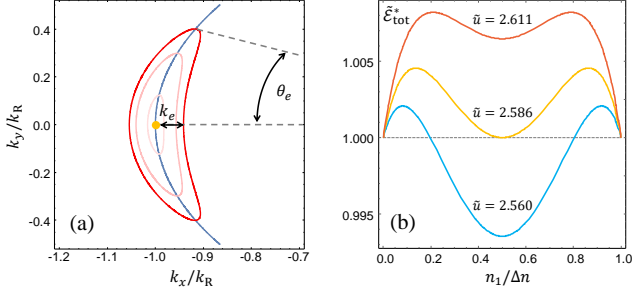


FIG. S7. (a). Fermi surface of one of the time-reversal partners in the symmetry broken phase, for three densities of electrons. The orange dot indicates the band-minimum point, \mathbf{k}_0 around which we expand the quasienergy. The opening angle (θ_e) and the width of the oval-shaped Fermi surface (k_e) are indicated on the figure. (b). The normalized optimal quasienergy, $\tilde{\mathcal{E}}_{\text{tot}}^*$, given in Eq. (S119), as a function of the normalized density $n_1/\Delta n$, for three values of the normalized inter-component interaction \tilde{u} . For $\tilde{u} < 4 - \sqrt{2} \approx 2.586$ the total energy has a single global minimum point at $n_1 = \Delta n/2$, corresponding to equal density of particles in the two time-reversal partners. For $\tilde{u} > 4 - \sqrt{2}$, the total energy has two global minimum points at $n_1 = 0$ and $n_1 = \Delta n$. In this case, one of the partners is fully occupied and the other is empty due to strong inter-partner repulsion. The two cases are separated by a critical point at $\tilde{u} = 4 - \sqrt{2}$, where the three possibilities coexist.

Fig. S7a. We parametrize this area by $\delta k = k_e x \cos(y)$ and $\theta = \theta_e x \sin(y)$, where $x \in [0, 1]$ and $y \in [0, 2\pi]$. By geometrical constraints, the values of k_e and θ_e are fixed by the density and the magnetization magnitude as follows,

$$k_e \theta_e = \frac{4\pi n_1}{k_R} \quad (\text{S115a})$$

$$\frac{k_e^2}{\theta_e^2} = \frac{\Delta_F m_* h_1}{\delta E} \frac{1}{2}. \quad (\text{S115b})$$

Using the new variables, the kinetic energy density reads $\mathcal{E}_{\text{kin}} = \frac{k_e k_R \theta_e}{(2\pi)^2} \int_0^1 dx \int_0^{2\pi} dy (\varepsilon_{\mathbf{k}} - h_1 \langle \sigma^x \rangle_{\mathbf{k}})$. Integration over x and y [the dependence of $\varepsilon_{\mathbf{k}}$ and $\langle \sigma^x \rangle_{\mathbf{k}}$ on x and y is given by Eqs. (S113) and (S114)] yields

$$\mathcal{E}_{\text{kin}}(n_1, h_1) \approx \frac{\Delta_F n_1}{2} + \sqrt{\frac{h_1}{2\Delta_F}} \frac{\pi n_1^2}{m_*} + \mathcal{O}(n_1^2 h_1^{3/2}). \quad (\text{S116})$$

Next, we evaluate the interaction energy density due to interaction of electron-electron interaction given in Eq. (S108), $\mathcal{E}_{\text{int}} = \frac{U}{\varpi^2} \sum_{\mathbf{q}\mathbf{k}\mathbf{k}'} \langle \hat{c}_{\mathbf{k}+\mathbf{q}\uparrow}^\dagger \hat{c}_{\mathbf{k}\uparrow} \hat{c}_{\mathbf{k}'-\mathbf{q}\downarrow}^\dagger \hat{c}_{\mathbf{k}'\downarrow} \rangle$. Using the Wick's theorem the interaction energy density simplifies to $\mathcal{E}_{\text{int}} = \frac{U}{4} (n_1^2 - \langle \sigma^x \rangle^2 - \langle \sigma^y \rangle^2 - \langle \sigma^z \rangle^2)$, where $\langle \sigma^\alpha \rangle \equiv \int \frac{d^2\mathbf{k}}{(2\pi)^2} \langle \sigma^\alpha \rangle_{\mathbf{k}}$. We further neglect $\langle \sigma^y \rangle^2$ and $\langle \sigma^z \rangle^2$ as they depend on higher powers of h_1 and n_1 . Substituting Eq. (S114) in the definition for $\langle \sigma^x \rangle$, we find $\langle \sigma^x \rangle \approx -n_1 + \frac{\pi n_1^2}{m_* \sqrt{2h_1 \Delta_F}} + \mathcal{O}(n_1^2 h_1^{1/2})$. Therefore, the

interaction energy density reads

$$\mathcal{E}_{\text{int}}(n_1, h_1) \approx \frac{U\pi n_1^3}{m_* \sqrt{8h_1 \Delta_F}} + \mathcal{O}(n_1^4 h_1^{-1}). \quad (\text{S117})$$

The kinetic and interaction energy densities of the time-reversal partner obtain expressions similar to Eqs. (S116) and (S117) with n_2 and h_2 replacing n_1 and h_1 . We define the full energy density of each of the components ($\tau = 1, 2$) as the sum of the kinetic and the interaction energy densities, $\mathcal{E}_{\text{full}}(n_\tau, h_\tau) = \mathcal{E}_{\text{kin}}(n_\tau, h_\tau) + \mathcal{E}_{\text{int}}(n_\tau, h_\tau)$. Finally, the total energy density includes the full energy densities of both components and the interaction between them [Eq. (S106)]. The total energy density of the system then reads

$$\begin{aligned} \mathcal{E}_{\text{tot}}(n_1, n_2, h_1, h_2) &= \\ &= \mathcal{E}_{\text{full}}(n_1, h_1) + \mathcal{E}_{\text{full}}(n_2, h_2) + U_{12} n_1 n_2. \end{aligned} \quad (\text{S118})$$

Next, we minimize \mathcal{E}_{tot} with respect to h_1, h_2 and n_1 (given $n_2 = \Delta n - n_1$). Due to the separable form of \mathcal{E}_{tot} , its minimum with respect to h_1 and h_2 for fixed n_1 and n_2 , coincides with the minimum of its respective terms. The minimum of $\mathcal{E}_{\text{full}}(n_1, h_1)$ with respect to h_1 yields $h_1^{\text{opt}} = \frac{1}{2} U n_1$. Similarly, the minimum of $\mathcal{E}_{\text{full}}(n_2, h_2)$ with respect to h_2 yields $h_2^{\text{opt}} = \frac{1}{2} U n_2$. Note that \mathcal{E}_{tot} denotes the total energy density relative to the full lower band. In fact, the energy of the full lower band also depends on h_1 and h_2 . However, this dependence is weak, hence we neglected the contribution of the full lower band in our calculation of h_1^{opt} and h_2^{opt} .

Finally, we define the optimal energy density with kinetic energy measured relative to the band bottom as follows, $\mathcal{E}_{\text{tot}}^*(n_1) \equiv \mathcal{E}_{\text{tot}}(n_1, \Delta n - n_1, h_1^{\text{opt}}, h_2^{\text{opt}})$. The minimum of $\mathcal{E}_{\text{tot}}^*$ with respect to n_1 yields the filling of each of the components, n_1^{opt} and $n_2^{\text{opt}} = \Delta n - n_1^{\text{opt}}$ in the variational ground state of the system in the rotating frame. Substituting explicit expressions of the energy densities [Eqs. (S116) and (S117)] and optimal magnetizations (h_1^{opt} and h_2^{opt}) into Eq. (S118), we find $\mathcal{E}_{\text{tot}}^*(n_1) = \frac{\pi(\Delta n)^2}{m_*} \sqrt{\frac{U\Delta n}{\Delta_F}} \tilde{\mathcal{E}}_{\text{tot}}^*(n_1/\Delta n) + \Delta n \Delta_F/2$, where

$$\tilde{\mathcal{E}}_{\text{tot}}^*(\tilde{n}) = \tilde{n}^{5/2} + (1 - \tilde{n})^{5/2} + \tilde{u} \tilde{n}(1 - \tilde{n}), \quad (\text{S119})$$

and $\tilde{u} \equiv \frac{m_* U_{12}}{\pi} \sqrt{\frac{\Delta_F}{U \Delta n}}$.

Fig. S7b shows $\mathcal{E}_{\text{tot}}^*$ as a function of the normalized density $n_1/\Delta n$ for three values of \tilde{u} . For $\tilde{u} < 4 - \sqrt{2}$, the quasienergy has a global minimum at $n_1 = \Delta n/2$, corresponding to an equal share of particles between the two time-reversal components, see Fig. S7b. For $\tilde{u} > 4 - \sqrt{2}$, the quasienergy density has two global minima at $n_1 = 0$ and $n_1 = \Delta n$, corresponding to the situation where one of the components is undoped due to the strong inter-partner repulsion.

In conclusion, we showed that a model which includes the time reversal partner of the Hamiltonian discussed in the main text [see Eq. (1)], may still exhibit a symmetry breaking phase. Within our mean-field analysis

| | | | |
|----------|-------|-------------------------|----------------|
| A/E_g | 1/60 | V/E_g | $\sqrt{0.025}$ |
| B/E_g | 1/30 | $\delta E/E_g$ | 1/200 |
| A'/E_g | 1/240 | $v_\ell/(\Delta_F/k_R)$ | 1.6 |
| B'/E_g | 1/120 | | |

TABLE S1. Parameters used in the numerical simulations.

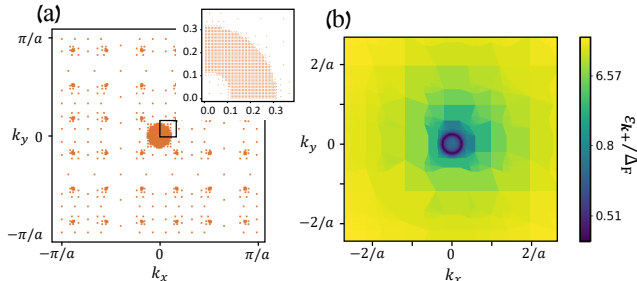


FIG. S8. (a). The nonuniform momentum grid which we used in the simulation. The highest density of momentum points resides around the resonance curve, $|\mathbf{k}| = k_R$. The total number of points is 8008. The inset shows a zoom in on the area with high density of points. (b). The energy of the upper band on the logarithmic scale computed on the nonuniform grid in panel a.

above, we found that when the repulsion between the time-reversal partners is not too strong, the symmetry breaking in both time-reversal partners minimizes the energy in the rotating frame. If the inter-partner repulsion is stronger than a critical value, only one of the partners becomes doped and develops a symmetry breaking term. Interestingly, within the mean-field approximation the energy is independent of the relative orientation of the magnetizations of the two time-reversal partners. To determine the optimal relative orientation, one needs to go beyond the mean-field theory we considered. We believe this is an interesting problem for future research. In addition, the analysis presented in this section is limited to $\kappa = 0$ case. It would be interesting to extend this analysis to finite effective temperature steady states.

V. DETAILS OF THE NUMERICAL SIMULATION

In this section we discuss the details of the numerical analysis. The parameters used in the simulation are summarized in Table S1. To see a pronounced suppression in U_c (see Fig. 2a) we worked at low densities of excitations, requiring a high-resolution grid of k -points. To reduce the amount of computational power, we created a nonuniform grid of momentum points with an enhanced density of points around the resonance ring, and total 8008 k -points. Fig. S8 demonstrates the grid that we used and the Floquet quasienergy levels of the upper Floquet band near the resonance ring. Each point in panel

(a) of this figure indicates a center of a grid cell, of area depending on the density of the grid in the vicinity of this cell. To ensure that the areas of all the cells amount to the total area of the Brillouin zone $[(2\pi/a)^2]$, we built the nonuniform grid as follows. First, we partitioned the Brillouin zone to $2^{10} \times 2^{10}$ cells. Then, we recursively combined clusters of $(2 \times 2)^n$ cells to form super cells, where the value of $n < 10$ controls the density of cells in the vicinity of the cluster. The area of such a cluster equals $(2\pi/(2^{10-n}a))^2$.

The k -grid is used to define the populations and the rates in the kinetic equation [Eq. (4) in the main text]. We calculated the rates $I_{\mathbf{k}\nu}^s$, $I_{\mathbf{k}\nu}^\ell$, appearing in this equation, using the Fermi's golden rule,

$$I_{\mathbf{k}\nu}^p = \sum_{\mathbf{k}'\nu'} (\dot{f}_{\mathbf{k}\nu})_{p,\mathbf{k}'\nu'}, \quad (\text{S120})$$

where $(\dot{f}_{\mathbf{k}\nu})_{p,\mathbf{k}'\nu'}$ is given by Eq. (S46). In a realistic realization of the driven system in a solid state setup, we expect the electron-phonon excitation rates to be suppressed by $(V/\Omega)^2$, as explained in Sec. III D 2. However, in our simulation, we took a large value of V/Ω (see Tab. S1) which facilitates large density of states near the Floquet gap. To capture the suppression of the electron-phonon excitations, we multiplied the squared matrix element $\mathcal{P}_s^{(l)}$ appearing in the definition of $(\dot{f}_{\mathbf{k}\nu})_{s,\mathbf{k}'\nu'}$ [see Eq. (S46)], by a factor v_V^{2l} , where $v_V = 10^{-2}$ represents realistic values of V/Ω .

To avoid using four-point terms for the electron-electron scattering collision integral in the numerical simulation of the kinetic equation [Eq. (S50)], we used an approximate expression for the collision integral of the form $I_{\mathbf{k}\nu}^{ee} = r_A U^2 I_{\mathbf{k}\nu}^\ell$. Such a collision integral mimics a source term due to Electron-electron interaction-activated excitation rate, described in Sec. III D 3. The parameter r_A sets the relative strength of this rate. Note that our numerical simulation, with the above simplification for the collision integral, does not take in account equilibration of the electron and hole distributions via electron-electron scattering. We argue in Sec. III H 2 that including this process will not qualitatively change the results of the numerical simulation.

In the first iteration of the algorithm we set the initial value of the magnetization field to have a form of the in-plane rotating field $\mathbf{h}^{(0)}(t) = h_1^{(0)}(\hat{x} - i\hat{y})e^{i\Omega t} + c.c.$, with $|h_1^{(0)}|/\Delta_F \sim 5 \times 10^{-7}$. We then solved the kinetic equation [given in Eq. (4) in the main text] in the steady-state ($\dot{f}_{\mathbf{k}\nu} = 0$), using the Newton-Raphson method and obtained the distribution $f_{\mathbf{k}\nu}$ after the first iteration. We used $f_{\mathbf{k}\nu}$ to calculate the magnetization vector $\mathbf{h}^{(1)}(t)$ for the next iteration of the algorithm, using Eq. (2) in the main text. As the momentum integral appearing in this equation is very sensitive to finite size effects, we evaluated the magnetization using an adaptive integration method. To this end, we used a fit of the steady-state distribution by two Fermi functions for the electron and hole excitations. Fig. S9 shows the comparison of the fits to

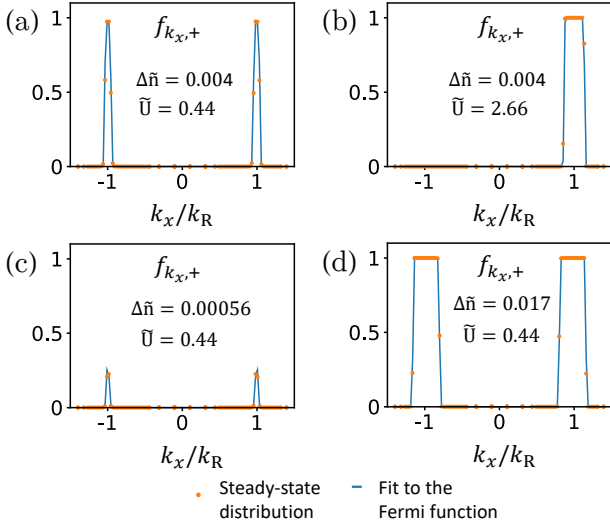


FIG. S9. Comparison between the steady state distribution of electrons in the upper Floquet band extracted from the numerical simulation, and the fit to the Fermi function, along the cut $k_y = 0$. The values of $\Delta\tilde{n}$ and \tilde{U} are indicated on the panels. (a,b). Steady-state distributions at the points indicated by the green and red squares in Fig. 2a in the main text. (c). Low-doping non-degenerate distribution of electrons in the “paramagnetic” phase, corresponding to the EFI regime. (d). Strongly doped “paramagnetic” phase, describing a degenerate Fermi distribution in the EFM regime.

the numerically obtained distributions at several points in the phase diagram in Fig. 2a in the main text. We then numerically integrate Eq. (2) over the fitting functions, to obtain the magnetization, $\mathbf{h}^{(1)}(t)$. Finally, we substituted $\mathbf{h}^{(1)}(t)$ in the mean-field Hamiltonian [Eq. (3)] and used it for the next iteration of the algorithm. The iteration loop terminates when the change in amplitude of the left-handed circular component of the magnetization reaches a threshold value. We verified that other components have also converged.

A. Relation between κ and system parameters

In the simulation we controlled the value of κ by the variation of the electron-photon coupling coefficient g_ℓ and measured κ from measurements of excitation densities [via Eq. (S36)]. The definition of κ , given in Eq. (S37), suggests that it is also sensitive to other parameters of the system controlling the heating and cooling rates. In particular, even though we fixed the value of g_ℓ throughout the phase diagram in Fig. 2a in the main text, the value of κ still may vary as a function of U and Δn . We chose the point $U = 0$, $\Delta n = 0$ in the phase diagram as a reference and denoted the value of κ at this point by κ_0 .

The value of κ is approximately equal to κ_0 throughout most of the phase diagram in Fig. 2a (for fixed g_ℓ). Yet,

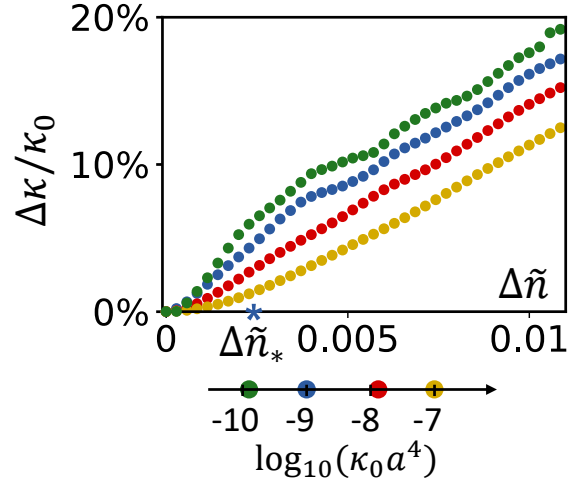


FIG. S10. The difference $\Delta\kappa = \kappa - \kappa_0$ as a function of the doping along the phase boundary line for four values of κ_0 indicated at the logarithmic scale. The optimal doping for $\kappa_0 a^4 \approx 10^{-9}$ is indicated by $\Delta\tilde{n}_*$.

it differs from κ_0 deep in the broken symmetry phase, as the single-particle Floquet band structure in this regime is significantly deformed. Furthermore, the value of κ slightly varies (at low doping) even in the symmetric phase, due to higher order doping-sensitive terms omitted from Eq. (S35). Likewise, we expect slight changes in κ relative to κ_0 at the phase boundary. As we show in Fig. S10, the relative change in κ at the phase boundary near the optimal doping (indicated by $\Delta\tilde{n}_*$ in the figure) is less than 5%. This finding justifies the assumptions made in our extended rate equation (outlined in Sec. III), where we treated κ as a doping-independent quantity.

B. Sensitivity of the self-consistent solution to the initial conditions

Here we examine the sensitivity of the self-consistent solution to the initial magnetization, $\mathbf{h}^{(0)}(t)$. All the results are obtained for $\Delta\tilde{n} = 0.004$ and $\tilde{U} = 2.66$, indicated by the red square in Fig. 2a in the main text.

First, we tested the response to different phase shifts of the initial magnetization, $\mathbf{h}^{(0)}(t) = h_1^{(0)} e^{i\varphi_0} (\hat{x} - i\hat{y}) e^{i\Omega t} + c.c.$. We swept φ_0 in the range $[-180^\circ, 0^\circ]$, and measured the in-plane component of the first harmonics of the self-consistent mean-field solution, $\mathbf{h}_1^{(xy)} = |h_x| e^{i\varphi_x} \hat{x} + |h_y| e^{i\varphi_y} \hat{y}$ [see definition of $\mathbf{h}_1^{(xy)}$ in the text following Eq. (8)]. Our simulation provides the complex-valued amplitudes of the components in the coordinate system spanned by \hat{x} and \hat{y} . We define a new coordinate system (spanned by \hat{x}' and \hat{y}') in which the \hat{x}' component

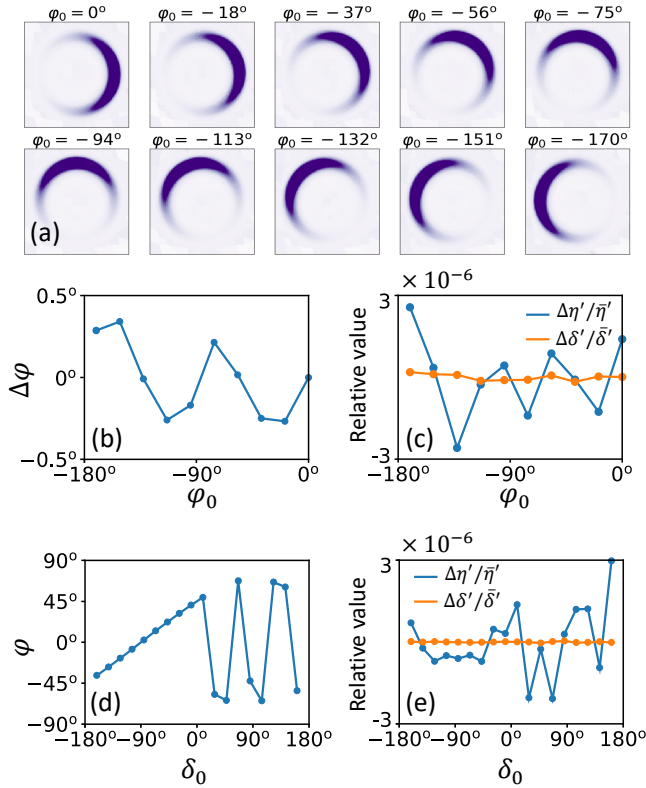


FIG. S11. Sensitivity of the self-consistent solution to initial conditions. All the results are obtained for $\Delta\tilde{n} = 0.004$ and $\tilde{U} = 2.68$, indicated by the red square in Fig.2a in the main text. (a). Steady-state distribution of the electrons in the upper Floquet band, f_{k+} , as a function of k_x and k_y , near the resonance ring for several values of the phase shift in the initial magnetization, φ_0 , see text. (b). The angle mismatch between φ_0 and the phase of the self-consistent field, φ , for the data shown in panel a. (c). Fluctuations of the relative polarization amplitudes and angles, $\Delta\eta' = \eta' - \bar{\eta}'$, $\Delta\delta' = \delta' - \bar{\delta}'$, where $\bar{\eta}' \approx 1.078$ and $\bar{\delta}' = -90^\circ$. (d). Phase shift of the self-consistent field φ , as a function of the relative initial polarization angle δ_0 . (e). Fluctuations of the relative polarization amplitudes and angles as a function of δ_0 .

is real. The angle between \hat{x} and \hat{x}' is given by

$$\tan(\varphi) = -\frac{|h_x| \sin(\varphi_x)}{|h_y| \sin(\varphi_y)}. \quad (\text{S121})$$

In the new coordinate system, the in-plane component of the magnetization reads

$$\mathbf{h}_1^{(xy)} = |h_{x'}| \hat{x}' + |h_{y'}| e^{i\delta'} \hat{y}'. \quad (\text{S122})$$

In a system described by a perfectly rotational symmetric interacting Hamiltonian, we expect $\varphi = \varphi_0$. In turn, we expect the \hat{x}' and \hat{y}' components to be same as the magnetization obtained in the case of $\varphi_0 = 0$, shown in Fig. 2b in the main text. Namely, the relative angle between \hat{x}' and \hat{y}' polarizations, δ' , is expected to be equal $\sim -90^\circ$. And the ratio of the amplitudes,

$$\eta' = h_{x'}/h_{y'} \quad (\text{S123})$$

is expected to be equal ~ 1.078 .

Fig. S11a demonstrates the steady-state distributions of the electrons as a function of the phase shift, φ_0 . Clearly, the angle along which the system breaks the symmetry in the rotating frame, φ , follows φ_0 . Fig. S11b shows the deviation between the two angles, $\Delta\varphi = \varphi - \varphi_0$ as a function of φ_0 . The deviation exhibits fluctuations around 0° within the range of $\pm 0.5^\circ$ presumably due to the lattice effects, spoiling the perfect rotational symmetry of the Hamiltonian. Fig. S11c shows the relative fluctuations of the angle δ' [see Eq. (S122)], and the ratio of the amplitudes, η' [Eq. (S123)] as a function of φ_0 . Both quantities are almost constant with relative fluctuations of the order of $\sim 10^{-6}$ around their averages over the data set, $\bar{\delta}' \approx -90^\circ$ and $\bar{\eta}' \approx 1.078$.

Next, we checked the stability of the self-consistent solution to different elliptical polarizations of the initial conditions. This time, we set the initial mean-field to $\mathbf{h}^{(0)}(t) = h_1^{(0)}(\hat{x} + e^{i\delta_0}\hat{y})e^{i\Omega t} + c.c.$, and swept δ_0 in the range $[-180^\circ, 180^\circ]$. For each value of δ_0 , we found the self-consistent mean-field solution and extracted the first harmonic of an in-plane component of the magnetization. The result rotated to the new coordinate system by φ [Eq. (S121)] is of the form given in Eq. (S122). Fig. S11e shows the fluctuations of δ' and η' [defined in Eq. (S123)], relative to the averages $\bar{\delta}' \approx -90^\circ$ and $\bar{\eta}' \approx 1.078$, as a function of δ_0 . It follows that the quantities δ' and η' are almost insensitive to δ_0 , with relative fluctuations of the order of $\sim 10^{-6}$. Fig. S11d shows the rotation angle, φ , as a function of δ_0 . When $\delta_0 < 0$, the phase shift of the self-consistent solution approximately equals the average between the phases of the initial x and y polarizations, $\varphi \approx (\delta_0 + 90^\circ)/2$. This relation breaks when $\delta_0 > 0$, i.e., when the polarization has a strong right-handed circular polarization component. Exactly at $\delta_0 = 180^\circ$, the self-consistent algorithm does not find a solution with a nonzero magnetization.

VI. ANALYSIS WHEN THE FLOQUET-AUGER RATE IS SIGNIFICANT

In this section we analyze the phase diagram when the excitation rate due to Floquet-Auger heating described in Sec. III D 3 is significant. The effect of Floquet-Auger processes is introduced in the model by an additional heating channel with a strength depending on U^2 (see Sec. V). In this case, κ reads

$$\kappa(\tilde{U}) = \kappa_{\text{ph}} + \chi_{\text{ee}}\tilde{U}^2, \quad (\text{S124})$$

where $\chi_{\text{ee}} = \kappa_{\text{ee}}/\tilde{U}^2$ and $\kappa_{\text{ee}} = \Gamma_{\text{ee}}/\Lambda_{\text{inter}}$ [cf. Eqs. (S62) and (S65)]. Note that $\tilde{U} = \mathcal{A}_{\text{R}}U/\delta E$ is the normalized interaction strength, such that χ_{ee} and κ_{ph} have the same dimensions. To see how the phase boundary is affected by the Floquet-Auger processes, recall that \tilde{U}_c , given by Eq. (10) in the main text, depends on κ through the dependence of the densities n_e and n_h on κ [see Eq. (S38)]

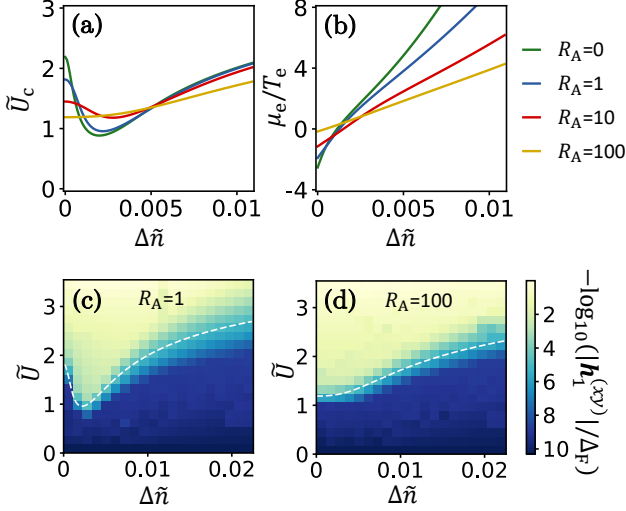


FIG. S12. Phase diagram as a function of the strength of the Auger processes, $R_A = \chi_{ee}/\kappa_{ph}$ for $\kappa_{ph} \approx 10^{-9}$ and $v_s = 0.0086\Delta_F/k_R$. (a). \tilde{U}_c obtained by solving Eq. (10) where n_e , n_h , μ_e/T_e , and μ_h/T_h were taken from the analytical rate equation approach [Eqs. (S38), (S100) and (S101)] and κ is given by Eq. (S124). We used the same parameters for ζ , \tilde{U}_{ex} , and \tilde{U}_{fb} as in Fig. 3 in the main text. (b). The ratio μ_e/T_e extracted from Eqs. (S100) and (S124), for the values of \tilde{U} obtained from the data in panel a. (c,d). Spontaneous magnetization strength, $|\mathbf{h}_1^{(xy)}|$ obtained from the self-consistent mean-field calculation, as a function of a normalized electron doping and normalized interaction strength, for two values of R_A . White dashed lines represent the analytical calculation, shown in panel a for the corresponding values of R_A .

and through the dependence of μ_e/T_e and μ_h/T_h on κ , cf. Eq. (S100). Therefore, Eq. (10) becomes a transcendental equation for \tilde{U}_c which can be solved numerically. The primary effect of a strong Floquet-Auger rate would be increasing the excitation density and heating the steady-state distribution.

We evaluate the relative effect of the Floquet-Auger heating by a dimensionless parameter $R_A = \chi_{ee}/\kappa_{ph}$. Figs. S12a and b show \tilde{U}_c and μ_e/T_e resulting from the numerical solution of the transcendental equation obtained from combining Eq. (10) in the main text with Eqs. (S38), (S100), (S101) and (S124). We plot the results for four values of R_A . The effect of increasing R_A is very similar to the effect of changing κ_0 in Fig. 3c and d in the main text, as both control the effective heating. Panels c and d in Fig. S12 show the results of the self-consistent mean-field calculation of the in-plane magnetization component, $\mathbf{h}_1^{(xy)}$, as a function of \tilde{U} and $\Delta\tilde{n}$ for $R_A = 1$ and $R_A = 100$. The parameter R_A is controlled in the simulation by tuning r_A (see Sec. V). White dashed lines represent the analytical solution to Eq. (10) similar to the corresponding line in the panel a.

-
- ¹ L. Lewin, *Polylogarithms and associated functions* (North-Holland, Amsterdam, 1981).
 - ² I. Esin, M. S. Rudner, and N. H. Lindner, (2019), [arXiv:1904.07856](#).
 - ³ N. W. Ashcroft and N. D. Mermin, *Solid state physics* (Brooks/Cole Cengage Learning, 2003).
 - ⁴ K. I. Seetharam, C.-E. Bardyn, N. H. Lindner, M. S. Rudner, and G. Refael, *Phys. Rev. X* **5**, 041050 (2015).
 - ⁵ M. S. Rudner and N. H. Lindner, (2020), [arXiv:2003.08252](#).
 - ⁶ K. I. Seetharam, C.-E. Bardyn, N. H. Lindner, M. S. Rudner, and G. Refael, *Phys. Rev. B* **99**, 014307 (2019).
 - ⁷ D. Wood, *The Computation of Polylogarithms*, Tech. Rep. (University of Kent, Computing Laboratory, 1992).
 - ⁸ E. Berg, M. S. Rudner, and S. A. Kivelson, *Phys. Rev. B* **85**, 035116 (2012).